

Linear Quantum Optics: Components and Applications

William R. Clements
Lady Margaret Hall, Oxford



Submitted for the degree of Doctor of Philosophy
Trinity term 2018

Supervised by
Prof. Ian A. Walmsley
Dr. W. Steven Kolthammer

Clarendon Laboratory
University of Oxford
United Kingdom

Linear Quantum Optics: Components and Applications

William R. Clements
Lady Margaret Hall, Oxford

Submitted for the degree of Doctor of Philosophy
Trinity Term 2018

Abstract

Quantum optics has successfully been used to test fundamental principles in quantum physics and to demonstrate the potential of quantum-enhanced technologies. Linear quantum optics, in which large quantum states of light are produced by optical interference of smaller quantum states, has proved to be particularly fruitful. Further progress will rely both on developing improved experimental tools to manipulate and measure quantum light, and on expanding and refining the range of applications of these technologies. This thesis presents our contributions towards both of these endeavours.

We first focus on some of the components necessary for linear quantum optics, starting with the requirement for reconfigurable interference between several optical modes. We propose a novel design for interferometers that satisfy this requirement, which is based on a new mathematical decomposition of unitary matrices used to describe optical interference. We show that our design is more efficient than previously known designs. We also experimentally demonstrate a modular approach to building these devices, which is based on the assembly of multiple UV-written integrated photonic chips. These chips are characterised, and three of them are assembled into a structure shown to enable a wide range of optical transformations. We then study methods of photon detection, showing how photon detectors can be calibrated and discussing the operation of superconducting photon number resolving transition edge sensors.

Next, we study two applications of linear optics. We examine the applicability of a proposal for simulating molecular spectroscopy using quantum optics in the presence of experimental imperfections. Our findings are illustrated with a proof of principle experiment in which we simulate part of the vibronic spectrum of the tropolone molecule. Finally, we study a class of optical devices, known as optical Ising machines, that has been shown to find solutions to difficult combinatorial problems. Describing the optical pulses in these devices in phase space as Gaussian quasi-probability distributions that evolve stochastically, we analyse the computational mechanism of these machines and show in theory that they can be simplified without affecting their performance.

Acknowledgments

Many people have helped and supported me during my DPhil, both in the lab and outside of it. First, I thank my supervisors, Ian and Steve, who took the risk of taking me on in the first place and the time to be my mentors. Ian, you've also done a fantastic job creating a group full of smart, helpful, and social physicists. I couldn't imagine a better working environment. Steve, you've taught me a lot about what it means to do science. I've always been impressed by your thoroughness and precision, and by trying to emulate you I think I've become a better scientist.

I am also grateful to the two post-docs I worked most closely with for all the time and effort they put into guiding me through my DPhil. Ben, working with someone as knowledgeable, patient and kind as you gave me the best possible introduction to both the Ultrafast group and the research field. Jelmer, you took your supervisory role above and beyond what had been required of you. You always supported me when I needed support, asked the difficult questions that had to be asked, and saw me through to the completion of my projects. I feel tremendously lucky to have known both of you and to have worked with you.

Numerous other members of the Ultrafast group and beyond have also had a huge impact on my work. Andreas, thanks for teaching me all about photon sources and for all the effort you put into making them work. Helen, Peter, Adrian, and Jan, our discussions have taught me a lot of what I know now about optics and quantum physics. David, Jake, and Roel, it's been a pleasure spending long hours with you setting up experiments or putting out fires (literally) in the lab. Paolo, James, and Thomas, thanks for letting me use all your amazing devices! There are too many Ultrafasters for me to list all of those who have contributed in many other ways; I am grateful to you all.

Thanks are also due to the people who made my life in Oxford be about more than just

my research. First, I feel lucky to have done my DPhil in a group in which the distinction between friend and colleague is as blurred as it is in Ultrafast. You're fantastic people to spend time with both in and outside of work. I'm going to miss our celebrations of successes, birthdays, Fridays, sunny days, or anything else really. My life has also been enriched by the companionship of my housemates and the friends I have met through college, societies, and elsewhere. Finally, I want to thank Sally. You more than anyone else made me enjoy my DPhil years as I did. You've encouraged me all along, and have made me feel at home in Oxford.

Lastly, I thank my family for the love and support you've given me during my student years. Celia, your dedication and drive in everything you do have been a huge inspiration for me. Nick and Annie, you gave me my passion for learning and have made me into who I am now.

Journal publications and conference presentations

Journal Publications

1. W. R. Clements, P. C. Humphreys, B. J. Metcalf, W. S. Kolthammer, and I. A. Walmsley, “**Optimal Design for Universal Multiport Interferometers**” *Optica*, **3**(12), 1460-1465 (2016).
2. W. R. Clements, J. J. Renema, Y. H. Wen, H. M. Chrzanowski, W. S. Kolthammer, and I. A. Walmsley, “**Gaussian Optical Ising Machines**” *Physical Review A* **96**(4), 043850 (2017).
3. W. R. Clements, J. J. Renema, A. Eckstein, A. A. Valido, A. Lita, T. Gerrits, S. W. Nam, W. S. Kolthammer, J. Huh, and I. A. Walmsley, “**Experimental Quantum Optical Approximation of Vibronic Spectroscopy**” *ArXiv* preprint arXiv:1710.08655 (2017).
4. P. L. Mennea, W. R. Clements, D. H. Smith, J. C. Gates, B. J. Metcalf, R. H. S. Banerman, R. Burgwal, J. J. Renema, W. S. Kolthammer, I. A. Walmsley., and P. G. R. Smith, “**Modular Linear Optical Circuits**” *Optica*, **5**(9), 1087-1090 (2018).
5. J. Sperling, W. R. Clements, A. Eckstein, M. Moore, J. J. Renema, W. S. Kolthammer, S. W. Nam, A. Lita, T. Gerrits, W. Vogel, G. S. Agarwal, and I. A. Walmsley, “**Detector-Independent Verification of Quantum Light**” *Physical Review Letters*, **118**(16), 163602 (2017).
6. R. Burgwal, W. R. Clements, D. H. Smith, J. C. Gates, W. S. Kolthammer, J. J. Renema, and I. A. Walmsley, “**Implementing random unitaries in an imperfect photonic network**” *Optics Express* **25**(23), 28236-28245 (2017).
7. J. Sperling, A. Eckstein, W. R. Clements, M. Moore, J. J. Renema, W. S. Kolthammer, S. W. Nam, A. Lita, T. Gerrits, I. A. Walmsley, G. S. Agarwal, and W. Vogel, “**Identification of nonclassical properties of light with multiplexing layouts**” *Physical Review A*, **96**(1), 013804 (2017).

8. J. J. Renema, A. Menssen, W. R. Clements, G. Triginer, W. S. Kolthammer, and I. A. Walmsley, “**Efficient Classical Algorithm for Boson Sampling with Partially Distinguishable Photons**” *Physical Review Letters*, **120**(22), 220502 (2018).
9. M. Stobińska, A. Buraczewski, M. Moore, W. R. Clements, J. J. Renema, S. W. Nam, T. Gerrits, A. Lita, W. S. Kolthammer, A. Eckstein, and I. A. Walmsley, “**Quantum interference enables constant-time quantum information processing**” *ArXiv* preprint arXiv:1807.03960 (2018).

Conference Presentations

1. W. R. Clements, B. J. Metcalf, P. C. Humphreys, W. S. Kolthammer, and I. A. Walmsley, “**Towards Practical Characterisation of Superconducting Single Photon Detectors**” *Quantum Technologies for Europe Summer School*, June 2015.
2. W. R. Clements, P. C. Humphreys, B. J. Metcalf, W. S. Kolthammer, and I. A. Walmsley, “**An Optimal Design for Universal Multiport Interferometers**” *Single Photons Single Spins Conference*, September 2016.
3. W. R. Clements, P. C. Humphreys, B. J. Metcalf, W. S. Kolthammer, and I. A. Walmsley, “**An Optimal Design for Universal Multiport Interferometers**” *Bristol Young Scientists Conference*, April 2016.
4. W. R. Clements, P. C. Humphreys, B. J. Metcalf, W. S. Kolthammer, and I. A. Walmsley, “**An Optimal Design for Universal Multiport Interferometers**” *Quantum Technology for the 21st Century*, May 2016.
5. W. R. Clements, P. C. Humphreys, B. J. Metcalf, W. S. Kolthammer, and I. A. Walmsley, “**An Optimal Design for Universal Multiport Interferometers**” *International Conference on Quantum Communication, Measurement and Computing*, July 2016.
6. W. R. Clements, “**Non-Universal Quantum Computing Using Linear Optics**” *4th NUDT-Oxford International Workshop on Quantum Information*, July 2017.

Contents

Acknowledgments	ii
Journal publications and conference presentations	iv
List of Figures	xi
List of Tables	xiii
1 Introduction	1
1.1 Thesis Outline	3
I Linear Optics	6
2 Quantum Physics of Light	7
2.1 Quantisation of the electromagnetic field	7
2.1.1 Quantum description of the state of an optical mode	9
2.2 Quantum states of light	10
2.2.1 Fock states	10
2.2.2 Quadrature states	11
2.2.3 Fock states in the quadrature basis	12
2.2.4 Coherent states	14
2.3 Modal transformations	16
2.3.1 Displacement	16
2.3.2 Phase shift	17
2.3.3 Squeezing	18
2.3.4 Rotation	20
2.3.5 General Bogoliubov transformation	22

2.3.6	Optical loss	23
2.4	Measurements	24
2.4.1	Photon number measurements	24
2.4.2	Homodyne measurements	25
2.5	Quasiprobability distributions and Gaussian states	26
2.5.1	Wigner function	26
2.5.2	P function	29
2.5.3	Gaussian states	30
2.5.4	Gaussian state formalism	31
2.6	Conclusion	32
3	Introduction to Linear Optics	33
3.1	Applications of linear optics	34
3.1.1	Fundamental studies in quantum physics	34
3.1.2	Metrology	34
3.1.3	Quantum information processing	35
3.1.4	Boson sampling	36
3.1.5	Linear quantum optical networks	38
3.2	Technology for linear optics	39
3.2.1	Quantum light sources	40
3.2.2	Integrated photonics	41
3.2.3	Photon detectors	48
3.3	Conclusion	53
II	Components for Linear Optics	54
4	Universal multiport interferometers	55
4.1	Optimal design for universal multiport interferometers	57
4.1.1	Background	58
4.1.2	Overview of the two designs	60
4.1.3	Decomposition method	61
4.1.4	Some possible implementations	67
4.1.5	Characterising a realistic universal multiport interferometer	70
4.2	Error tolerance of universal multiport interferometers	71
4.2.1	Loss tolerance	71
4.2.2	Beam splitter imperfections	74
4.3	Conclusion	81

5 Modular Linear Optical Circuits	82
5.1 Modular architecture	83
5.1.1 Why a modular design?	85
5.1.2 Motivation for the structure	86
5.1.3 Structure and fabrication	87
5.1.4 Electronics	88
5.2 Characterisation	90
5.2.1 Optical characterisation	90
5.2.2 Electrical characterisation	93
5.2.3 Experiment Planning	95
5.3 Characterising a three chip assembly	96
5.3.1 Switching between optical outputs	97
5.3.2 Implementing a tritter	98
5.3.3 Implementing a universal multiport interferometer	99
5.4 Conclusion	108
6 Photon Detectors	109
6.1 Measuring the efficiency of photon detectors	110
6.1.1 Overview of the scheme	111
6.1.2 Radiometer	112
6.1.3 Attenuation Stage	120
6.1.4 Photon Counting	122
6.2 Operation of transition edge sensors	125
6.2.1 Experimental apparatus	125
6.2.2 Dilution refrigerator	130
6.2.3 Method of operation	135
6.2.4 Experiments	138
6.3 Conclusion	138
III Applications of Linear Optics	140
7 Quantum Optical Simulation of Vibronic Spectroscopy	141
7.1 Background	142
7.1.1 Vibronic spectroscopy	142
7.1.2 Quantum optical simulation of vibronic spectroscopy	147
7.2 Dealing with imperfections	151
7.2.1 Designing an experiment	152
7.2.2 Bounding the error	154

7.2.3	Classicality criterion	156
7.3	Experiments	158
7.3.1	Application to tropolone	158
7.3.2	Experimental Setup	160
7.3.3	Characterising the experimental setup	162
7.3.4	Results for tropolone	167
7.3.5	Results for benzene	169
7.4	Discussion	171
7.4.1	Analysis of the simulation of tropolone	171
7.4.2	Sulfur dioxide	174
7.4.3	Nonclassicality Analysis	177
7.5	Conclusion	178
8	Gaussian Optical Ising Machines	179
8.1	Background	180
8.1.1	Optical Ising machines	181
8.1.2	State of the art	183
8.2	Gaussian optical Ising machines	183
8.2.1	Theoretical framework	184
8.2.2	Gaussian measurement-feedback Ising machines	186
8.2.3	Gaussian optical delay line Ising machines	190
8.2.4	Interpretation	191
8.3	Simplified Ising machines	192
8.3.1	Replacing squeezing with other gain mechanisms	192
8.3.2	Outlook	194
8.4	Conclusion	195
9	Conclusion	196
9.1	Summary	196
9.1.1	Components for linear optics	196
9.1.2	Applications of linear optics	198
9.2	Directions for future research	200
9.2.1	Building larger quantum states	200
9.2.2	Developing quantum applications	202
9.3	Outlook	203

A Gaussian state formalism formulae	204
A.1 Simulation of squeezing and loss	204
A.2 Simulation of homodyne measurements	205
A.3 Simulation of phase insensitive gain	206
B Success probabilities for simulated optical Ising machines	208
Bibliography	211

List of Figures

2.1 Examples of Wigner functions	27
3.1 A schematic of a typical linear optics experiment	33
3.2 Image of a superconducting nanowire single photon detector	51
3.3 Resistance vs. temperature for a transition edge sensor	52
4.1 Designs for universal multiport interferometers	60
4.2 Algorithm for programming a universal multiport interferometer	62
4.3 Order in which matrix elements are nulled	65
4.4 Mach-Zehnder interferometer	67
4.5 Time bin implementation of a universal multiport interferometer	69
4.6 Transformation fidelities with imperfections	73
4.7 Distribution of beam splitter reflectivities	75
4.8 Effect of unbalanced MZIs on the fidelity	78
4.9 Increasing the fidelity with numerical optimisation and redundancy	80
5.1 Modular photonic chips	84
5.2 Layer structure of the modular chips	88
5.3 Characterisation of the modular chips	91
5.4 Picture of 3 assembled modular chips	96
5.5 Three chip assembly as a switch	97
5.6 Three chip assembly used as a tritter	98
5.7 Three chip assembly used as a universal multiport interferometer	100
6.1 Scheme for measuring the efficiency of photon detectors	111
6.2 Overview of the radiometer set-up	116
6.3 Spectra measured for the radiometry process	118
6.4 Sketch of the attenuation setup	121

6.5	Diagrams of a TES	126
6.6	Low temperature amplification system.	129
6.7	Circulation of ^3He in a dilution refrigerator	131
6.8	Pictures of our dilution refrigeration system	132
6.9	Analysing TES traces	136
7.1	Simulating vibronic spectra with quantum optics	148
7.2	Experimental setup for estimating vibronic spectra	160
7.3	Characterisation data for the vibronic spectra experiment	165
7.4	Fidelity as a function of loss	172
7.5	Simulated spectrum of sulfur dioxide	176
8.1	Overview of two types of optical Ising machines	181
8.2	Simulation success probabilities	186
8.3	Evolution of pulses in a MIF Ising machine	187
8.4	Evolution of pulses in a saturated MIF Ising machine	188
8.5	Histogram of simulation success probabilities	189

List of Tables

6.1	WSi SNSPD detection efficiencies	124
6.2	InGaAs SPAD detection efficiencies	125
7.1	Parameters for an ideal simulation of tropolone	159
7.2	Table of Franck-Condon factors for tropolone	168
7.3	Parameters for an ideal simulation of benzene	170
7.4	Parameters for an imperfect simulation of benzene	170
7.5	Table of Franck-Condon factors for benzene	171
7.6	Table of Franck-Condon factors for tropolone	173
7.7	Parameters for an ideal simulation of sulfur dioxide	175
7.8	Parameters for an imperfect simulation of sulfur dioxide	175

Introduction

Quantum physics describes the behaviour of light and matter at very small scales. This behaviour is often counter-intuitive; quantum physics allows for phenomena such as superposition^[1], entanglement^[2], and Bell non-local correlations^[3]. These phenomena are not observed in classical physics, which governs our day to day lives. Despite its counter-intuitive nature, quantum physics is one of the most successful scientific theories in human history^[4]. It has allowed for a greater understanding of nature from single particles to supernovae. In addition, the development of quantum physics has led to a whole range of new technologies ranging from modern computers to MRI scanners.

Further research into quantum physics is expected to yield fundamental insight into natural phenomena. Many open questions remain within the field of quantum physics, dealing with issues such as the nature of the quantum to classical transition^[5] and the behaviour of large quantum systems^[6]. Furthermore, quantum effects can be used to build better measurement systems which will provide insight into other fields, such as in the study of gravitational waves^[7], gravimetry^[8], magnetometry^[9,10], and time keeping^[11].

Moreover, harnessing quantum phenomena such as superposition and entanglement will enable a whole new range of technologies. Whereas many of the advances underpinning modern technology have relied on our understanding of the quantum behaviour of individual particles, future quantum technologies will directly make use of quantum phenomena in many-body quantum systems^[4]. In particular, quantum systems are known to hold vastly superior computing power than classical computers for solving some computational problems. The enhanced computing power manifests itself in the exponential increase of computing power with system size, when benchmarked against a classical computer. The development of quantum computing, quantum simulation, and related technologies that demonstrate this “quantum advantage” will revolutionise many fields of research and technology^[12].

A key requirement for realising the potential of quantum science is therefore the ability to create, manipulate, and measure large quantum states. This is a challenging task. Extremely precise tools are necessary for controlling systems in which quantum effects are manifest, due to the typically small sizes and energy scales involved. In addition, since interactions with the environment tend to erase quantum phenomena such as superposition and entanglement, these systems must be very well isolated. Several platforms show promise for meeting these requirements. Many body quantum phenomena have thus been demonstrated using trapped ions^[13] and atoms^[14], superconducting circuits^[15], and semiconductor structures^[16] for example.

Quantum optics is also a promising platform for quantum science. Photons are less sensitive to decoherence than many other quantum systems. Furthermore, many tools developed by the photonics industry can readily be used in quantum optics. In addition, the quantum

properties of light have been extensively studied^[17]. Due to these advantages, new ideas and technologies in quantum physics have often first been demonstrated using quantum optics. Examples include foundational studies into the nature of quantum physics, such as research on violations of Bell’s inequalities^[18–20] and decoherence^[21]. Demonstrations of quantum metrology^[7,22], computation^[23] and cryptography^[24] have also been performed with quantum optics.

There is still much work to be done on improving quantum optics technology. At present, some technologies required for manipulating light at the quantum level are still in their infancy, such as high efficiency photon sources and low-loss optical switches. The experiments that have been demonstrated to date have thus generally involved small quantum systems of up to 10 photons^[25]. However, techniques for achieving quantum control over light have been continuously improving over the last few years, with for example the recent development of high efficiency superconducting photon detectors^[26]. This progress has gone hand in hand with theoretical efforts to develop new applications for quantum states consisting of larger numbers of photons.

1.1 Thesis Outline

This thesis investigates methods for building larger quantum states of light and studies some of their applications. We focus our discussion on linear quantum optical systems, consisting of interconnected quantum light sources, interferometers, and detectors.

This thesis is structured as follows. Part 1, “Linear Optics”, contains background for this thesis. Chapter 1, “Quantum Physics of Light”, provides a quantum description of light that will be used in the rest of the thesis. Chapter 2, “Introduction to Linear Optics”,

then describes linear quantum optics in more detail and highlights some applications in foundational studies in quantum physics, metrology, and quantum information processing. We also provide an overview of the state of the art in experimental work on building linear quantum optical systems, in which we discuss sources of quantum light, integrated photonics for interferometry, and photon detectors.

Part 2, “Components for Linear Optics”, investigates experimental tools for manipulating and measuring quantum states of light. The first two chapters deal with methods of building interferometers for linear quantum optics. In chapter 4, “Optimal Design for Universal Multiport Interferometers”, we discuss a method for designing reprogrammable devices that can implement any desired linear transformation between any number of optical modes. This method is based on a new mathematical decomposition of the unitary matrices describing optical interference. We also theoretically study how devices built following our method are tolerant to fabrication errors such as loss. In chapter 5, “Modular Linear Optical Circuits”, we experimentally demonstrate a modular approach to building these interferometers, which is based on the assembly of multiple UV-written integrated photonic chips. These chips are characterised, and three of them are assembled into a structure shown to enable a wide range of optical transformations.

Chapter 6, entitled “Photon Detectors”, presents experimental work on two aspects of photon detection. First, we demonstrate a method for measuring the efficiency of photon detectors that does not rely on an external calibrated reference, which we apply to two different types of detectors. We then describe the operation of transition edge sensors, which are a type of high efficiency photon-number resolving detector operating at cryogenic temperatures.

In Part 3, we study two applications of linear quantum optics. In chapter 7, “Quantum Optical Simulation of Vibronic Spectroscopy”, we investigate the applicability in the presence of experimental imperfections of a proposal for simulating molecular vibronic spectra using quantum optics. We show that the impact of these imperfections can be accounted for, and illustrate this result by performing a proof of principle experiment. In chapter 8, “Gaussian Optical Ising Machines”, we theoretically analyse the working mechanism of an optical computation device, consisting of many coupled pulses in a cavity, that has been shown to solve hard combinatorial problems. We provide a theoretical framework for studying these devices, which we show can replicate experimental results. We use our analysis to suggest routes for scaling these computational devices to larger sizes.

Taken together, the results presented in this thesis contribute to the development of linear quantum optics by expanding the range of experimental tools and examining some of its applications. In the conclusion, we discuss ways in which future research may benefit from the work presented here.

Part I

Linear Optics

Quantum Physics of Light

This chapter provides a quantum description of light that is used in the rest of this thesis.

We first introduce the quantisation of the electromagnetic field. We then describe some states of light and optical transformations that are of particular interest. Finally, we discuss quasi-probability distributions, as well as Gaussian states and Gaussian transformations.

2.1 Quantisation of the electromagnetic field

We start by introducing the concept of a quantised electromagnetic field. We consider the vector potential \mathbf{A} in vacuum. According to Maxwell's equations and in the Coulomb gauge $\nabla \cdot \mathbf{A} = 0$, the vector potential must satisfy^[27]:

$$\nabla^2 \mathbf{A}(r, t) = \frac{1}{c^2} \frac{\partial^2 \mathbf{A}(r, t)}{\partial t^2} \quad (2.1)$$

The boundary conditions of this problem determine a set of normal modes labelled k with frequency ω_k , such that the general solution of 2.1 can be written as:

$$\mathbf{A}(\mathbf{r}, t) = \sum_k \sqrt{\frac{\hbar}{2\omega_k \epsilon_0}} [a_k \mathbf{u}_k(\mathbf{r}) e^{-i\omega_k t} + a_k^* \mathbf{u}_k^*(\mathbf{r}) e^{i\omega_k t}] \quad (2.2)$$

This expression is entirely classical. Each normal mode is described by its spatial and temporal distribution $\mathbf{u}_k(r)e^{-i\omega_k t}$, with $\mathbf{u}_k(r)$ satisfying the Helmholtz equation^[17], and by its amplitude a_k .

We quantise the electromagnetic field by replacing the classical amplitude a_k by an operator \hat{a}_k which satisfies the bosonic commutation relations $[\hat{a}_i, \hat{a}_j] = 0$ and $[\hat{a}_i, \hat{a}_j^\dagger] = \delta_{ij}$. An in-depth justification for this quantisation procedure can be found in the textbook by Grynberg *et al*^[27]. The operator $\hat{\mathbf{A}}$ corresponding to the vector potential \mathbf{A} can now be written as follows:

$$\hat{\mathbf{A}}(\mathbf{r}, t) = \sum_k \sqrt{\frac{\hbar}{2\omega_k \epsilon_0}} [\hat{a}_k \mathbf{u}_k(\mathbf{r}) e^{-i\omega_k t} + \hat{a}_k^* \mathbf{u}_k^*(\mathbf{r}) e^{i\omega_k t}] \quad (2.3)$$

Equation 2.3 conveniently separates the classical aspect of light as described by the spatial distributions $\mathbf{u}_k(\mathbf{r})$, and the quantum aspect described by operators \hat{a}_k . Intuitively, it can be said that each mode of light defined by $\mathbf{u}_k(r)$ is populated by a quantised field described by \hat{a}_k ^[17].

2.1.1 Quantum description of the state of an optical mode

A description of the possible quantum states of light of an optical mode can be derived from the Hamiltonian of the electromagnetic field, which can be written as follows:

$$\hat{H} = \frac{1}{2} \int (\epsilon_0 |\hat{\mathbf{E}}|^2 + \mu_0 |\hat{\mathbf{H}}|^2) d\mathbf{r}^3 \quad (2.4)$$

where $\hat{\mathbf{E}}$ and $\hat{\mathbf{H}}$ respectively correspond to the electric field and the magnetic field. Using expression 2.3 and Maxwell's equations, the Hamiltonian can be rewritten as^[27]:

$$\hat{H} = \sum_k \hbar \omega_k (\hat{a} \hat{a}^\dagger + \frac{1}{2}) \quad (2.5)$$

This is the Hamiltonian of an ensemble of quantum harmonic oscillators with frequencies ω_k . The existing theory for quantum harmonic oscillators can therefore be applied to light. The conjugate quadrature operators \hat{q}_k and \hat{p}_k associated with these quantum harmonic oscillators are defined as follows:

$$\hat{q}_k = \frac{1}{\sqrt{2}} (\hat{a}_k^\dagger + \hat{a}_k), \quad \hat{p}_k = \frac{i}{\sqrt{2}} (\hat{a}_k^\dagger - \hat{a}_k) \quad (2.6)$$

These quadrature operators are Hermitian and satisfy the canonical commutation relations $[q_i, p_j] = i\delta_{ij}$ and $[q_i, q_j] = 0$. The Hamiltonian can be expressed in terms of the quadrature operators as:

$$\hat{H} = \sum_k \hbar \omega_k \left(\frac{\hat{q}_k^2}{2} + \frac{\hat{p}_k^2}{2} \right) \quad (2.7)$$

Moreover, these quadrature operators are the observables for the quadratures of the electromagnetic field, since the electric field associated with the vector potential in equation 2.3 can be written as:

$$\hat{\mathbf{E}}(\mathbf{r}, t) = \frac{i}{\sqrt{2}} \sum_k \sqrt{\frac{\hbar\omega_k}{\epsilon_0}} \mathbf{u}_k(\mathbf{r}) [\hat{a}_k e^{-i\omega_k t} - \hat{a}_k^\dagger e^{i\omega_k t}] \quad (2.8)$$

$$= \sum_k \sqrt{\frac{\hbar\omega_k}{\epsilon_0}} \mathbf{u}_k(\mathbf{r}) [\hat{q}_k \sin(\omega_k t) - \hat{p} \cos(\omega_k t)] \quad (2.9)$$

where we have assumed for simplicity that the $\mathbf{u}_k(\mathbf{r})$ are real. Complex $\mathbf{u}_k(\mathbf{r})$ would lead to an additional phase term in this expression.

2.2 Quantum states of light

This section focuses on three states of light that are particularly relevant to this thesis: Fock states, quadrature states, and coherent states.

2.2.1 Fock states

We focus on a single mode of the electromagnetic field and study the eigenstates of the Hamiltonian in equation 2.5. Since this Hamiltonian describes a quantum harmonic oscillator, its eigenstates are discrete and can be numbered as $|0\rangle, |1\rangle, \dots$, etc. These states are known as Fock states and are eigenstates of the number operator $\hat{n} = \hat{a}^\dagger \hat{a}$:

$$\hat{n} |n\rangle = n |n\rangle \quad (2.10)$$

A Fock state $|n\rangle$ contains n excitations of the mode under consideration. These excitations are also known as photons, such that state $|n\rangle$ is an n -photon state. Vacuum is Fock state $|0\rangle$. An n -photon state has an energy $\hbar\omega(n + \frac{1}{2})$ according to equation 2.5. These Fock states are transformed by operators \hat{a} and \hat{a}^\dagger as follows:

$$\hat{a}|n\rangle = \sqrt{n}|n-1\rangle, \quad \hat{a}^\dagger|n\rangle = \sqrt{n+1}|n+1\rangle, \quad \hat{a}|0\rangle = 0 \quad (2.11)$$

Since \hat{a} and \hat{a}^\dagger respectively remove and add photons from a state, these operators are respectively known as the annihilation and creation operators.

Due to the linearity of quantum mechanics, any normalised superposition of these Fock states is an allowable quantum state. Furthermore, since Fock states are the eigenstates of the Hamiltonian, they constitute a complete basis for the space of allowable quantum states. Any photonic quantum state can thus be described as a superposition of Fock states.

2.2.2 Quadrature states

In addition to Fock states, a useful basis in which to represent quantum states is that of the eigenstates of the quadrature operators. These quadrature operators are analogous to the position and momentum quadratures of a quantum harmonic oscillator. Formally, the eigenstates of $|q\rangle$ and $|p\rangle$ of operators \hat{q} and \hat{p} satisfy:

$$\hat{q}|q\rangle = q|q\rangle, \quad \hat{p}|p\rangle = p|p\rangle \quad (2.12)$$

Since the quadratures are conjugate canonical variables, their spectrum is unbounded and continuous^[17]. Furthermore, these eigenstates are related to each other by Fourier trans-

formation:

$$|q\rangle = \frac{1}{\sqrt{2\pi}} \int_{-\infty}^{\infty} e^{-iqp} |p\rangle dp \quad (2.13)$$

$$|p\rangle = \frac{1}{\sqrt{2\pi}} \int_{-\infty}^{\infty} e^{iqp} |q\rangle dq \quad (2.14)$$

These quadrature states allow us to introduce the quadrature wave functions:

$$\psi(q) = \langle q|\psi\rangle, \quad \tilde{\psi}(p) = \langle p|\psi\rangle \quad (2.15)$$

The quadrature wave functions have a physical interpretation. Their moduli squared correspond to the probability of measuring state $|q\rangle$ or $|p\rangle$ using a measurement that projects onto the set of quadrature operators. We note that these observables are constrained by the canonical uncertainty relation:

$$\langle \delta\hat{q}^2 \rangle \langle \delta\hat{p}^2 \rangle \geq \frac{1}{4} |[\hat{q}, \hat{p}]|^2 = \frac{1}{4} \quad (2.16)$$

This uncertainty relation indicates that the two quadratures of a state do not simultaneously have well defined values. Consequently, they cannot simultaneously be measured to arbitrary accuracy.

2.2.3 Fock states in the quadrature basis

Fock states can be expressed using quadrature wave functions and vice versa. For example, consider the vacuum state. For the quadrature wave function of vacuum $\psi_0(q)$, using equa-

tion 2.11 we have:

$$\hat{a}\psi_0(q) = \frac{1}{\sqrt{2}}(q + \frac{\partial}{\partial q})\psi_0(q) = 0 \quad (2.17)$$

where we have decomposed \hat{a} into the quadrature basis and used the formula $\hat{p} = -i\partial/\partial q$ ^[17].

This equation is solved for:

$$\psi_0(q) = \pi^{-1/4}e^{-q^2/2} \quad (2.18)$$

We note that, according to this expression and the relation between the quadratures and the electric field in 2.9, the vacuum state of the electromagnetic field has zero mean but non-zero variance. Specifically, the variance of its quadratures is $1/2$. This non-zero variance can be understood as stemming from the uncertainty relations in equation 2.16.

Having determined the wave function for the vacuum, the other Fock states can be expressed as quadrature wave functions using equation 2.11 with the following recursion relation:

$$\hat{a}^\dagger\psi_{n-1}(q) = \frac{1}{\sqrt{2}}(q + \frac{\partial}{\partial q})\psi_{n-1}(q) = \sqrt{n}\psi_n(q) \quad (2.19)$$

Which is satisfied by the following expression for $\psi_n(q)$:

$$\psi_n(q) = \frac{H_n(q)}{\sqrt{2^n n! \sqrt{\pi}}} e^{-q^2/2} \quad (2.20)$$

where H_n is the n -th Hermite polynomial.

2.2.4 Coherent states

Another important quantum state of light is the coherent state. The coherent state $|\alpha\rangle$ is defined as the eigenstate of the annihilation operator:

$$\hat{a} |\alpha\rangle = \alpha |\alpha\rangle \quad (2.21)$$

These states are as close as we can get to the classical picture of light as a wave, which would be fully described by an amplitude and a phase^[17]. Following equation 2.9, the expectation value for a given mode of the electromagnetic field populated with a coherent state $|\alpha\rangle$ is:

$$\langle \hat{\mathbf{E}}(\mathbf{r}, t) \rangle = \sqrt{\frac{2\hbar\omega}{\epsilon_0}} \mathbf{u}(\mathbf{r}) |\alpha| \sin(-i\omega t + \arg(\alpha)) \quad (2.22)$$

which indeed corresponds to a field with amplitude $\sqrt{\frac{2\hbar\omega}{\epsilon_0}} |\alpha|$ and phase $\arg(\alpha)$.

Coherent states can be described in the Fock basis as follows:

$$|\alpha\rangle = e^{\frac{|\alpha|^2}{2}} \sum_{n=0}^{\infty} \frac{\alpha^n}{\sqrt{n!}} |n\rangle \quad (2.23)$$

We note that this expression corresponds to a Poisson distribution of photon numbers. In the photon number picture, a coherent state can therefore be thought of as a statistical ensemble of several randomly generated and uncorrelated photons.

In the quadrature picture, if we decompose α into its real and imaginary parts as $\alpha = 1/\sqrt{2}(q_0 + ip_0)$, the quadrature wave functions of a coherent state can be written

as follows^[17]:

$$\psi_\alpha(q) = \pi^{-\frac{1}{4}} \exp\left(-\frac{(q - q_0)^2}{2} + ip_0q - \frac{ip_0q_0}{2}\right) \quad (2.24)$$

$$\tilde{\psi}_\alpha(p) = \pi^{-\frac{1}{4}} \exp\left(-\frac{(p - p_0)^2}{2} - iq_0p + \frac{ip_0q_0}{2}\right) \quad (2.25)$$

We note that this expression is the same as for vacuum, to within a displacement of q_0 and with an additional phase factor. This fact will be used later when we discuss displacement operations and Gaussian states. Furthermore, it can be seen from this expression that coherent states are minimal uncertainty states in that they saturate inequality 2.16, and the uncertainty is equally divided between the two quadratures.

Coherent states are particularly important in quantum optics because light emitted from a laser above threshold is well approximated as a coherent state. Large coherent states are therefore relatively simple to experimentally generate and manipulate. However, quantum phenomena such as superposition and entanglement are difficult to observe in these states since in the quadrature picture they behave as classical waves, and in the photon number picture they behave as a statistical ensemble of uncorrelated photons.

In the same way that the Fock basis and the quadrature basis can be used to describe quantum states of light, a coherent state basis can also be used. Indeed, any quantum optical state described by density operator ρ can be written as^[17]:

$$\rho = \int P(q_0, p_0) |\alpha\rangle \langle \alpha| dq_0 dp_0 \quad (2.26)$$

where P is known as the P-function for this state. The P-function of a coherent state defined by $\alpha = 1/\sqrt{2}(q_0 + ip_0)$ is $\delta(q_0, p_0)$. We note that the coherent state basis is not an orthogonal

basis, as there is finite overlap between any two coherent states. Furthermore, even though this expression describes ρ as a mixture of coherent states, the P function is not necessarily a well-behaved function. If the P-function is regular (i.e. analytic and single-valued) or not more singular than a delta function then the state can be described as a statistical mixture of coherent states, in which case the state is called “classical”. Otherwise, the state is called “nonclassical”.

2.3 Modal transformations

Until now, we have considered optical modes that evolve under the action of the Hamiltonian in equation 2.5. This equation does not consider modal transformations, which can be effected in several different ways. In the following, we consider some of the more common mode transformations: displacements, phase shifts, squeezing, and rotation. We will show that these transformations are sufficient to implement any unitary optical transformation described by a Hamiltonian that is at most quadratic in the annihilation and creation operators.

2.3.1 Displacement

We first consider the “displacement” operator:

$$\hat{D}(\alpha) = \exp(\alpha \hat{a}^\dagger - \alpha^* \hat{a}) \quad (2.27)$$

where α is a complex number. The annihilation operators are transformed under the action of this operator as follows:

$$\hat{D}^\dagger(\alpha)\hat{a}\hat{D}(\alpha) = \hat{a} + \alpha \quad (2.28)$$

There is an important relation between the displacement operator and coherent states:

$$\hat{D}(\alpha)|0\rangle = |\alpha\rangle \quad (2.29)$$

We had noticed earlier that the quadrature wave function for coherent states is the same as for vacuum to within a displacement in phase space. The displacement operator is the operator that causes this displacement. In general, the displacement operator displaces any optical state it is applied to in phase space by an amount determined by α .

Physically, an optical state can be displaced by α by interfering it with an ancilla mode containing a large coherent state $|\alpha/t\rangle$ on a beam splitter with reflectivity t^2 , in the limit of small t , and then tracing over the ancilla mode. Beam splitters are discussed in more detail in the following.

2.3.2 Phase shift

We consider the “phase shift” operator:

$$\hat{U}(\phi) = \exp(i\phi\hat{n}) \quad (2.30)$$

As its name implies, this operator introduces a phase shift ϕ to the annihilation operator \hat{a} :

$$\hat{U}^\dagger(\phi)\hat{a}\hat{U}(\phi) = e^{i\phi}\hat{a} \quad (2.31)$$

The phase shift operator can be used to change the phase of the electric field, as per equation 2.9. It can also be used to define new quadrature operators \hat{q}_ϕ and \hat{p}_ϕ that correspond to a rotation of the previous quadratures:

$$\begin{pmatrix} \hat{q}_\phi \\ \hat{p}_\phi \end{pmatrix} = \begin{pmatrix} \cos(\phi) & \sin(\phi) \\ -\sin(\phi) & \cos(\phi) \end{pmatrix} \begin{pmatrix} \hat{q} \\ \hat{p} \end{pmatrix} \quad (2.32)$$

2.3.3 Squeezing

We consider the “squeezing” operator:

$$\hat{S}(r) = \exp \left[\frac{1}{2}(r\hat{a}^{\dagger 2} - r\hat{a}^2) \right] \quad (2.33)$$

where r is a real number and is known as the squeezing parameter. This operator has the following effect on the annihilation operator:

$$\hat{S}^\dagger(r)\hat{a}\hat{S}(r) = \hat{a} \cosh(r) - \hat{a}^\dagger \sinh(r) \quad (2.34)$$

It is particularly informative to see how the squeezing operator transforms the quadrature operators:

$$\hat{q}' = \hat{S}^\dagger(r)\hat{q}\hat{S}(r) = \hat{q}e^{-r}, \quad \hat{p}' = \hat{S}^\dagger(r)\hat{p}\hat{S}(r) = \hat{p}e^r \quad (2.35)$$

The transformed quadrature operators thus have the following variances:

$$\langle \hat{q}'^2 \rangle = \langle \hat{q}^2 \rangle e^{-2r}, \quad \langle \hat{p}'^2 \rangle = \langle \hat{p}^2 \rangle e^{2r} \quad (2.36)$$

The squeezing operator has the effect of rescaling the quadratures by squeezing one quadrature and stretching the other, in such a way that the product of the variances is not affected and still respects the uncertainty relation in equation 2.16.

One state of particular interest that is created by the squeezing operator is the single mode squeezed vacuum $\hat{S}(r) |0\rangle$. This state still saturates the uncertainty relation in 2.16, but now one quadrature is squeezed and the other is stretched. Whereas the vacuum state is classical as it has a regular P function, squeezed vacuum is non-classical. In the photon number basis, single mode squeezed vacuum (SMSV) is written as:

$$\hat{S}(r) |0\rangle = \frac{1}{\sqrt{\cosh r}} \sum_{n=0}^{\infty} (-\tanh r)^n \frac{\sqrt{(2n)!}}{2^n n!} |2n\rangle \quad (2.37)$$

This state is a coherent superposition of photon pairs.

Physically, squeezing is generated by a non-linear process described by the Hamiltonian:

$$\hat{H} \propto r(\hat{a}^{\dagger 2} - \hat{a}^2) \quad (2.38)$$

This Hamiltonian can be implemented in a non-linear material such as potassium titanyl phosphate (KTiOPO₄ or KTP) traversed by a strong pump field. The non-linearity of the material causes the light from the pump field to interact with an optical “signal” mode with half the energy. This signal mode is amplified parametrically by the pump beam, and some

energy of the pump beam is converted into the additional fluctuations of one quadrature of the signal mode. In the photon number picture, photons from the pump beam are probabilistically converted into pairs of photons in the signal beam, which explains the absence of odd photon numbers in equation 2.37 where the initial state of the signal mode is vacuum.

2.3.4 Rotation

One last example of a modal transformation is the multimode rotation, which is a generalisation of the phase shift to several modes. We consider an ensemble of optical modes described by their annihilation operators \hat{a}_k . These modes can be made to interact with each other using the rotation operator \hat{R} :

$$\hat{R} = \exp(i\mathbf{J}_{kl}\hat{a}_k^\dagger \hat{a}_l) \quad (2.39)$$

where summation over k and l in the parenthesis is implied. \mathbf{J} is a Hermitian matrix describing the mode couplings. It can be seen that this operator transforms the annihilation operators as follows:

$$\hat{\mathbf{a}}' = \hat{R}^\dagger \hat{\mathbf{a}} \hat{R} = U \hat{\mathbf{a}} \quad (2.40)$$

where $U = \exp(i\mathbf{J})$ is a unitary matrix.

Physically, this rotation can be interpreted as optical interference between the modes. For example, a balanced beam splitter can be described by the following 2×2 modal

transformation between modes labelled 1 and 2:

$$\begin{pmatrix} \hat{a}_1' \\ \hat{a}_2' \end{pmatrix} = \frac{1}{\sqrt{2}} \begin{pmatrix} 1 & 1 \\ -1 & 1 \end{pmatrix} \begin{pmatrix} \hat{a}_1 \\ \hat{a}_2 \end{pmatrix} \quad (2.41)$$

These rotations can be used to create correlations between modes. For example, it can be shown that interfering two modes populated with identical squeezed vacua on a balanced beam splitter creates the following state in the photon number picture, which is known as a two mode squeezed vacuum (TMSV):

$$|0\rangle_{\text{TMSV}} = \frac{1}{\cosh r} \sum_{n=0}^{\infty} (\tanh r)^n |n\rangle |n\rangle \quad (2.42)$$

This state has perfectly correlated photon numbers in the two modes, such that a measurement of N photons in mode 1 projects mode 2 onto an N -photon Fock state. Furthermore, it can be shown that in such a state there also are quadrature correlations. The difference of the q quadratures $\hat{q}_1 - \hat{q}_2$ is squeezed whereas the sum of the p quadratures $\hat{p}_1 + \hat{p}_2$ is stretched.

Whereas rotations often create correlations between modes, coherent states have the particular property that they remain uncorrelated after a rotation. Indeed, a multimode state which is a separable product of coherent states remains a separable product of coherent states after a rotation. If the state before the rotation is $|\alpha\rangle = |\alpha_1, \alpha_2, \dots\rangle$ and the rotation is described by unitary matrix \mathbf{U} , then the output state is $|\mathbf{U}\alpha\rangle$.

2.3.5 General Bogoliubov transformation

We show here that the above transformations are sufficient to describe any unitary transformation generated by Hamiltonians that are at most quadratic in the creation and annihilation operators. As illustrated in our examples above, quadratic Hamiltonians acting on an ensemble of modes generate the following Bogoliubov transformations of the annihilation operators^[28]:

$$\hat{a}'_j = \sum_k (A_{jk} \hat{a}_k + B_{jk} \hat{a}_k^\dagger) + \beta_j \quad (2.43)$$

We now decompose matrices \mathbf{A} and \mathbf{B} into a convenient form. It can be shown as a consequence of the fact that the commutation relation between the \hat{a}'_j must be preserved that A and B can be written as:

$$A = U A_D V^\dagger, \quad B = U B_D V^T \quad (2.44)$$

where U and V are unitary matrices and A_D and B_D are diagonal real and positive matrices satisfying:

$$A_D^2 = B_D^2 + 1 \quad (2.45)$$

Based on this expansion, it can be seen that any Bogoliubov transformation of an ensemble of optical modes can be described first as a rotation described by matrix V , then a set of single mode squeezing operations with squeezing parameters $\text{acosh}(A_D)$, an additional rotation described by matrix U , and a displacement described by β .

2.3.6 Optical loss

An optical transformation that is particularly frustrating for experimentalists is optical loss. Optical loss can be described using the transformations that we have just introduced. Consider an optical mode in which each photon has a probability η of being removed from the mode of interest. The loss process is modelled as a rotation between the lossy mode and an ancillary vacuum mode at a beam splitter with reflectivity η . After this rotation, a new description of the optical state in the mode of interest is obtained by tracing over this vacuum mode. This trace operation reflects the loss of all information concerning the state of light in that mode.

Loss affects quantum states in the following ways. Fock state $|n\rangle\langle n|$ is transformed into an incoherent mixture of Fock states ρ by the following Bernoulli transformation:

$$\rho = \sum_{k=0}^n \binom{n}{k} \eta^{n-k} (1-\eta)^k |k\rangle\langle k| \quad (2.46)$$

Loss also causes squeezed states to become less squeezed and also introduces some degree of mixedness into the state. Specifically, the variance of a quadrature operator \hat{q} of a squeezed vacuum with a squeezing parameter $r \geq 0$ and undergoing loss η is:

$$\langle \hat{q}^2 \rangle = (1-\eta) \frac{e^{-2r}}{2} + \frac{\eta}{2} \quad (2.47)$$

The decrease in the squeezing comes from the additional noise introduced into the squeezed mode from the vacuum fluctuations of the ancilla mode.

Coherent states remain pure coherent states after loss. A coherent state $|\alpha\rangle$ becomes $|\sqrt{\eta}\alpha\rangle$ after experiencing loss. We note that a consequence of this property of coherent

states is that a displacement operation $\hat{D}(\alpha - \sqrt{\eta}\alpha)$ can be used to recover the original coherent state after experiencing loss.

2.4 Measurements

We proceed to describe some aspects of measurements in quantum optics. First, we recall that a measurement in quantum physics is described by a positive-operator valued measure (POVM) which consists of a set of Hermitian positive semidefinite operators F_i that sum to identity:

$$\sum_i F_i = 1 \quad (2.48)$$

The probability of a measurement of a state ρ resulting in the outcome described by F_i is then:

$$P(i|\rho) = \text{tr}(\rho F_i) \quad (2.49)$$

Two important measurements in quantum optics are photon number measurements and homodyne measurements.

2.4.1 Photon number measurements

The POVM for an ideal photon number measurement consists of the set of projectors onto Fock states $F_n = |n\rangle\langle n|$. Unfortunately, no such ideal detector exists. A common imperfection includes limited photon detection efficiency, which is modelled as loss so that the actual POVMs also contain higher photon components. Furthermore, dark counts can also

lead to POVM elements containing lower photon numbers.

A common type of photon detector is the “click” detector which only has two POVM elements F_1 and F_2 such that:

$$F_1 = |0\rangle\langle 0|, \quad F_2 = 1 - |0\rangle\langle 0| \quad (2.50)$$

This type of measurement can only distinguish between vacuum and the presence of at least one photon. Once again, losses and dark counts change the nature of these POVMs. We note that measurements in the photon number basis are not phase sensitive, as opposed to homodyne measurements.

2.4.2 Homodyne measurements

For a given quadrature, the POVMs for an ideal homodyne measurement of that quadrature are the set of quadrature eigenstates. For example, a homodyne measurement that measures \hat{q} projects onto the $|q\rangle$ eigenstates. Homodyne measurements can be performed along any quadrature, but due to the uncertainty relation 2.16 two different quadratures cannot be measured simultaneously to arbitrary accuracy.

In practice, a homodyne measurement can be performed by using a balanced beam splitter to mix the mode to be measured, defined by annihilation operator \hat{a}_1 , with another mode defined by \hat{a}_2 containing a strong coherent state $|\alpha\rangle$. We will assume for now that α is real. The annihilation operators \hat{a}'_1 and \hat{a}'_2 for the two outputs modes are then:

$$\hat{a}'_1 = \frac{1}{\sqrt{2}}(\hat{a}_1 + \hat{a}_2), \quad \hat{a}'_2 = \frac{1}{\sqrt{2}}(\hat{a}_2 - \hat{a}_1) \quad (2.51)$$

The number operators \hat{n}'_1 and \hat{n}'_2 for modes 1 and 2 are therefore:

$$\hat{n}'_1 = \frac{1}{2}(\hat{a}_1^\dagger \hat{a}_1 + \hat{a}_1^\dagger \hat{a}_2 + \hat{a}_2^\dagger \hat{a}_1 + \hat{a}_2^\dagger \hat{a}_2) \quad (2.52)$$

$$\hat{n}'_2 = \frac{1}{2}(\hat{a}_1^\dagger \hat{a}_1 - \hat{a}_1^\dagger \hat{a}_2 - \hat{a}_2^\dagger \hat{a}_1 + \hat{a}_2^\dagger \hat{a}_2) \quad (2.53)$$

So that their difference is:

$$\hat{n}'_1 - \hat{n}'_2 = \hat{a}_1^\dagger \hat{a}_2 + \hat{a}_2^\dagger \hat{a}_1 \quad (2.54)$$

Since mode 2 is a large coherent state with amplitude α , we can replace \hat{a}_2 with its expectation value $\alpha^{[29]}$ so that this expression becomes:

$$\hat{n}'_1 - \hat{n}'_2 = \sqrt{2}\alpha\hat{q} \quad (2.55)$$

Measuring the difference between the two intensities therefore yields a measurement of \hat{q} .

We note that a different quadrature can be selected by changing the phase of α .

2.5 Quasiprobability distributions and Gaussian states

2.5.1 Wigner function

In classical optics, a plane wave at a given frequency can be described using its amplitude and phase. We can therefore consider a two-dimensional phase space in which every point corresponds to a given plane wave. This two dimensional space is spanned by the two quadratures q and p . A probabilistic mixture of plane waves can be described using a probability distribution $W(q, p)$ over this space.

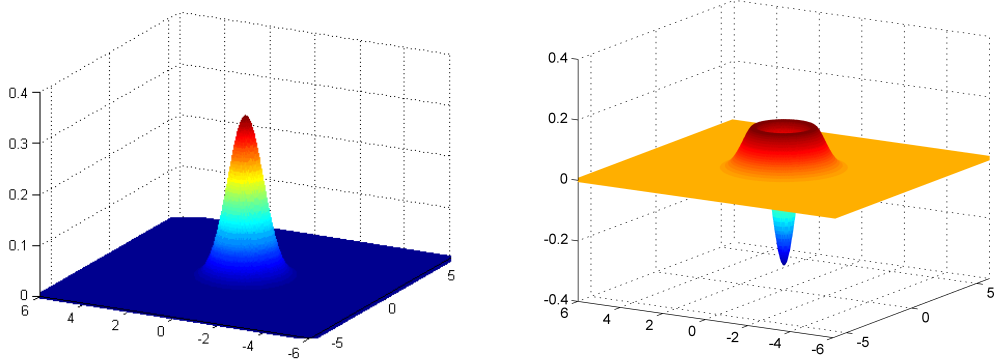


Figure 2.1: Left: Wigner function for coherent state. Right: Wigner function of a single photon Fock state.

A similar concept can be introduced in quantum optics. We use the quadrature states described earlier to define the following function, known as the Wigner function, for a single mode state defined by density matrix $\hat{\rho}$ ^[17,30]:

$$W(q, p) = \frac{1}{2\pi} \int_{-\infty}^{\infty} e^{-ipx} \left\langle q - \frac{x}{2} \right| \hat{\rho} \left| q + \frac{x}{2} \right\rangle dx \quad (2.56)$$

We note that this expression can be generalised to also define Wigner functions for multimode states.

The Wigner function has several properties that allow it to be interpreted as an extension of a probability distribution. First, the Wigner function is real and its integral over phase space is normalised. Furthermore, its marginal distributions correspond to the probabilities of measuring the corresponding quadrature values:

$$\langle q | \hat{\rho} | q \rangle = \int W(q, p) dq, \quad \langle p | \hat{\rho} | p \rangle = \int W(q, p) dq \quad (2.57)$$

In addition, the Wigner function for a coherent state $|\alpha\rangle$ is:

$$W(q, p) = \frac{1}{\pi} \exp[-(q - q_0)^2 - (p - p_0)^2] \quad (2.58)$$

where we use $\sqrt{2}\alpha = q_0 + ip_0$. This Wigner function is indeed centred around the (q_0, p_0) coordinate corresponding to the classical description of a plane wave, but now incorporates the quantum mechanical uncertainty on the two quadratures. A Wigner function for a coherent state is shown in Fig. 2.1.

There are some differences between the Wigner function and a classical probability distribution. Whereas the marginals of the Wigner function correspond to physical quantities that can be measured, the Wigner function itself does not correspond to a physical quantity. $W(q, p)$ has a well defined value, but the two quadratures do not simultaneously have well defined values due to the uncertainty principle 2.16. The Wigner function therefore does not have to be positive, and is indeed negative in places for a large variety of states such as non-vacuum Fock states. The Wigner function for a single photon Fock state is shown in Fig. 2.1.

The Wigner function is particularly useful because of the following overlap formula. For any two operators \hat{F}_1 and \hat{F}_2 with the corresponding Wigner functions W_1 and W_2 we have:

$$\text{tr}(\hat{F}_1 \hat{F}_2) = \int W_1(q, p) W_2(q, p) dq dp \quad (2.59)$$

The Wigner function can thus be used to calculate a wide range of physically relevant quantities such as expectation values, transition probabilities, and purities of quantum states^[17].

2.5.2 P function

The Wigner function is one specific instance of a class of quasiprobability distributions; here we study the P-function, mentioned earlier during our discussion of coherent states, in more detail^[17]. We define a function $\tilde{P}(u, v) = \tilde{W}(u, v)e^{\frac{1}{4}(u^2+v^2)}$ where \tilde{W} is the Fourier transform of the Wigner function. We then have:

$$W(q, p) = \frac{1}{\pi} \int_{-\infty}^{\infty} \int_{-\infty}^{\infty} P(x, y) \exp[-(q - x)^2 - (p - y)^2] dx dy \quad (2.60)$$

where P is the Fourier transform of \tilde{P} . The Wigner function is therefore a convolution of P with the Wigner function of a coherent state, so this expression can be seen as decomposing the Wigner function into a coherent state basis. P therefore corresponds to the P-function defined in equation 2.26. Once again, we stress that the P function is only a regular function (or not more singular than a delta function) if the underlying state can be treated as a mixture of coherent states, in which case the state is considered classical. If the P function is more non-regular than a delta function, then we refer to the state as being non-classical.

The use of the P-function to determine whether a state is classical or not is justified by considering the classical simulability of quantum optics experiments. Separable measurements on an optical state described by a regular P function are efficiently simulable using a classical computer^[31], whereas it can be shown that some separable measurements on some states with non-regular P functions cannot be efficiently simulated on a classical computer. For example, photon number measurements on states produced by sending single photons into a large interferometer cannot be efficiently simulated classically. We discuss this in more detail later when we describe boson sampling.

2.5.3 Gaussian states

A class of states of particular relevance to this thesis is Gaussian states. A Gaussian state is defined as having a Gaussian Wigner function. Vacuum, squeezed states, and coherent states all are Gaussian states.

Furthermore, any optical transformation described by a Hamiltonian that is at most quadratic in the creation and annihilation operators transforms a Gaussian state into another Gaussian state. Such a transformation is known as a Gaussian transformation. That an at most quadratic Hamiltonian conserves the Gaussian nature of a state can be understood using our previous discussion of Bogoliubov transformations in quantum optics. Any such transformation can be decomposed into a sequence of squeezing operations, rotations, and displacements. In the single mode case, these squeezing, rotation (i.e. a phase shift in the single mode case), and displacement operations affect the Wigner function as follows:

$$\text{Squeezing } r : W(q, p) \rightarrow W(qe^{-r}, pe^r) \quad (2.61)$$

$$\text{Phase shift } \phi : W(q, p) \rightarrow W(q_\phi, p_\phi) \quad (2.62)$$

$$\text{Displacement } \alpha : W(q, p) \rightarrow W(q + q_0, p + p_0) \quad (2.63)$$

These transformations all perform linear transformations on the quadratures and thus maintain the Gaussian nature of the state. Similar expressions can be derived in the multimode case^[17]. In addition, homodyne measurements project an optical state onto a quadrature state, which can be considered a Gaussian state in the limit of infinitely high squeezing. This observation allows us to also introduce the notion of a Gaussian measurement, which projects an optical state onto a Gaussian state.

2.5.4 Gaussian state formalism

Gaussian states and Gaussian transformations acting on Gaussian states are particularly easy to describe. A Gaussian distribution over N variables is entirely characterised by its length N vector of first order moments and its $N \times N$ matrix of second order moments, known as the covariance matrix. An N -mode Gaussian state can therefore be described using its length $2N$ “displacement vector” and its $2N \times 2N$ covariance matrix. The factor of 2 stems from the fact that each mode has two quadratures.

Since Gaussian transformations perform linear transformations on the quadratures, a Gaussian transformation can be described by a simple transformation of the displacement vector and covariance matrix of the state. Specifically, if a state $\hat{\rho}$ is described by displacement vector \mathbf{d} and covariance matrix \mathbf{M} , and a unitary transformation acting on the Hilbert space of the state is Gaussian and is described by a matrix \mathbf{S} acting on the quadratures, then the displacement vector and covariance matrix are transformed as follows:

$$\mathbf{d} \rightarrow \mathbf{S}\mathbf{d} \quad (2.64)$$

$$\mathbf{M} \rightarrow \mathbf{S}^T \mathbf{M} \mathbf{S} \quad (2.65)$$

Gaussian measurements can also be described using this formalism. Furthermore, some non-unitary transformations such as loss and phase-insensitive gain can also be described as Gaussian transformations and be included in this formalism. A list of the transformations corresponding to squeezing, homodyne measurement, loss, and phase insensitive gain can be found in appendix A.

The Gaussian state formalism allows for a practical description of optical states since

any sequence of Gaussian operations and measurements acting on Gaussian states can be accounted for using a number of operations that scales polynomially with the number of modes. One consequence of this fact is that such a sequence can be efficiently simulated using a classical computer^[32].

The photon number statistics of a Gaussian state can also be determined directly from its displacement vector and covariance matrix^[33]. However, Fock states are not Gaussian and in this case the algorithm for doing so scales exponentially with the number of modes.

2.6 Conclusion

In this chapter, we provided a quantum description of light that will be used in the rest in this thesis. We reviewed some particularly useful states of light, modal transformations, and measurements. We also discussed the notion of quasiprobability distributions through the Wigner and P functions, which allowed us to introduce the concept of Gaussian states and the Gaussian state formalism. In the following chapter, we build on these foundations to introduce the field of linear quantum optics.

Chapter 3

Introduction to Linear Optics

A commonly used framework within quantum optics is linear quantum optics, in which large multimode quantum states of light are created by optical interference of single mode quantum states. The modes populated by this multimode quantum state are then typically measured separately. Measurement and feedback mechanisms, as well as the use of initially entangled states, can also be included within this framework. A schematic of a typical linear quantum optics experiment is shown in figure 3.1. Despite the simplicity of this framework, linear optical schemes are able to generate a wide variety of different states of

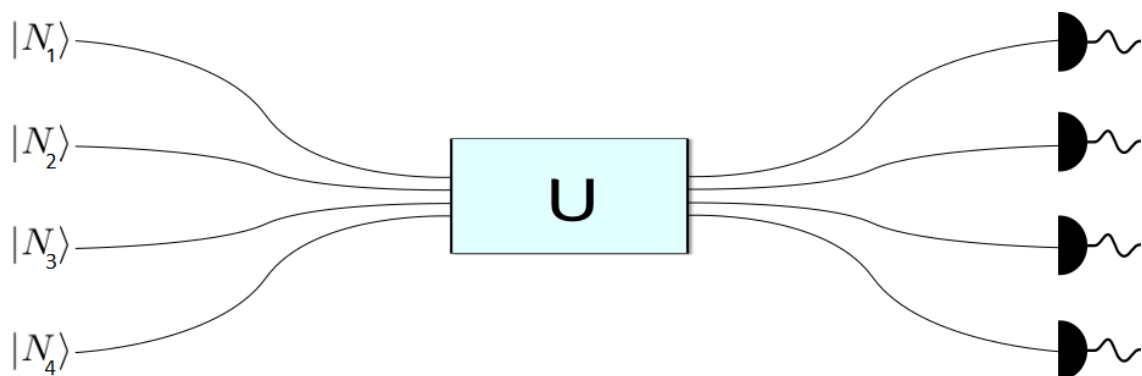


Figure 3.1: A schematic of a typical linear optics experiment. Single mode states of light (such as the Fock states represented here) are prepared, interfered with each other, and then measured.

light and have several applications. For example, any multimode pure Gaussian state can be generated using linear optics by sending squeezed and displaced single mode states into an interferometer^[34]. Furthermore, many experimental tools have been developed for linear optics, so that experiments in the field can often be readily performed. In the following, we review some applications of linear quantum optics.

3.1 Applications of linear optics

3.1.1 Fundamental studies in quantum physics

Linear optics has been used as a platform with which to investigate fundamental properties of quantum physics. For example, studies into violations of Bell's inequalities have often been performed using entangled photon pairs^[3,18–20], as have investigations into the nature of the wavefunction^[35]. Quantum teleportation has also first been demonstrated within this framework^[36,37]. Several phenomena that are specific to quantum optics (and analogous bosonic systems) can also be investigated using linear optics. Non-intuitive photonic interference phenomena between two^[38] and more^[39,40] photons have thus been demonstrated.

3.1.2 Metrology

Linear optics can be used to develop high precision measurement systems. Measurement schemes using classical light are hampered by the uncertainty on the quadrature and photon number uncertainty on coherent states, which imposes a precision limit known as the shot noise limit. Measurement schemes using quantum states of light can outperform the shot noise limit, by choosing states that either have a smaller photon number uncertainty or a smaller quadrature uncertainty. For example, NOON states of light, consisting of two modes

populated with exactly N photons in an equal superposition of all being in one mode and all being in the other mode, can be generated using linear optics and used to perform phase measurements using fewer resources than would be possible with classical light^[41]. A linear optical scheme using squeezed light can similarly be used to reduce the noise in a phase measurement^[42].

These ideas in quantum metrology have been applied in several fields. Measurements beating some classical limits have been demonstrated in measurements of atomic spin ensembles^[43] and biological samples^[44,45]. Furthermore, the sensitivity of gravitational wave detectors^[46], which at present consist of an optical interferometric setup, is expected to be improved by the use of squeezed light at one input of the interferometer^[7].

3.1.3 Quantum information processing

Information processing systems that make use of quantum phenomena such as entanglement and superposition can outperform classical information processing systems. Informally, this is because the physical state of a classical computer containing N bits can always be described using N numbers (such as the string of 0s and 1s describing the state of the N bits), whereas the state of a quantum computer with N “qubits” is described by 2^N complex amplitudes. Some algorithms, such as factorisation^[47], can in principle be solved in polynomial time using a quantum computer whereas the best known classical algorithms would require exponential time. A major research objective in the field of quantum physics is the construction of a “universal quantum computer”, that would be the quantum equivalent of current reprogrammable classical computers. Given the experimental complexity of building a quantum computer, to date only small-scale quantum computers have been

realised^[15,48,49].

Linear optics can be used to perform quantum computation tasks. In principle, universal quantum computation can be performed by a linear optical device with single photon inputs and feed-forward, using what is known as the KLM scheme^[50]. Alternative routes to universal quantum computation using linear optics have also been explored, for example using photonic cluster states^[51] or squeezed state inputs^[52]. Recent advances have also been able to account for experimental imperfections such as losses in these schemes^[53,54]. There still is a considerable gap between theoretical proposals for universal quantum computation using optics and what is experimentally feasible, but the obstacles do not seem insurmountable^[55].

Although universal quantum computation with photons is still a somewhat distant prospect, some more limited but more accessible quantum information tasks can be addressed using linear optics. These include analog simulations of quantum walks^[56–59], spin systems^[60], and noise-assisted transport^[61]. Another task that we discuss in the following is boson sampling.

3.1.4 Boson sampling

That quantum computers can outperform classical computers for some tasks is already widely believed to be true. However, two obstacles stand in the way of a definitive experimental demonstration of such a “quantum advantage”. First, many tasks for which quantum computers are believed to be more powerful, such as factorisation, have not been proven hard to perform on classical computers. Secondly, the quantum computers that have been demonstrated to date hold insufficient computing power to outperform modern-day

classical computers.

Boson sampling^[62] is a computational task that is designed specifically to provide an experimental demonstration of a quantum advantage for a task the computational hardness of which is well understood. Boson sampling is provably hard to perform on a classical computer, assuming a couple of reasonable conjectures. However, boson sampling can in principle be performed efficiently using a linear optics device which is much easier to construct than a universal quantum computer.

Boson sampling is defined as follows. We are given a set of M optical modes, $N \ll M$ of which are populated with single photon Fock states. We perform an M -mode rotation on these modes described by a Haar-random unitary matrix U . The computational task consists of drawing a sample from the photon number distribution of the output modes. It is clear that a linear optics experiment can straightforwardly implement this computational task in a single experimental run consisting of single photon state preparation, interference, and photon number measurements. However, using a couple of reasonable assumptions it has been shown that a classical computer cannot produce such a sample in a time that scales polynomially with N .

Directly implementing the original proposal by Aaronson and Arkhipov^[62] is quite challenging, so several variations have been proposed. The original proposal requires several tens of photons, which is not achievable with current photon source technology. It has since been shown that quantum states of light that may be easier to produce can be used instead while maintaining the computational complexity of the task. A collection of two mode squeezed vacuum states can for example be used instead of single photons^[63,64], as can single mode squeezed vacuums^[65]. These two proposals are respectively known as scattershot boson

sampling and Gaussian boson sampling. The quantum states can also be generated within the interferometer^[66].

In addition, there is ongoing discussion concerning the conditions under which an experimental boson sampler outperforms a classical computer. First, imperfections in quantum experiments can cause these experiments to be classically simulable^[67]. It has for example been shown that the photons in boson sampling must be close to indistinguishable^[68], and that optical losses must scale favourably with the number of photons^[69]. Moreover, verifying that a boson sampling device is indeed performing the desired task is another problem that has been studied in several different ways^[70–72]. Finally, the number of photons that is required to demonstrate a quantum advantage is also a matter of discussion, with estimates ranging from 30^[62] to 50^[73] photons.

Small-scale experimental demonstrations of boson sampling were realised soon after the development of the theoretical proposal^[74–77]. Improvements since then have included the use of deterministic photon sources^[78–80] and implementations of scattershot boson sampling^[81]. Experimental issues such as loss and mode matching remain, and the largest number of photons achieved in these experiments to date is 5 photons^[80].

3.1.5 Linear quantum optical networks

An important concept that extends that of linear optics is that of a quantum optical network^[82,83]. A quantum optical network consists of linear optical elements connecting spatially separated quantum nodes, which may be quantum optical components such as sources and detectors or material systems such as trapped ions^[84] and quantum memories^[85]. Such a network can produce long range and large scale distributed entanglement between these

quantum nodes. These networks can be used for a wide range of applications. They enable multi-user quantum key distribution^[86]. A quantum network of clocks that share entangled resources has been proposed^[87] as a precise worldwide time reference. Moreover, quantum systems consisting of spatially separated ion traps connected to each other with optical links are a strong contender for building a universal quantum computer^[84]. For these systems, linear optics may prove useful not only for distributing entanglement, but also for providing some degree of complementary processing such as entanglement distillation^[88].

A desirable design requirement for linear optical systems is therefore that they be compatible with a quantum network. It should be possible to interface them with other quantum systems. A particularly practical component for building these networks is optical fibre due to its extremely low optical loss over long distances. Components for linear optical systems should therefore ideally be fibre-coupled. Furthermore, they should allow for some degree of reconfigurability so that they can be used for different applications with a wide range of systems.

3.2 Technology for linear optics

The last few years have seen many advances in the development of linear optical systems, from experiments capable of generating a million entangled modes^[89] to the teleportation of quantum states between Earth and a satellite^[90]. These advances have been due in part to the development of better quantum light sources, interferometers, and detectors. In the following, we describe some approaches to building these components.

3.2.1 Quantum light sources

Crucial to linear optics is the development of sources of non-classical light. The sources that are relevant to this thesis can be divided into two categories: generators of single photon Fock states and generators of squeezed light.

Single photon sources

The two most commonly used approaches for generating Fock states are artificial atoms and heralded light sources.

When excited, a single atom typically emits a single photon, which can then be used for linear optics experiments^[91]. However, the coupling efficiency between a single atom and an optical fibre is usually quite low, which limits the usefulness of this scheme. A promising alternative scheme for producing single photons is the use of artificial atoms such as quantum dots in a cavity. Highly indistinguishable photons have thus been extracted from such cavities with efficiencies close to 30%^[92,93], and have for example been used for boson sampling experiments^[80]. There is ongoing work on improving both the indistinguishability of the photons produced in this way and the extraction efficiency.

Single photons can also be produced using correlated light fields, such as a two mode squeezed vacuum. As seen earlier, the photon numbers in the two modes of a TMSV are perfectly correlated, so that the detection of a single photon in one mode heralds the presence of a single photon in the other mode. Heralded photon sources have been able to reach coupling efficiencies of up to 90% into fibre^[19] and very high indistinguishabilities^[94]. However, the generation of a single photon is probabilistic, with a maximum probability of 25%^[95]. The possibility of generating more than one photon is also problematic. These

issues can be mitigated using source multiplexing schemes^[96].

Squeezed light sources

Squeezed light, such as TMSVs and SMSVs, can be produced by focusing pump light into a nonlinear material. Pump photons are then converted into signal and idler photons at frequencies and in directions that satisfy both conservation of momentum and conservation of energy. If the initial state of the signal and idler modes is vacuum and signal and idler are different then this process generates a TMSV; if they are identical then a SMSV is generated. TMSVs are easier to produce since they have less stringent mode matching requirements.

Since the same setup produces both TMSVs and heralded single photons, TMSVs can also be coupled into fibre with very high efficiency and high indistinguishability. Squeezing levels of greater than 10 dB for continuous light have been observed^[97,98], whereas squeezing of about 5 dB has been observed for pulsed light^[99], corresponding to a few tens of photons on average^[100]. To generate pulsed squeezed light, both bulk nonlinear materials and waveguides are used, with bulk materials typically generating higher coupling efficiencies and waveguides generating higher squeezing.

3.2.2 Integrated photonics

There are many ways of providing the optical interference that is required in linear optics schemes. For example, both bulk optics^[80] and fibre networks^[80] have been used in boson sampling experiments. In the following, we focus our discussion on integrated photonics, which is of particular relevance to this thesis.

Integrated photonics has emerged in the last few years as a promising platform for linear optics. In addition to providing interference, state of the art photon sources^[101,102],

interferometers^[103,104] and detectors^[105] have all been demonstrated on chip, as have several experiments such as boson sampling^[74] and quantum teleportation^[37]. In the following, we motivate the use of integrated photonic devices for linear optics, and provide an overview of recent work in the field.

Why use integrated photonic devices

An important challenge faced by linear optics is that of scaling up to a large number of modes that are very well matched and phase stable. Early experiments in quantum optics relied on bulk optics in free space. However, bulk optics take up a lot of space, mode matching is difficult especially if light has to propagate long distances, and active phase stabilisation is often required. Furthermore, state of the art superconducting detectors are fibre coupled, and losses occur at the interface between fibre and free space. Alternatives to free space bulk optics are therefore sought after. For example, fibre networks have been used for linear optics applications^[106]; however, there is no obvious route to achieving phase stability or scaling to a large number of modes.

Integrated photonics has emerged as a promising platform with which to address these issues. Single mode optical waveguides and other optical components can be etched or written into a monolithic substrate. Because a single waveguide is typically a few microns across, a large density of optical components can be included into a centimeter-sized chip. Furthermore, the small size of photonic chips and their integration into a single substrate guarantee phase stability on the nanometre scale. The optical waveguides can also be made to high precision to ensure good mode matching.

Desiderata for integrated photonic devices

Despite the promise of integrated photonics, some challenges remain to be overcome. To understand these challenges, we first review the desiderata for integrated photonic devices.

- *Density:* Higher densities of components on a chip lead to better scaling prospects, as well as to lower propagation loss. Since optical waveguides must be routed from one optical element to another for on-chip applications in linear optics, the maximum bend radius r determines how close the optical elements can be to one another. This bend radius is in turn determined by the refractive index contrast between the waveguide and the surrounding material. The maximum density of components on a chip can therefore be quantified by $1/r^2$ ^[107].
- *Loss:* Quantum information with photons is very vulnerable to loss, so low loss is an important requirement. Typical sources of loss in photonic chips include propagation loss due to scattering at the boundary of the waveguide^[108], bending losses, or losses at optical elements such as beam splitters. Propagation loss is typically expressed in dB/cm. However, the most relevant figure of merit for propagation loss is loss compared to the density of optical elements. If there is a high density and photons do not need to propagate far on the chip, then propagation loss is less of an issue than if photons need to propagate long distances. This figure of merit can be quantified by $1/\alpha r$ ^[107], where α is the loss per centimeter and r is the bend radius, which is related to the density of optical elements as described above.
- *Coupling:* For integrated chips to be used as part of a larger fibre-coupled quantum network, good coupling to optical fibre is required.

- *Integration with sources and detectors:* Integrating several linear optical components such as sources, waveguides, and detectors all on a single chip is a promising route for scaling linear optics to a larger number of modes and photons. Furthermore, on-chip integration ensures good mode matching and therefore potentially lower loss. However, integrating different components on the same platform can be difficult due to their differing requirements. For example, superconducting detectors demand cryogenic temperatures, whereas photon pair sources based on nonlinear processes require strong pump fields which can leak through to the detectors or cause a significant amount of heat from absorption.
- *Reconfigurability:* To perform experiments that cover the entire range of linear optics, we require that the optical circuits be reconfigurable. Reconfigurable circuits can be used, for example, to implement the universal multiport interferometers discussed in the following chapter. Furthermore, given the fast repetition rates of a few tens of MHz of current pulsed light sources, ideally photonic circuits should be reconfigurable on those same time scales.

Several different materials have been proposed for building photonic chips. However, no material has yet emerged that simultaneously meets all the requirements described above. In the following, we review the state of the art in some of the material platforms that have featured prominently in recent quantum optics experiments: silicon, lithium niobate, and silica. This discussion is intended to highlight some of the tradeoffs that must be made when choosing a material platform, and we therefore choose to focus on three materials with different properties instead of making an exhaustive list. Indeed, silicon nitride, indium phosphide and gallium arsenide for example are also promising for linear optics but will not

be discussed here.

Silicon photonics

Silicon is the material of choice for integrated electronic circuits, and its processing is therefore backed by the skills and expertise of a multi-billion pound industry. The field of silicon photonics can harness this industry to deliver complex photonic devices. Furthermore, silicon has several advantages as a photonic material. Silicon waveguides exhibit low propagation losses as low as 0.3 dB/cm in the telecom band^[109]. In addition, silicon and its oxide, silica, have a large refractive index contrast which allows for a very high density of optical elements. For these reasons, and for the potential of integrating electronic and photonics on a single platform, silicon photonics is already a proven technology within the classical communications domain^[110].

Silicon quantum photonics is a burgeoning field^[107]. In particular, the density of optical components that can be integrated on a single chip has surpassed that of any other platform. The largest reconfigurable integrated circuits for quantum optics to date have been constructed in silicon, involving 26 modes, 88 Mach-Zehnder interferometers, and 176 phase shifters, with a total of 20% facet-to-facet loss^[59,104]. Furthermore, integration with photon sources^[102], delay lines^[111], low loss and fast modulators^[112], filters^[113], and detectors^[114] have all been separately demonstrated.

A significant drawback of silicon photonics is that coupling losses from silicon to optical fibre are typically high due to the large mismatch in mode size and refractive index. The lowest reported coupling losses are less than 1 dB with well engineered devices^[115,116]; however, losses of about 3 dB are still common. This is a strong incentive for pursuing

entirely on-chip integration of optical components in silicon. Furthermore, although low loss and fast modulators do exist for silicon, their development is still in its infancy. This is because whereas most fast and low loss modulators to date in other materials rely on an electro-optic effect via a χ_2 nonlinearity, silicon is a centro-symmetric material and has a χ_2 of 0. Therefore, integration of silicon with other materials^[112] or first inducing a χ_2 into silicon using strain for example are necessary^[117]. We note that classical silicon photonics typically uses modulators that rely on locally changing the concentration of charge carriers^[118], but these modulators are unsuitable for quantum optics because they introduce loss.

Lithium niobate photonics

Lithium niobate (LiNbO_3) has also attracted significant interest within the quantum optics community^[119]. Like silicon, lithium niobate is commonly used within the classical photonics industry^[120], so mature fabrication technologies are available. Some advantages of lithium niobate over other materials are: simple writing of waveguides and beam splitters using titanium indiffusion for example^[121], strong χ_2 nonlinearity that enables straightforward integration of high efficiency photon pair sources and fast electro-optic modulators^[122], propagation losses smaller than 0.1dB/cm ^[119], and coupling losses to single mode fibre smaller than 0.4 dB ^[123].

Due to its strong nonlinearity, investigations of lithium niobate have largely focused on its use as a source of quantum states of light. It has been used as a source of: heralded single photons with 60% efficiency^[124], entangled photon pairs^[125], squeezed states^[126], and photon triplets^[127]. These sources have been interfered in tunable circuits^[121]. Lithium

niobate has also been shown to be compatible with superconducting detectors^[128,129], and quantum memories^[130].

One drawback of lithium niobate is that the refractive index contrast between waveguides and the surrounding material is not as high as in silicon, so that acceptable bend radii are several mm^[131]. This limits the density of optical elements that can be written on a chip and increases the impact of propagation loss. Furthermore, the fabrication process for low loss waveguides in lithium niobate can be challenging, often resulting in higher loss than anticipated^[122,132].

Silica photonics

Silica photonic devices are interesting for quantum optics mainly because of their intrinsic compatibility with optical fibre. Optical fibres are made of silica and have loss of less than 0.2 dB/km. Many commercially available optical components are designed to be fibre coupled. Optical fibres can therefore be used as a particularly convenient way to connect photon sources to circuits and then to detectors. Silica photonic circuits, being made of the same material, have been demonstrated to have low propagation losses of less than 0.3 dB/cm^[133] and coupling losses of less than 0.2 dB to fibre^[134]. Furthermore, several methods exist for making silica photonic chips. Femtosecond laser-written chips^[135] can adopt complex 3D geometries, whereas etched silica waveguides^[136] and UV-written waveguides^[137] can be written on top of a silicon substrate that can dissipate heat from thermo-optic phase shifters, for example.

Due to low loss at the chip to fibre interface, silica photonic chips have mostly been used in the quantum optics community in conjunction with other fibre coupled components.

Experiments with silica chips have therefore been able to make use of state of the art photon sources and detectors, that are typically designed to couple into fibre. Examples include a 6 mode fully reconfigurable interferometer that was fibre coupled to a photon source and to detectors and was used to performed a wide range of experiments^[103], as well as some other reconfigurable circuits used to demonstrate boson sampling^[74] or quantum teleportation^[37]. Furthermore, silica photonic circuits have been shown to be compatible with photon sources^[101] and detectors^[105].

Silica photonic circuits have a few drawbacks. Chief among them is that the allowable density of optical components is very low due to the small refractive index contrast, typically about 10^{-3} , between waveguides and the surrounding material. This low density also increases the impact of propagation loss. Furthermore, silica has very small nonlinearities, so fabricating fast modulators is an issue.

3.2.3 Photon detectors

Many schemes exist for performing measurements on optical modes, which include the homodyne and photon counting measurements discussed earlier. In the following, we focus on photon counting measurement devices. We first describe what qualities are expected from an ideal photon detector, and then discuss how three commonly used detectors compare to this ideal detector. The detectors we discuss are single photon avalanche diodes, superconducting nanowire single photon detectors, and transition edge sensors.

Desiderata for photon detectors

An ideal photon detector should have the following qualities. Despite recent advances in photon detection technology, no current detector has all of these qualities simultaneously.

At present, different types of detectors exist that have their own specific advantages and disadvantages, so that different detectors are used for different applications.

- *High Efficiency:* Every incident photon should lead to a signal on the detector. The proportion of incident photons that cause a signal is what defines the efficiency.
- *No Dark Counts or Afterpulsing:* Every signal on the detector should correspond to an incident photon. The frequency at which the detector outputs a signal without there being an incident photon is called the dark count rate. Some detectors also suffer from afterpulsing, which is an undesirable effect whereby an additional spurious detection signal can appear just after a detection event.
- *Photon Number Resolution:* Different numbers of photon should lead to different detector responses. Some detectors are binary in that they produce a “click” if there is one or more photons and “no click” if no photon was detected; these detectors are called click detectors.
- *Short Dead Time:* After a detection event, the detector should reset as quickly as possible to detect any subsequent photons.
- *Low Timing Jitter:* The time of arrival of a photon should be known to a high level of precision.
- *Ease of Use:* A photon detector should be compact and easy to use so that it can be used in many different situations, including outside of a laboratory environment.

Single Photon Avalanche Diodes

A single photon avalanche diode (SPAD) consists of a reverse biased semiconductor p-n junction that is biased above the breakdown voltage of the device. When a photon is absorbed, a bound electron in the depletion layer breaks loose, and an avalanche reaction occurs as the resulting electron and hole dislodge other electrons and holes in the material. This effect causes a measurable current through the device. Resetting the SPAD involves quenching the avalanche process by lowering the voltage across the junction to below the breakdown voltage.

SPADs are click detectors that are typically compact, easy to use, and can have low timing jitters of less than a hundred picoseconds. Their efficiency, dark count rate and dead time depend on the material and the bias voltage. Silicon is typically used for wavelengths below 1100 nm, and efficiencies of about 70% can be achieved with dead times of a few tens of nanoseconds and dark count rates of a few hundred Hz in commercial devices. Wavelengths above 1100 nm are above the silicon bandgap, so InGaAs SPADs are used. Commercial InGaAs detectors have typical efficiencies of about 20% with dead times of about 10 μ s and dark count rates of at least a few hundred Hz.

Until recently, InGaAs SPADs were the only detectors available for the telecom range. The poor performance of these detectors limited the use of the telecom range in quantum optics, despite the advantages of this range in terms of the availability of high quality and low loss equipment provided by the telecommunications industry. However, in the last few years, high-efficiency superconducting photon detectors have been developed which make the telecom band much more attractive for quantum optics.

Superconducting Nanowire Single Photon Detectors

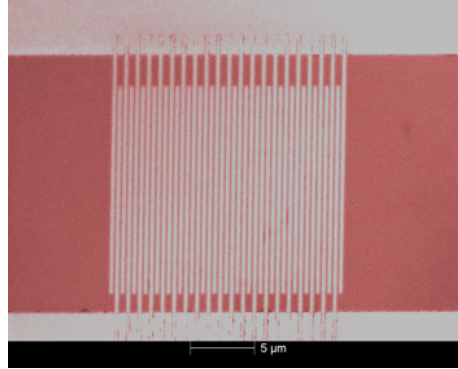


Figure 3.2: Scanning Electron Microscope image of a superconducting nanowire single photon detector, consisting of a meandering strip of superconducting material. Image credit: National Institute of Standards and Technology.

A superconducting nanowire single photon detector (SNSPD)^[138] is a strip of superconducting material that is typically about 100 nm wide and 5 nm thick and laid out in a meandering pattern to cover the area of the optical field to be measured (see Fig. 3.2. It is placed inside an optical cavity designed to maximise absorption at a target wavelength, and is biased with a current a bit below its critical current. Photon absorption creates a localised hotspot that is sufficient, in combination with the bias current that causes additional heating, to make the nanowire locally resistive^[139]. This causes a measurable voltage spike.

SNSPDs are click detectors with very low jitter of tens of picoseconds^[140], short dead times of a few tens of nanoseconds, dark count rates of about 50 Hz which is mostly caused by background noise photons, and efficiencies as high as 93% in the telecom band^[26]. They must be kept in a cryostat at a temperature of less than a few Kelvin, but this requirement is becoming less and less cumbersome as lighter and more compact cryogenic systems are developed^[141].

Transition Edge Sensors

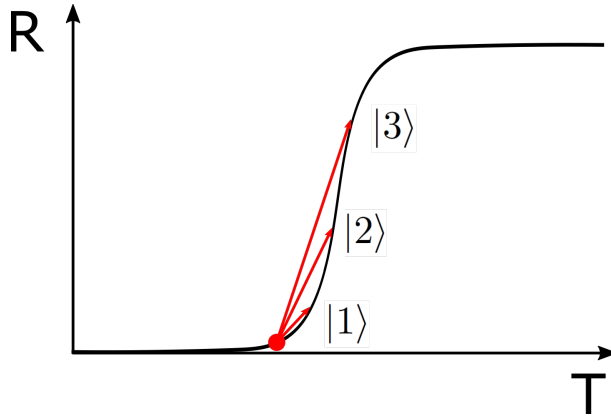


Figure 3.3: Resistance vs. temperature for a transition edge sensor. Photon absorption causes the TES temperature to increase, which leads to an increase in resistance. Different photon numbers lead to different resistance values, so photon number resolution is achieved.

A transition edge sensor (TES) is a small slab of superconducting material that is kept at its transition temperature via an electro-thermal feedback effect^[142], and located inside an optical cavity designed to maximise absorption at a target wavelength. At this transition temperature, the minute increase in temperature caused by absorption of one or more photons leads to a significant increase in the resistance of the TES. This change in resistance can be picked up and amplified using low temperature electronics, which can then be measured at room temperature. After photon absorption, the heat is then dissipated to the environment via a weak thermal link to the TES substrate.

TESs can have efficiencies as high as 98%^[143], and they are photon number resolving with a resolution of a few tens of photons^[144]. They have very low dark count rates which are mostly caused by background photons. However, they have a roughly 5 μs dead time which is the time it takes for the TES to cool down again after absorbing photons, and a typical jitter of a few hundred nanoseconds caused by the high inductance of the superconducting electronics. Furthermore, they have to be operated at very low temperatures of a few

tens of mK so that the signal from the photons is above the thermal noise, which requires expensive and cumbersome cryogenic systems such as dilution refrigerators. The operation of TES detectors is discussed in chapter 6.

3.3 Conclusion

In this chapter, we introduced the field of linear quantum optics, in which large quantum states of light are produced by optical interference of smaller quantum states. We discussed some applications of this field and provided an overview of the technology that is currently available. In particular, this overview discussed some of the shortcomings of these technologies, with a particular focus on integrated photonic circuits and photon detectors. In the following part, we propose new experimental tools which we anticipate will help to overcome some of these shortcomings.

Part II

Components for Linear Optics

Universal Multiport Interferometers

All linear optics schemes require a method of providing the interferometric optical transformation that is required for the chosen task. In many implementations of linear optical schemes, the means of providing this interference is specifically set up for that scheme, and performing a different task requires a new optical setup. However, given the wide range of quantum information processing tasks that can be performed with linear optics, having to use a different interferometer for each task can be a major hindrance. In the same way that the development of classical computers hinged upon the development of the programmable processor, we can expect reprogrammable interferometers to play an important role in the development of linear optics.

A large variety of tasks can already be performed with interferometers with limited reconfigurability. For polarisation modes for example, waveplates allow for controllable single qubit operations that can be used for simulating quantum chemistry^[145], blind quantum computing^[23], solving linear equations^[146], boson sampling^[75], or verifying quantum com-

¹The contents of this chapter relate to the author's publications entitled "Optimal Design for Universal Multiport Interferometers" and "Implementing random unitaries in an imperfect photonic network"

putation^[147]. For spatial modes, several configurations of boson sampling^[74] and quantum teleportation^[37] can be performed on an integrated photonic device containing only a few controllable phase shifters. However, these devices still fall short of providing full reconfigurable interference; they can only implement a small subset of all possible unitary transformations between the number of modes used.

In their seminal work, Reck *et al*^[148] demonstrated a method for providing fully reconfigurable interference between any number of modes, which uses a planar mesh of 2×2 beam splitters and phase shifters. We call such a device a universal multiport interferometer. Reck *et al* provide a convenient analytic mapping between the targeted unitary transformation and the settings of the beam splitters and phase shifters in the mesh that must be implemented to realise the unitary transformation. The use of beam splitters and phase shifters to realise a universal multiport interferometer is particularly convenient since these are simple optical elements the large scale integration of which has already been demonstrated, in particular using integrated photonic technology^[59,104,149]. Continued interest in universal multiport interferometers has led to the development of a new mapping procedure for the same interferometer design^[150,151].

Beyond quantum optics, the development of universal multiport interferometers is also important for applications in the classical domain. Their use has been proposed for microwave photonics^[152,153], optical networking^[154,155], machine learning^[104], and astrophotonics^[156]. This interest in universal multiport interferometers for classical applications stems in part from the perceived potential of photonics to assist conventional computers to perform information processing tasks. The fulfilment of this potential requires the development of programmable optical components to complement programmable computers.

Several realisations of universal multiport interferometers have recently been demonstrated. For example, Carolan *et al*^[103] built a silica photonic chip that can interfere up to six channels, and was used to implement a wide variety of optical quantum information protocols. Ribeiro *et al*^[157] demonstrated a 4×4 silicon device that they use to unscramble light. Perez *et al*^[158] demonstrated a silicon device that can not only act as a universal multiport interferometer, but also perform programmable frequency filtering. In addition, a method for implementing time-bin universal multiport interferometers has been proposed by Motes *et al*^[159]. Both Carolan *et al* and Ribeiro *et al* directly implement the layout of beam splitters and phase shifters proposed by Reck *et al*, whereas Perez *et al* show that their hexagonal layout can also be mapped onto the work by Reck *et al*.

In this chapter, we present an alternative layout of beam splitters and phase shifters that can be used to implement universal multiport interferometers. In the first section, we discuss our proposed layout, and show that it compares favourably to with that by Reck *et al*. In the second section, we discuss how fabrication errors can affect implementations of our design.

4.1 Optimal design for universal multiport interferometers

We first provide an overview of both the design by Reck *et al* (referred to as the Reck design in the following) and of our new design, and discuss some advantages of the latter. We then explain the general principles of our procedure for mapping the targeted unitary transformation to the settings of the beam splitters and phase shifters in the mesh using a 5×5 transformation as an example, and proceed to give a general algorithm. We then discuss some possible physical implementations of our interferometer. Finally, we explain

how a device built according to our design can be characterised so that it can implement our programming scheme.

4.1.1 Background

As discussed in the introduction, an ideal, lossless multiport interferometer between N optical modes performs an optical transformation which can be described by an $N \times N$ unitary matrix U acting on the annihilation operators of the optical modes as $\hat{a}' = U\hat{a}$. Equivalently, in classical optics, U describes the transformation of the electric field amplitudes at the input to those at the output.

Within this framework, the following transformation between channels m and n ($m = n - 1$):

$$T_{m,n}(\theta, \phi) = \begin{bmatrix} 1 & 0 & \dots & \dots & \dots & 0 \\ 0 & 1 & & & & \vdots \\ \vdots & & e^{i\phi} \cos \theta & -\sin \theta & & \vdots \\ \vdots & & e^{i\phi} \sin \theta & \cos \theta & & \vdots \\ \vdots & & & & 1 & 0 \\ 0 & \dots & \dots & \dots & 0 & 1 \end{bmatrix} \quad (4.1)$$

corresponds to a lossless beam splitter between channels m and n with transmittivity $\cos^2 \theta$ ($\theta \in [0, \pi/2]$), and a phase shift ϕ ($\phi \in [0, 2\pi]$) at input m . In the following, we will generally omit the explicit dependence of these $T_{m,n}(\theta, \phi)$ matrices on θ and ϕ for notational simplicity.

Both our scheme and the Reck scheme are based on analytical methods of decomposing the U matrix into a product of $T_{m,n}$ matrices. Specifically, these schemes provide an explicit algorithm for writing any unitary matrix U as:

$$U = D \left(\prod_{(m,n) \in S} T_{m,n} \right) \quad (4.2)$$

where S defines a specific ordered sequence of two-mode transformations, and where D is a diagonal matrix with complex elements with modulus equal to one on the diagonal. A physical interferometer composed of beam splitters and phase shifters in the configuration defined by S , with settings defined by the $T_{m,n}$ matrices, will therefore implement transformation U . We note that D is irrelevant for some applications, but can be implemented in an interferometer nonetheless by phase shifts on all individual channels at the output of an interferometer.

The formalism developed here for unitary transformations describing lossless $N \times N$ interferometers can be extended to include any $M \times N$ linear (non-unitary) transformation. Indeed, it has been noted that any $M \times N$ linear transformation, with for example $M \leq N$ (resp. $M \geq N$), can be either directly embedded within a $2N \times 2N$ (resp. $2M \times 2M$) unitary transformation^[160] to within a scaling factor, or, in a more compact way, implemented by 2 separate $N \times N$ (resp. $M \times M$) interferometers connected to each other via phase and amplitude modulators^[150]. Furthermore, realistic, lossy interferometers can also be included in our formalism simply by rescaling U by a loss factor, as we explain later. Therefore, our design for universal multiport interferometers, as well as that by Reck *et al.*, can be used to implement any linear transformation, to within a scaling factor, on any number of input and output channels. While our design is very general and can be used for any interferometric transformation, more efficient architectures may exist for specific values of N or M when $N \neq M$ (see^[161] for N or $M = 1$, for example) or for specific transformations (see^[162] for implementing Fourier transforms, for example).

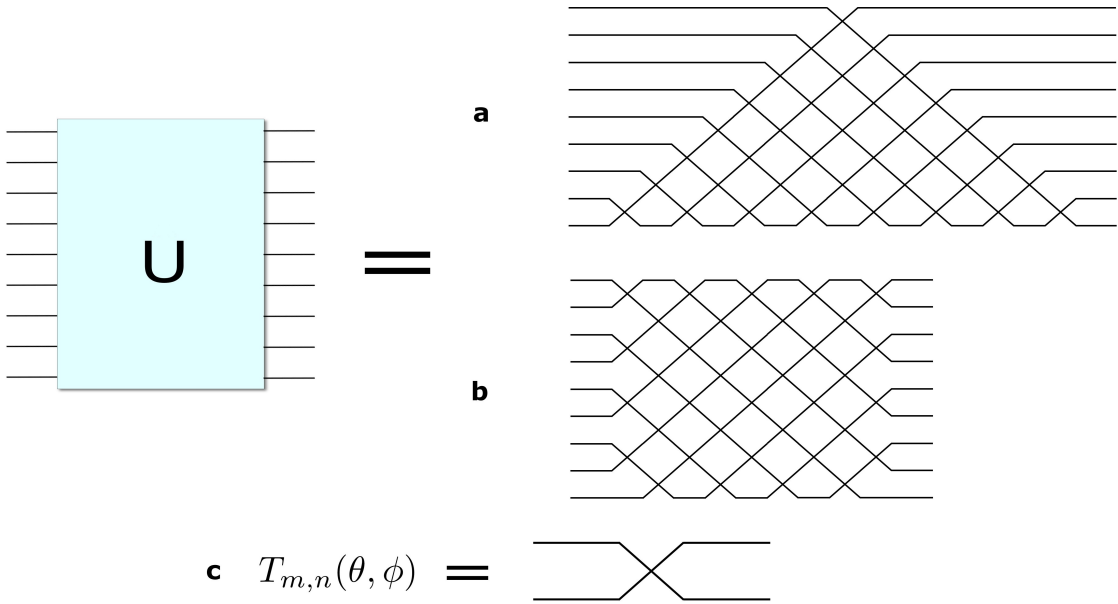


Figure 4.1: A universal N -mode multiport interferometer (shown here for $N = 9$) can be implemented using a mesh of $N(N - 1)/2$ beam splitters such as a) the one proposed by Reck *et al* or b) the one that we propose. As shown in c), a line corresponds to an optical mode, and crossings between two modes correspond to a phase shifter followed by a variable beam splitter, the combination of which is described by a $T_{m,n}(\theta, \phi)$ matrix. Although the total number of beam splitters in both interferometers is identical, our scheme clearly has a much shorter optical depth, and therefore suffers less propagation loss. This reduction in optical depth stems from the fact that each mode crosses its nearest neighbour at the first possible occasion, in contrast to the Reck scheme where the top modes must propagate for some distance before interacting with other modes.

4.1.2 Overview of the two designs

Schematic views of the Reck design and of our proposed design are presented in figure 4.1.

Figure 4.1a presents the Reck design, in which the matrix decomposition method determines a sequence S that corresponds to a triangular mesh of beam splitters. Figure 4.1b presents our design, in which every mode crosses its nearest neighbour at the first possible occasion. Our design has a shorter optical depth and is more symmetric than the Reck design. We note that both interferometers use the same, minimal number $N(N - 1)/2$ of beam splitters to implement an $N \times N$ interferometer^[148].

We define the optical depth of an interferometer as the longest path through the inter-

ferometer, enumerated by counting the number of beam splitters traversed by that path. It is important to minimize the optical depth of an interferometer because the resulting circuits can then be more compact. Furthermore, propagation losses are reduced for an interferometer with smaller depth. It can be seen that our design has the minimal possible optical depth, since every channel crosses its nearest neighbour at the first possible occasion. Specifically, for an $N \times N$ interferometer, the Reck design has an optical depth of $2N - 3$, whereas our design has an optical depth of N . To illustrate this, the longest path through the interferometer shown in figure 4.1a follows the edges of the triangle and crosses $2N - 3 = 15$ beam splitters, whereas the longest paths through the interferometer in figure 4.1b cross $N = 9$ beam splitters. The increased symmetry of our design also leads to significantly better loss tolerance, as discussed in a subsequent section.

4.1.3 Decomposition method

The 5×5 case

In the following, we present our decomposition method, which allows us to constructively calculate the values of the $T_{m,n}$ matrices. Beyond its use in proving that our design is capable of implementing universal interferometric transformations, this method directly provides a recipe for programming such interferometers. If each beam splitter is programmed to implement the transformation described by the corresponding $T_{m,n}$ then the interferometer performs the targeted unitary transformation.

Our decomposition method relies on two important properties of the $T_{m,n}$ matrices. Firstly, for any given unitary matrix U , it is easy to see that there are values of θ and ϕ that make any target element in row m or n of matrix $T_{m,n}U$ zero, as per Reck *et al*^[148].

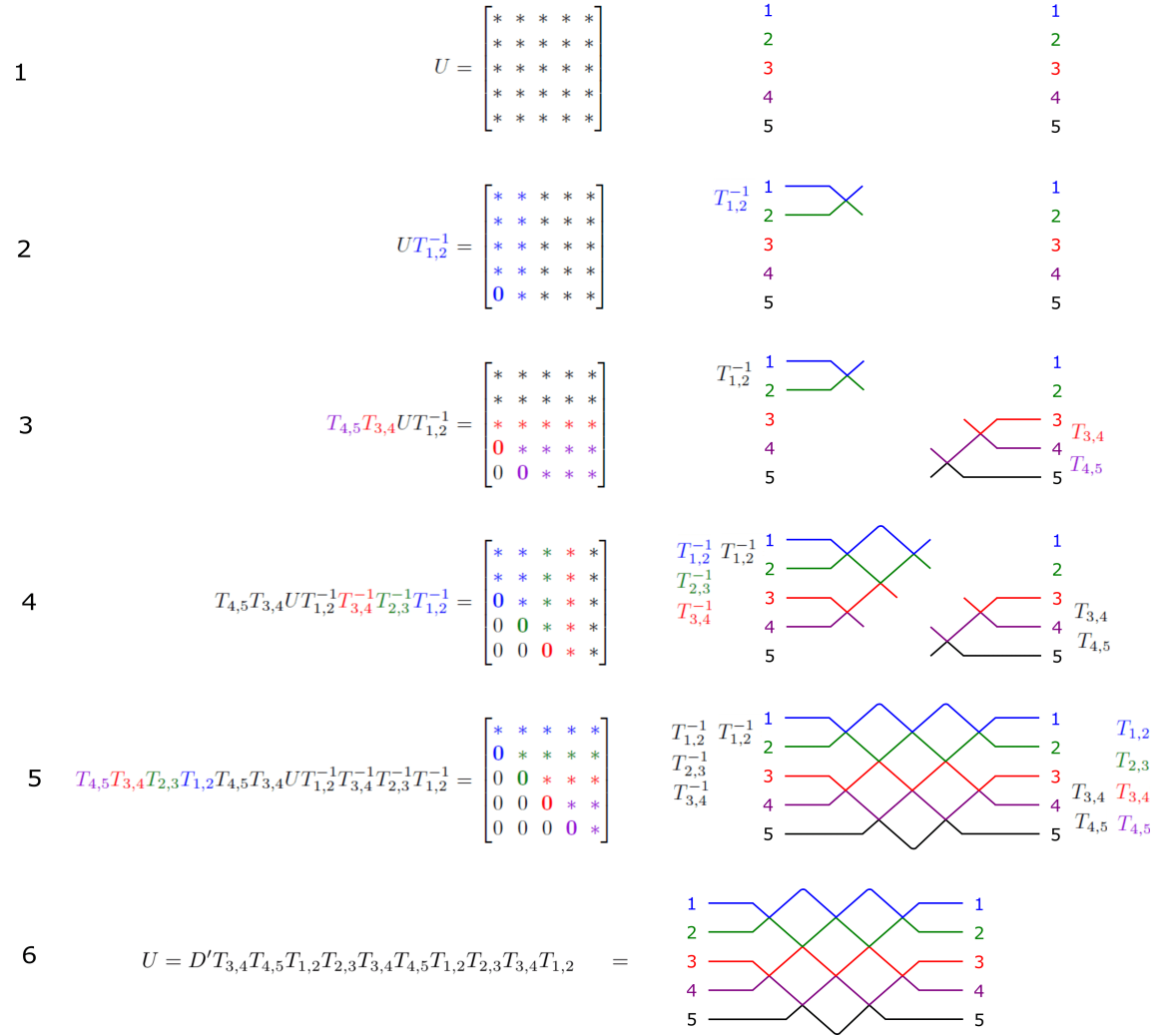


Figure 4.2: Illustration of the algorithm for programming a universal multiport interferometer, for a 5×5 interferometer. The left-hand side presents our decomposition procedure, and the right-hand side shows how our decomposition corresponds to building up the corresponding interferometer. 1) We start with a target unitary matrix U , and a blank interferometer. 2) We first null the bottom left element of U with a $T_{1,2}^{-1}$ matrix, which causes the first two columns of U to mix. This corresponds to adding the top-left beam splitter in the interferometer. 3) We then null the next two elements of this modified U using a $T_{3,4}$ matrix followed by a $T_{4,5}$ matrix, which correspond to the two bottom right beam splitters in the interferometer. $T_{3,4}$ mixes rows 3 and 4, and $T_{4,5}$ mixes rows 4 and 5. Since both the (4,1) and (5,1) elements of U had been nulled, they are not affected by $T_{4,5}$. 4-5) At every step in the algorithm, we null a successive diagonal of the updated U matrix, by alternating between $T_{m,n}$ and $T_{m,n}^{-1}$ matrices, which corresponds to adding diagonal lines of beam splitters to the interferometer. $T_{m,n}$ (resp. $T_{m,n}^{-1}$) matrices of a given color cause the rows (resp. columns) m and n , which are shown in the same colour, to mix, and null the corresponding element of that colour in U . It is clear from this process that once a matrix element has been nulled, no subsequent operation can modify it. 6) After step 5, this modified U has become a lower triangular matrix, which by virtue of its unitarity must be diagonal. We can then write the original matrix U in the way shown here, which by construction exactly corresponds to the desired interferometer.

We will refer to this process as nulling that element of U , and will still refer to the modified matrix after this operation as U . Secondly, we note that any target element in column n or m of U can also be nulled by multiplying U from the right by a $T_{m,n}^{-1}$ matrix.

Our algorithm, shown in figure 4.2 for the 5×5 case, consists of nulling elements of U one by one in such a way that every $T_{m,n}$ and $T_{m,n}^{-1}$ matrix used in the process completely determines both the reflectivity and phase shift of one beam splitter and phase shifter. The sequence of $T_{m,n}$ and $T_{m,n}^{-1}$ matrices must both correspond to the desired order of beam splitters in the interferometer, and guarantee that nulled elements of U are not affected by subsequent operations. In the Reck decomposition, the entire matrix can be nulled using either only $T_{m,n}$ matrices or only $T_{m,n}^{-1}$ matrices while still making sure that nulled elements of U are not affected by subsequent operations. Both types of matrices are necessary to verify this condition in our decomposition. As illustrated in figure 4.2, we null successive diagonals of U by alternating between $T_{m,n}$ and $T_{m,n}^{-1}$ matrices, in such a way that every nulled diagonal in the matrix corresponds to one diagonal line of beam splitters through the interferometer.

At the end of the decomposition process, we obtain the following expression for a 5×5 matrix:

$$T_{4,5}T_{3,4}T_{2,3}T_{1,2}T_{4,5}T_{3,4}UT_{1,2}^{-1}T_{3,4}^{-1}T_{2,3}^{-1}T_{1,2}^{-1} = D \quad (4.3)$$

where D is a diagonal matrix as in equation 4.2. This can be rewritten as:

$$U = T_{3,4}^{-1}T_{4,5}^{-1}T_{1,2}^{-1}T_{2,3}^{-1}T_{3,4}^{-1}T_{4,5}^{-1}DT_{1,2}T_{2,3}T_{3,4}T_{1,2} \quad (4.4)$$

If D consists of single-mode phase-shifts, then for any $T_{m,n}^{-1}$ matrix one can find a matrix D' of single-mode phases and a matrix $T_{m,n}$ such that $T_{m,n}^{-1}D = D'T_{m,n}$. This can be shown as follows. $T_{m,n}^{-1}D$ contains only one element below the diagonal at position (n, m) , and one element above the diagonal at position (m, n) . Similarly to what was done earlier, we can therefore find a $T_{m,n}^{-1}$ matrix that nulls the (n, m) element of $T_{m,n}^{-1}D$ by right multiplication. The resulting $T_{m,n}^{-1}DT_{m,n}^{-1}$ matrix is therefore diagonal by unitarity; we will call it D' . We can therefore write $T_{m,n}^{-1}D = D'T_{m,n}$ (we recall that, with our notation, $T_{m,n}^{-1}$ and $T_{m,n}$ can have different θ and ϕ).

Equation 4.4 can therefore be rewritten as:

$$U = D'T_{3,4}T_{4,5}T_{1,2}T_{2,3}T_{3,4}T_{4,5}T_{1,2}T_{2,3}T_{3,4}T_{1,2} \quad (4.5)$$

which, mirroring equation 4.2, completes our decomposition.

By construction, equation 4.5 physically corresponds to the multiport interferometer shown in figure 4.2, and the values of the θ and ϕ of the $T_{m,n}$ matrices in this equation determine the values of the beam splitters and phase shifts that must be programmed to implement U .

General algorithm

Our unitary matrix decomposition procedure can be generalised to any $N \times N$ unitary matrix. Elements of \hat{U} are consecutively nulled using $T_{m,n}$ or $T_{m,n}^{-1}$ matrices, which physically correspond to beam splitters in the final interferometer, in the pattern shown in figure 4.3. The decomposition is implemented by algorithm 1.

		15
7		14
6	8	13
2	5	9 12
1	3	4 10 11

Figure 4.3: Illustration of the order in which matrix elements of a unitary matrix \hat{U} are nulled. The first element to be nulled is at the bottom left of the matrix. The following elements are then nulled in consecutive diagonals. A black element located in column i is nulled with a $T_{i,i+1}^{-1}$ matrix, and a blue element located in row i is nulled with a $T_{i-1,i}$ matrix.

Algorithm 1 Unitary Matrix Decomposition Algorithm

```

1: procedure DECOMPOSE( $U$ )
2:   for  $i$  from 1 to  $N - 1$  do
3:     if  $i$  is odd then
4:       for  $j = 0$  to  $i - 1$  do
5:         Find a  $T_{i-j,i-j+1}^{-1}$  matrix that nulls element  $(N - j, i - j)$  of  $U$ 
6:         Update  $U = UT_{i-j,i-j+1}^{-1}$ .
7:     else
8:       for  $j = 1$  to  $i$  do
9:         Find a  $T_{N+j-i-1,N+j-i}$  matrix that nulls element  $(N + j - i, j)$  of  $U$ 
10:        Update  $U = T_{N+j-i-1,N+j-i}U$ 

```

After this decomposition procedure, we obtain the following expression:

$$\left(\prod_{(m,n) \in S_L} T_{m,n} \right) U \left(\prod_{(m,n) \in S_R} T_{m,n}^{-1} \right) = D$$

where D is a diagonal matrix corresponding to single-mode phases, and S_L and S_R are the respective orderings of the (m, n) indices for the $T_{m,n}$ or $T_{m,n}^{-1}$ matrices yielded by our decomposition. This can be rewritten as:

$$U = \left(\prod_{(m,n) \in S_L^T} T_{m,n}^{-1} \right) D \left(\prod_{(m,n) \in S_R^T} T_{m,n} \right)$$

As demonstrated earlier, we can then find a matrix D' and $T_{m,n}$ matrices such that the

previous equation can be re-written as:

$$U = D' \left(\prod_{(m,n) \in S} T_{m,n} \right)$$

where S is, by construction, the order of beam splitters corresponding to the desired circuit.

This completes our decomposition.

This algorithm has many uses beyond that of programming a universal multiport interferometer. It can be used to inform the design of fixed interferometric circuits, such as those demonstrated in^[70,81], in which the specific arrangement of beam splitters that corresponds to our design was used to provide instances of random interference. Furthermore, we anticipate that our matrix decomposition method can be used in other physical systems that use mathematical structures analogous to beam splitters and phase shifters, such as ion traps^[163] and some architectures for superconducting circuits^[164,165]. It has also been shown that our decomposition method can be effectively used to address computational issues in machine learning algorithms^[166].

We note that in addition to the method presented here to program a universal multiport interferometer built according to our design, another programming scheme has recently been proposed by Miller^[167]. This scheme requires detectors that pick off and measure light in the waveguides at several places in the circuit, and then progressively configures one beam splitter after another using the measured powers. Similar self-configuring methods have been proposed^[150,151] and demonstrated^[157,168] for the Reck design. These methods can be advantageous for some applications in that they do not require full characterisation of the circuit elements corresponding to the $T_{m,n}$ matrices.

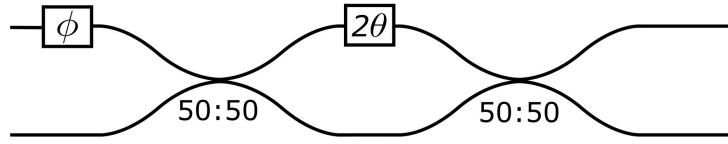


Figure 4.4: A Mach-Zehnder interferometer can be used to implement a variable beam splitter. A variable phase shifter is located between two fixed 50:50 beam splitters. With an additional phase shift at the input of the MZI, this system implements a $T_{m,n}(\theta, \phi)$ matrix.

4.1.4 Some possible implementations

The decomposition procedure described above can in principle apply to any type of optical mode in any platform. Here, we first show how to implement a variable beam splitter using a Mach-Zehnder interferometer, and then discuss methods of implementing our proposed interferometer design in two promising physical platforms: integrated photonics and delay lines.

Reconfigurable beam splitters

Universal multiport interferometers require reconfigurable beam splitters. Direct fabrication of reconfigurable beam splitters is in many platforms not straightforward. A commonly used approach is therefore to use a variable phase shift in between two fixed nominally 50:50 beam splitters in a Mach-Zehnder interferometer (MZI) configuration, as shown in Fig.4.4. If a fixed 50:50 beam splitter is described by the following matrix:

$$\frac{1}{\sqrt{2}} \begin{pmatrix} 1 & i \\ i & 1 \end{pmatrix} \quad (4.6)$$

then the MZI shown in Fig.4.4 containing a 2θ phase shift inside the MZI and an additional ϕ phase shift at the input performs a transformation described by the following matrix:

$$ie^{i\phi} \begin{pmatrix} e^{i\phi} \sin \theta & \cos \theta \\ e^{i\phi} \cos \theta & -\sin \theta \end{pmatrix} \quad (4.7)$$

which, by redefining $\theta = \pi/2 - \theta$ and $\phi = \phi + \pi$, is equal to:

$$-ie^{i\phi} \begin{pmatrix} e^{i\phi} \cos \theta & -\sin \theta \\ e^{i\phi} \sin \theta & \cos \theta \end{pmatrix} \quad (4.8)$$

which is exactly $T_{m,n}(\theta, \phi)$ as defined above to within an additional phase.

Integrated photonics

The most common approach for building universal multiport interferometers is to use spatial modes that are manipulated using integrated photonic devices. This is the approach demonstrated by Carolan *et al*^[103], Ribeiro *et al*^[157], Perez *et al*^[158], and Shen *et al*^[104]. Although Carolan *et al* and Ribeiro *et al* implement the Reck design and Perez *et al*^[158] implement a hexagonal lattice, integrated photonics can straightforwardly be used to realise our proposed design. The realisation of our design using integrated photonics is discussed in more detail in the following chapter.

Time bins

Temporal modes can be manipulated in quantum optics using light emitted in regularly spaced time bins, which can then be delayed and interfered with other time bins. Temporal

modes are promising because pulsed light sources are readily available, and low loss optical delay lines can be built with either free space optics or optical fibre. Temporal modes have thus been used to demonstrate quantum walks^[56], boson sampling^[78], and multiplexing of quantum light sources^[96]. However, building the fast and low loss active optical devices that would be required to make wider use of temporal modes for quantum optics applications is a challenge.

A simple scheme for implementing universal multiport interferometers using the Reck scheme within a fibre loop architecture has already been proposed by Motes *et al*^[159], shown in Fig. 4.5a. Regularly spaced time bins are injected into the larger loop, and interference between consecutive pulses is engineered using the smaller loop.

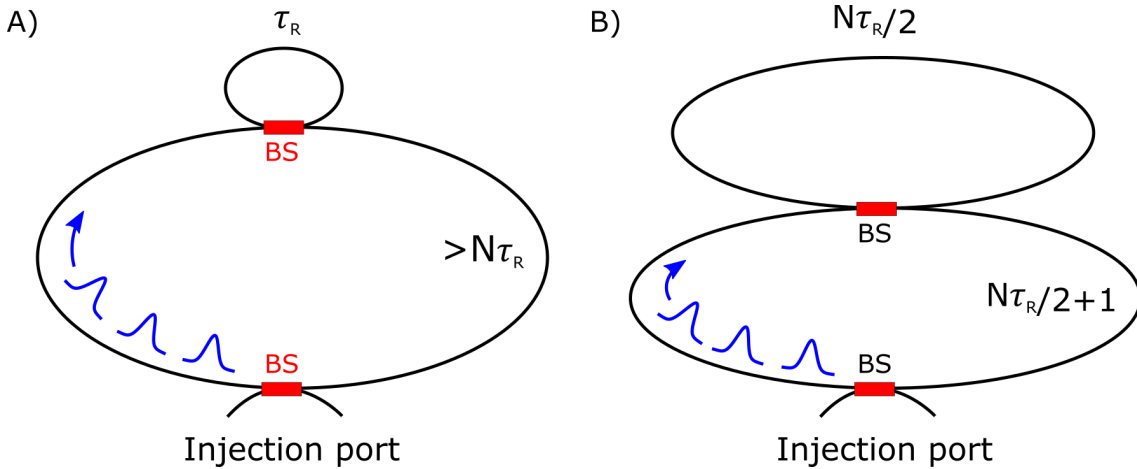


Figure 4.5: Time bin implementation of universal multiport interferometers using fibre loops, where each pulse is temporally separated by τ_R . a) Reck design. The top part of the fibre loop has a length equal to the pulse spacing, and the bottom part has a length equal to N times the pulse spacing. b) Our design. The top part of the fibre loop has a length equal to $N/2$ times the pulse spacing, and the bottom part has a length equal to $N/2 + 1$ times the pulse spacing. Note that the variable beam splitters also includes a variable phase shift.

Figure 4.5b shows how our design for the universal multiport interferometer shown in Fig.4.1 can be implemented within a compact “snowman” shaped fibre loop architecture for even N . The first $N/2$ pulses are injected into the loop and sent via the variable beam

splitter to the top part of the snowman, and the remaining half of the pulses are then allowed to interfere with the first half. To map these modes onto our decomposition shown in figure 4.2, at first we label the $N/2$ pulses in the top loop as the odd numbered modes, and the other pulses in the lower loop as the even numbered modes. Every time the pulses go around one loop, we switch the labels of the pulses in the top loop and in the bottom loop. There is one interstitial time bin that is used to switch which pairs of modes interfere with each other. An analogous design can be found for odd N .

4.1.5 Characterising a realistic universal multiport interferometer

Programming a universal multiport interferometer using our procedure requires a preliminary full characterisation of its beam splitters and phase shifters. This procedure, similar in spirit to that proposed by Mower *et al*^[169], only has to be done once, provided that there is no long-term drift of the optical properties of the interferometer.

At every step in the process, we choose an input-output pair that is such that there is only one possible path through the interferometer to get from one to the other. Any beam splitter along that path can then be characterised by sending light into the path and scanning the reflectivity of the targeted beam splitter while monitoring the output. Once all the beam splitters along one path have been characterised, they can be “removed” from the circuit by setting them to full transmission or full reflection and we can move on to a different path. This method allows us to characterise all the variable beam splitters within the interferometer.

Individual phase shifters can then be characterised by creating simple interfering paths through the interferometer, and modulating the phase shifters in those paths. We note that

the phase shifters at the input of the interferometer cannot be individually characterised in this way, but these are typically not relevant for most applications.

The preceding protocol assumes that the beam splitters can perfectly reflect and transmit light. This is typically not the case for real interferometers, where small amounts of light will leak through. However, the approach proposed by Mower *et al* to overcome this problem also works for our design. This light can be isolated and removed from the characterisation process by modulating the reflectivities of the beam splitters not along the path being broken, in such a way that the spurious light can be identified in the Fourier transform of the output signal.

4.2 Error tolerance of universal multiport interferometers

Realistic circuits will suffer from fabrication imperfections such as loss and imperfect beam splitters. Understanding such effects and finding methods to mitigate their impact are important for making use of realistic circuits. We first compare the loss tolerance of our design to that of the design by Reck *et al*, and show that our design is more loss tolerant. We then study the impact of beam splitter imperfections in our design, and propose methods to mitigate these imperfections.

4.2.1 Loss tolerance

To analyse the impact of loss on the performance of universal multiport interferometers, we first distinguish between two types of loss. Balanced loss in a multiport interferometer, in which every path through the interferometer experiences the same loss, preserves the target interference to within an overall scaling factor. This is generally acceptable for applications

in the classical domain, such as optical switching or microwave photonics. In the quantum domain, although loss severely affects the scalability of quantum experiments, post-selection can in some situations be used to recover the desired interference pattern. We note that propagation loss in an interferometer is expected to contribute to balanced loss, since every physical path length in an interferometer must be matched to within the coherence length of the input light to maintain high-fidelity interference. However, propagation loss must therefore be proportional to the longest path through the interferometer (i.e. the optical depth), so interferometers built according to our design will suffer from only about half the propagation loss of an interferometer built according to the Reck design.

Unbalanced loss, where different paths through the interferometer experience different loss, can be difficult to characterise and, critically, can result in a poor fidelity to the intended operation^[37,170–172]. Unequal losses between paths in the interferometer are typically caused by beam splitters, which are unavoidably lossy due to additional bending losses and scattering. To compare the tolerance of multiport interferometers to unbalanced loss caused by beam splitters, we adopt the following procedure. For a given N , we first generate 100 random unitary matrices^[173]. We then implement our decomposition, where we add loss to both outputs of all the resulting beam splitters by rescaling the $T_{m,n}$ matrices by a loss factor. We use a simple loss model that assumes equal insertion loss for every beam splitter. We then compare the fidelities in the overall transformations, using a metric that accounts for the non-unitarity of the loss. Specifically, we quantify the fidelity of the transformation implemented by a lossy $N \times N$ experimental interferometer, M_{exp} , to the intended

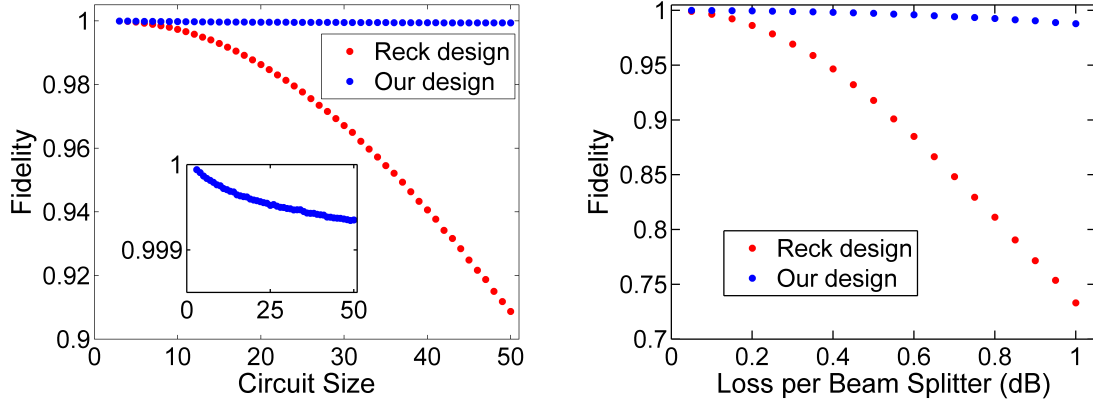


Figure 4.6: Left: Average fidelities achieved by an interferometer with a constant loss of 0.2 dB per beam splitter (as in the universal multiport interferometer in^[103]) for interferometers built according to the Reck design (red) and our design (blue), for different interferometer sizes. Inset: close-up of the fidelity in our design. Right: Fidelity as a function of loss per beam splitter, for interferometers implementing 20×20 transformations. We see from our results that our design is much more loss-tolerant than the Reck design, and maintains high fidelity with the target unitary matrix even in the case of high loss. This is because mismatched path lengths in the Reck design causes loss to severely affect the resulting interference.

transformation U using the following metric:

$$F(M_{exp}, U) = \frac{\text{tr}(|U^\dagger M_{exp}|)}{\sqrt{N \text{tr}(|M_{exp}^\dagger M_{exp}|)}} \quad (4.9)$$

This measure corresponds to the state fidelity at the output of the interferometer for a single photon input, averaged over all inputs and normalised so that we do not distinguish between matrices that differ by only a constant multiplicative factor. This metric allows us to focus on unbalanced loss instead of balanced loss in our simulations.

Figure 4.6 shows our simulation results, for both a fixed loss and varying interferometer sizes, and for a fixed interferometer size and varying loss. We conclude that interferometers that implement our design are significantly more tolerant to unbalanced loss than those implementing the Reck design. This is because, as can be seen in the circuit diagram in Fig.4.1, in the Reck design different paths through the interferometer go through different

numbers of beam splitters, so they all experience different loss and the resulting interference is degraded. In our design, the path lengths are better matched, so equally distributed loss within the interferometer does not strongly affect the resulting interference. We note that whereas unbalanced loss can be compensated for in the Reck design by adding loss to shorter paths, for example by adding dummy beam splitters to the shorter paths in the interferometer as proposed by Miller^[151], this is inefficient and it is better to start with a fundamentally loss-resistant interferometer.

4.2.2 Beam splitter imperfections

The following analysis of the impact of beam splitter imperfections on the performance of a universal multiport interferometer is based on the work by Burgwal *et al*^[174]. We focus our analysis on the problem of implementing Haar-random unitary matrices, since these are of particular interest to boson sampling.

Distribution of Beam Splitter reflectivities

To analyse the impact of beam splitter imperfections, we first study the distribution of beam splitter reflectivities within a universal multiport interferometer built according to our proposed design. We first draw a random 20×20 unitary matrix and perform our decomposition on it to determine what the beam splitter reflectivities in the interferometer should be. We repeat this process for 500 random unitary matrices, and calculate the average reflectivity for every beam splitter.

The spatial distribution of the average reflectivities in a size 20 interferometer is shown in Fig. 4.7a. Each beam splitter in this interferometer is represented as a grayscale square, the colour of which indicates its average reflectivity. We find that the reflectivities range

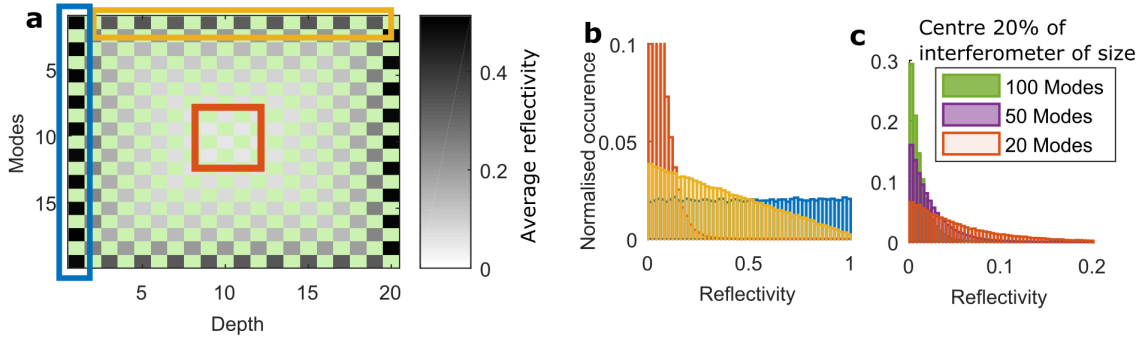


Figure 4.7: Distribution of the average reflectivities of the beam splitters in interferometers implementing Haar-random unitary matrices. a) Spatial distribution of these reflectivities in a size 20 interferometer. b) Histograms of reflectivities for three regions in the interferometer: the first column, the top row, and the centre. c) Histograms of reflectivities in the centre of the interferometer for different interferometer sizes.

from 0 to 0.5, and that the centre of the interferometer has relatively low reflectivities. In fact, the majority of beam splitters have low reflectivity and the overall average is 0.18. Note that low reflectivity means most light is transmitted, and thus travels along diagonal lines across the interferometer.

Figure 4.7b provides more insight into the distribution of reflectivities in different parts of the interferometer. We select three different regions of the interferometer, indicated in Fig. 4.7b: the first column, the top row, and the centre of the interferometer. The centre of the interferometer is delimited by a square the sides of which are 20% the size of the interferometer. For each of these regions, we show the histogram of the reflectivities that are observed during our simulations. We see that the centre region has particularly low values for the reflectivity.

To study the way in which this effect scales with the size of the interferometer, we plot in Figure 4.7c the histograms for the reflectivities in the centre of the interferometer for three different interferometer sizes: 20, 50, and 100. We see that increasing the size of the interferometer causes these reflectivities to become more and more skewed towards low

values. In contrast, we observe that the distribution of reflectivities does not change for the first row and for the top of the interferometer. The overall average reflectivity thus decreases as the interferometer size increases.

We can provide an intuitive explanation for these results. The average value of the squared amplitude of an entry in a Haar-random unitary matrix U of size N is $\langle |U_{i,j}|^2 \rangle = 1/N$. Therefore, for any given input in the interferometer we can expect an average proportion of $1/N$ of the light to exit at any given input. We now consider the first input and the last output. There is only one path through the interferometer that connects these two ports. The N interferometers along that path must therefore each transmit a fraction of about $\sqrt[N]{1/N}$ of the incident light, which tends towards 1 as N increases. The reflectivity therefore tends towards 0 for these beam splitters, which go straight through the centre of the interferometer. An analogous reasoning for other inputs close to the top and outputs close to the bottom (and vice versa) also explains why the other beam splitters close to the centre must have low reflectivity.

We note that an analytic expression for the distribution of beam splitter reflectivities in a universal multiport interferometer implementing our design was found by Russell *et al*^[175], and matches our numerical results. Russell *et al* also found that the Reck scheme similarly has a distribution of beam splitter reflectivities that is skewed to low values.

Impact on the fidelity

The requirement for low reflectivities in the centre of a universal multiport interferometer can be expected to limit the maximum fidelity that can be achieved. This is because one of the most convenient ways of implementing a variable beam splitter is to use a Mach-

Zehnder interferometer (MZI) consisting of two fixed 50:50 beam splitters and a variable phase shifter. The setting of the phase shifter determines the reflectivity of the MZI. If the fixed beam splitters that constitute the MZI deviate from 50:50, which is unavoidable in realistic devices, then the MZI is not fully tunable and cannot reach either high reflectivities or high transmittivities. As shown above, low reflectivities are needed for the majority of MZIs in a large interferometer implementing random unitary matrices, thus this is problematic.

We first adapt our decomposition procedure in order to quantify the effect of these imperfections. This adaptation is necessary since the $T_{m,n}$ matrices no longer always correspond to physical beam splitters because of their limited tuning range. First, we generate a random unitary matrix and decompose it assuming a perfect interferometer following the procedure described above. Next, we model the beam splitter error as follows. We draw the reflectivities of the static beam splitters composing the MZIs from a normal distribution with standard deviation σ and mean 0.5. We refer to σ as the fabrication error. Using these reflectivities, we calculate the minimum and maximum reflectivity of the corresponding MZI. If because of this limited range we cannot implement the required $T_{m,n}$ matrix we use the nearest achievable $T_{m,n}$ matrix instead, which will have a different reflectivity. We then calculate the overall resulting transformation using these modified $T_{m,n}$ matrices, and then evaluate the fidelity between the unitary matrix achieved by this process and the target unitary matrix.

The effect of beam splitter imperfections for various interferometer sizes up to size 50 and for both decomposition methods is shown in Fig. 4.8. Fig. 4.8a shows the fraction of random unitary matrices for which a $T_{m,n}$ matrix had to be replaced by another one for at least one beam splitter, as a function of beam splitter error. We see that every interferometer

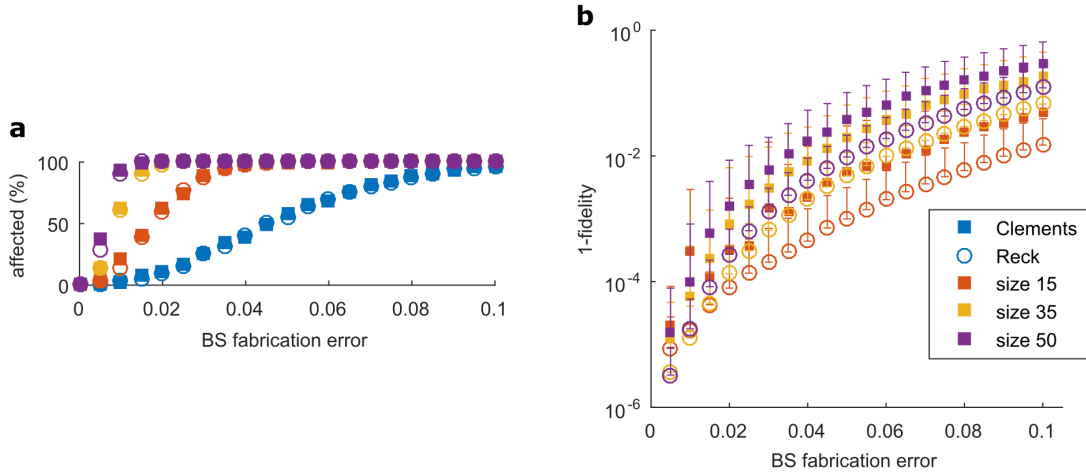


Figure 4.8: The effect of unbalanced MZIs on the fidelity of the decompositions as a function of the fabrication error, for both the Reck design and our design. a) the fraction of the random unitaries that are affected by imperfections. b) the fidelity between the target and the effective unitary for the affected matrices when using our adapted version of the decompositions. The error bars show the standard deviation of all data points used in the average.

is eventually affected by this error as it increases, and that as the size of the interferometer increases so does its probability of being affected. In Fig. 4.8b, we show the average fidelity for those interferometers that could not be faithfully implemented because of this error. The y -axis shows one minus the fidelity, which means that a value of 0 implies the effective unitary matrix is equal to the target. Figure 4.8 can be used as a reference to determine what fabrication tolerances are required to attain a specified fidelity.

We see that the Reck design is slightly less affected by this error than our design. Intuitively, this is because the total error accumulated along a path scales as the square root of the length of the path (since the errors are assumed to be uncorrelated). For a size N interferometer, the average between the error accumulated along the shortest (length 1) path and that accumulated along the longest (length $2N$) path in the Reck design is less than the error accumulated along a path of length N . The unbalanced path lengths in the Reck design therefore lead to slightly less total error than in our design in which each path

has roughly the same length.

We note that the adapted decomposition described above does not necessarily yield the beam splitter parameters that produce the overall transformation with the highest achievable fidelity for the system. Higher fidelities can be achieved by using the adapted decomposition as a starting point and then numerically optimising the beam splitter parameters. The result of this optimisation procedure, conducted using Matlab's built in `fminunc` function which uses a BroydenFletcherGoldfarbShanno algorithm^[176], is shown in Fig. 4.9. However, although this mitigates the effect of fabrication imperfections, we still cannot perfectly implement most unitary transformations.

Mitigation Methods

The settings for the reconfigurable beam splitters in our universal interferometer design are constrained by the one to one mapping between these beam splitters and the $T_{m,n}$ matrices used in the decomposition method. This constraint is what forces the beam splitters in the interferometer to be set to low reflectivities, which leads to decreased fidelities in the presence of fabrication imperfections. Using additional beam splitters to add some redundancy to the interferometer is one method of avoiding this constraint and achieving higher fidelities even with imperfect beam splitters.

We first explore the effect of adding an additional layer of beam splitters to the interferometer shown in Fig.4.1. We start with a random $N \times N$ unitary matrix, perform the adapted decomposition described above using the original square mesh of beam splitters, and then numerically optimise all the beam splitter parameters to maximise the fidelity. We use the built in sequential programming routine from Matlab to perform this optimisation.

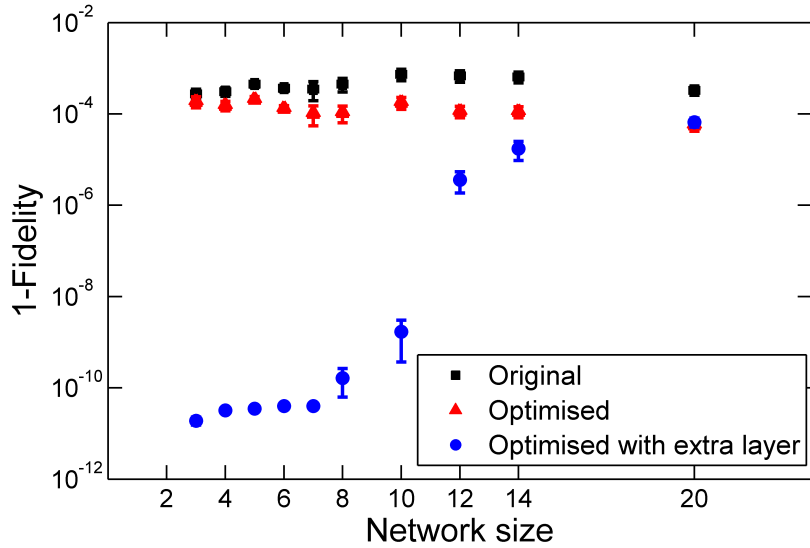


Figure 4.9: Increasing the fidelity with numerical optimisation and redundancy. The black points show the original infidelity after our adapted decomposition procedure, the red points show the infidelity after numerical optimisation of the network parameters, and the blue points show the infidelity after adding an extra layer to the network and performing numerical optimisation.

We sample 100 combinations of matrices and sets of imperfections in each point.

Figure 4.9 shows the enhancement in fidelity which is obtained by this procedure. We use the infidelity (defined as $1 - \text{fidelity}$) as our metric. We show in black the original infidelity obtained after our adjusted decomposition procedure, in red the infidelity obtained after performing numerical optimisation on the network parameters, and in blue the infidelity obtained after adding an extra layer to the network and then performing numerical optimisation. We see that an additional layer of beam splitters does increase the fidelity, especially for small network sizes. However, as the size of the decomposed matrices increases, the enhancement provided by the additional layer of beam splitters decreases. Furthermore, this method requires joint numerical optimisation of all the beam splitters and phase shifters in the interferometer to find parameters that increase the fidelity. Computationally, this optimisation is impractical since the parameter space scales exponentially with the number

of beam splitters. It is an interesting open problem to see how the number of additional layers of beam splitters that are required scales with the targeted increase in fidelity and the matrix size.

We note that by doubling the size of the circuit, an imperfect optical network can in principle achieve unit fidelity. This is because two imperfect MZIs can be concatenated to create one ideal reconfigurable beam splitter^[151,177,178]. The resulting reconfigurable beam splitter can then be fully tunable as long as its constituent four fixed beam splitters have a splitting ratio of no more than 85:15, thus significantly relaxing their fabrication tolerances. An ideal interferometer can then be built using these ideal beam splitters. However, this method comes at the cost of doubling the optical depth and therefore the loss in the interferometer.

4.3 Conclusion

Universal multiport interferometers are important tools for the field of linear optics. In this chapter, we proposed a new design for these devices using a mesh of beam splitters and phase shifters that is more compact than previously known designs. We also demonstrated that our design outperforms previously known designs in terms of loss and error tolerance. In the next chapter, we experimentally demonstrate a modular architecture for reconfigurable multiport interferometers that allows us to implement our new interferometer design.

Chapter 5

Modular Linear Optical Circuits¹

Integrated photonics is a suitable platform for building the reconfigurable multiport interferometers discussed in the previous chapter. Photonic chips are more compact, more stable, and easier to scale up to large sizes than alternative platforms such as bulk optics. Integrated circuits that can perform arbitrary interference between a fixed number of modes have been demonstrated and used for several quantum information protocols^[37,59,103]. Reconfigurable devices that can provide programmable frequency filtering as well as interferometry have also been shown^[158].

However, all the devices demonstrated to date are monolithic and are designed for a fixed number of optical modes. A chip designed to manipulate a large number of modes and complex interference may not be the most appropriate for also handling a smaller number of modes or simpler interference. Indeed, as device size increases to handle more modes, so do optical loss, optical crosstalk, and the complexity of characterizing all the optical elements on a chip. In addition, fabrication tolerances become more stringent, since a single faulty component may jeopardize the correct operation of the entire device.

¹The contents of this chapter relate to the author's publication entitled "Modular Linear Optical Circuits"

In this chapter, we propose and demonstrate the use of identical, simple building blocks to compose reconfigurable interferometric circuits of any size that are suitable for linear quantum optics. Each of these blocks consists of a single row of Mach-Zehnder interferometers with phase shifters both internally and on the input arms, as shown in Fig. 5.1a. Fig. 5.1d illustrates how subsequent modules may be offset to construct the required network. Each of these modules may be tested and characterized individually, and imperfections in the modules can be mitigated by selecting those most suitable for a given experiment. Individual chips can be added or removed, depending on the desired application.

This chapter is structured as follows. We first explain and motivate the modular design that we choose for our devices. We then describe the characterisation procedure for a single unit. Finally, we show how we use these units to build a large interferometer, and present our experimental results demonstrating that this interferometer is programmable and can be used to implement a wide range of optical transformations.

5.1 Modular architecture

The basic building block of our device is a silica-on-silicon chip with 24 UV-written waveguides designed for 830 nm light (Fig. 5.1). The 20 waveguides at the centre of the device form 10 independent Mach-Zehnder interferometers, consisting of two X-couplers. For each Mach-Zehnder, four resistive heaters are placed just above the waveguides to modulate the phases via the thermo-optic effect. These heaters are wire bonded to a printed circuit board (PCB) so that they can be connected to control electronics. Several of these building blocks can be coupled to each other using optical epoxy to build larger interferometers.

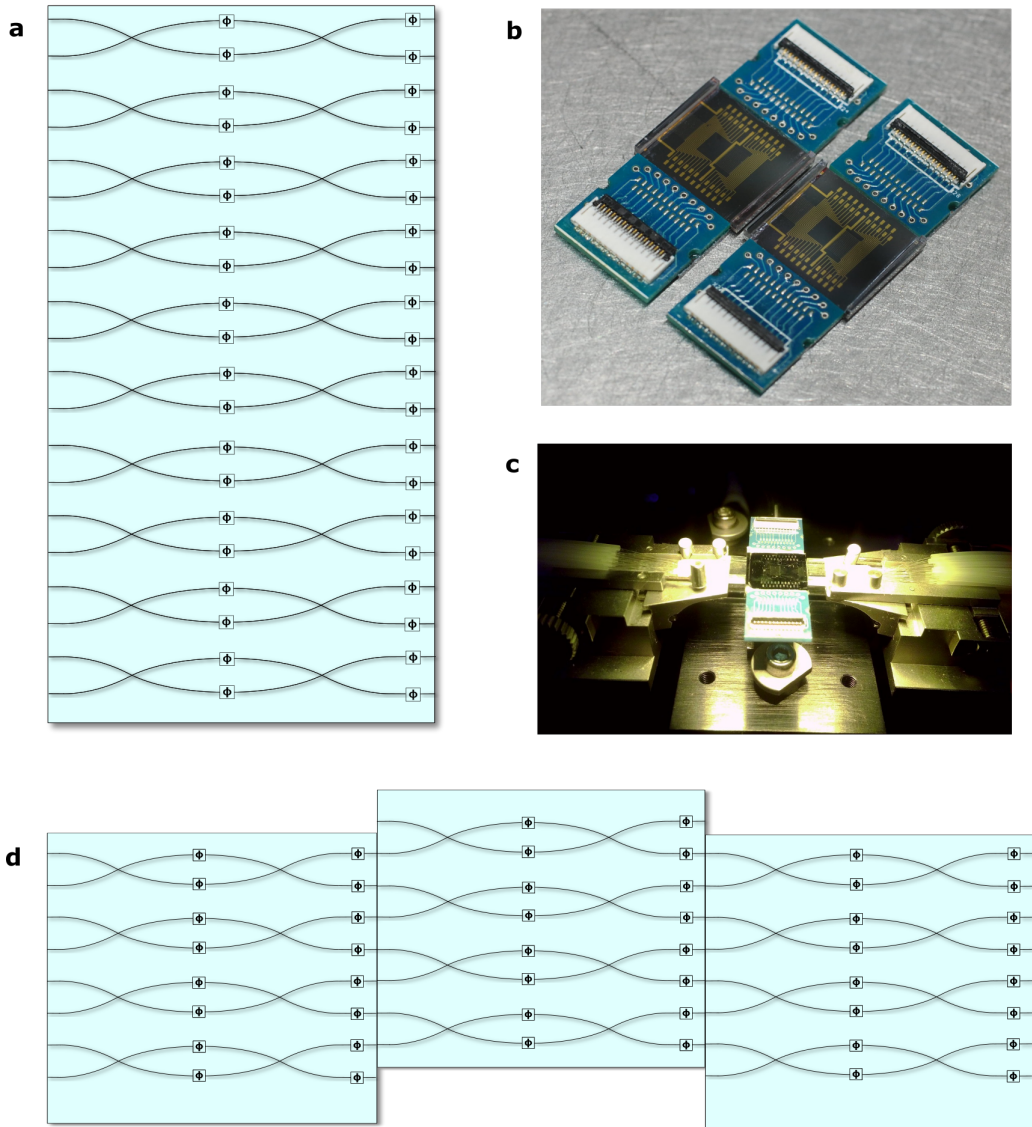


Figure 5.1: Modular photonic chips. A) Layout of the waveguides on the chip. 10 Mach-Zehnder interferometers (MZI) consisting of two X-couplers are laid out side by side, with 4 thermo-optic phase shifters per MZI. B) Picture of two completed modular chips. The optical chip is in the centre and is surrounded by two green printed circuit boards (PCB). The wiring for the phase shifters appears in gold on the chip. C) Coupling to a modular chip. A modular chip is butt coupled to a 24 fibre V-groove array using two coupling stages, one on each side. D) Several modular chips can be connected to each other to form large interferometric circuits.

5.1.1 Why a modular design?

These chips are intended to be tiled to build large interferometers, as shown in Fig. 5.1. In particular, using the design for universal multiport interferometers discussed in the previous chapter, N of these chips can be used to implement a $N \times N$ universal interferometer. We find that it is more advantageous to use a modular approach than to attempt to build a single monolithic large interferometer for the following reasons.

Firstly, a modular approach gives us more flexibility. Many experimental protocols in linear optics, such as quantum teleportation^[37], do not require fully connected interferometers. For these applications, additional MZIs are not necessary and only introduce more loss. Furthermore, as was discussed in the previous chapter, additional MZIs at the output of a universal multiport interferometer can be used to increase the achievable fidelities. A modular approach allows us to add these MZIs if required, or alternatively to implement the nested MZI architecture that can be used to form an ideal two by two interferometer from two MZIs.

Secondly, it is easier in practice to work with individual layers of MZIs than it is to work with a large interferometer. Optical characterisation is easier when the modes don't all interfere with each other. Optimising the fabrication of a single layer of MZIs is also easier than optimising that of an entire interferometer. Furthermore, faulty components can be replaced without compromising the entire structure.

The downsides of using a modular approach are that additional coupling steps are required and loss can occur at the interfaces. However, with a bit of experience, coupling chips to each other is not a particularly difficult task, and since the waveguides are all fabricated using the same process different chips can be expected to be perfectly mode matched. Fur-

thermore, commercial epoxy exists that matches the refractive index of the waveguides and maintains high coupling efficiencies during and after the curing process.

5.1.2 Motivation for the structure

Following our discussion of different material platforms in the introduction, we find that UV written silica waveguides best suit our purpose. We intend our devices to only provide multimode interference while being fibre coupled to external photon sources and detectors which are readily available in our lab. We are also concerned with loss, which significantly affects quantum optics experiments in terms of decreased photon counting rates; silica provides the lowest coupling loss to optical fibre. Furthermore, due to the unavailability of high efficiency photon sources we plan to perform experiments with fewer than 20 modes, so the low density of silica photonic devices is not a significant constraint. We also want our devices to be reconfigurable. Thermo-optic phase shifters are a mature technology, but they require the use of a substrate that can act as a heat sink. UV written waveguides can be built in silica on a silicon substrate. Furthermore, UV writing does not require a lithographic step, which allows for quick turnaround times from planning to production.

We work at 830 nm light for the simple reason that a good single photon source was available at that wavelength in our lab^[94]. Furthermore, despite the desirability of the telecom band in terms of lower losses and the availability of standard telecoms equipment, high efficiency detectors for the telecom band were not widely available when this project began. We had several SPADs optimised for 830 nm that could be used instead.

X couplers^[179] are beam splitters that consist of two waveguides that directly cross each other at an angle that defines the coupling ratio. We use X couplers instead of the

more commonly used directional couplers because the splitting ratio in X couplers does not strongly depend on wavelength, and so can be used with broadband photons. X couplers are also more compact. Furthermore, since low-loss X couplers require an increased refractive index in the crossing region compared to the waveguides, they are particularly well suited for UV written waveguides since the refractive index can be easily tuned by changing the fluence of the writing laser. Such tuning cannot be achieved with etched waveguides, for example. Furthermore, UV written X couplers can in principle achieve very low loss below 0.1 dB^[180].

Finally, our design for universal multiport interferometers requires the presence of two phase shifters: one inside the MZI and one outside it. Our phase shifters consist of strips of chromium resistors deposited above the waveguides that we can use to modulate their refractive index via the thermo-optic effect. We choose resistive heaters because this is a mature technology for silica-on-silicon devices. The silicon substrate acts as a heat sink. Although these phase shifters are reconfigurable at a slow rate of about 1 kHz, this is acceptable for experiments that do not require feed-forward. Furthermore, we choose to use four phase shifters per MZI for our devices because this allows us to use them in a push-pull configuration. The total heat load across the chip can therefore be kept constant, which is important because thermal fluctuations can cause undesirable phase shifts.

5.1.3 Structure and fabrication

The chips are fabricated at the University of Southampton^[137]. Using flame hydrolysis deposition, three doped silica layers are fabricated on a silicon substrate on a 6" wafer (see Fig. 5.2). A 4.5 μm germanium-doped layer is sandwiched between two 18 μm boron-doped

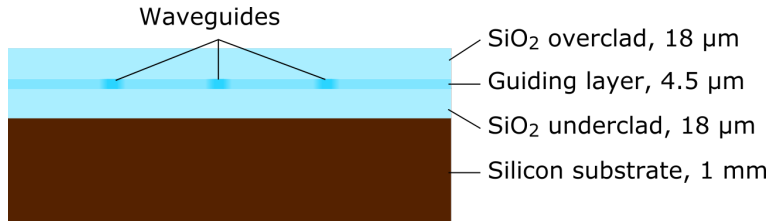


Figure 5.2: The layer structure of the modular chips. Three doped silica layers are grown on top of a silicon substrate. Waveguides are formed in the middle layer by focusing a UV laser into it.

layers. The doping in these layers is designed so that all three layers have similar refractive indices. A continuous-wave UV laser at 244 nm is then focused into the germanium-doped layer, which causes a permanent refractive index increase that is typically of order 10^{-3} . Translating the chip through the focal point of the laser therefore creates optical waveguides.

The electrical components are then deposited on the chip. The phase shifters are composed of thin strips of NiCr ($0.4 \mu\text{m} \times 50 \mu\text{m} \times 2.5 \text{ mm}$). These are connected to wire bonding pads at two edges of the chip using gold wires. These electrical components, except for the wire bonding pads, are covered by a thin protective silica layer.

Once the deposition step is finished, the chip is attached to a strengthening bar, polished, placed on a thermally conductive silicon layer, and two printed circuit boards with matching wire bonding pads are placed on both sides. The last step consists of wire bonding the chip to the two PCBs.

5.1.4 Electronics

Our collaborators at the University of Southampton also developed the electronics control system. These must control a large number of electrical channels: each chip contains 40 phase shifters, and we intend to use several chips simultaneously.

The phase shifters are controlled using a pulse width modulation (PWM) scheme, which

allows us to maintain a constant heat load across the chips and reduce crosstalk. The electronics are designed to apply a constant voltage across a switch leading up to each pair. Within every $32 \mu\text{s}$ time period, we define 256 time bins. The switch applies the voltage for a given number of bins to one phase shifter, and then applies it to the other phase shifter for the remainder of the time bins. This number of bins will be referred to as the PWM setting in the following, and ranges from 0 to 255. This process is repeated every $32 \mu\text{s}$. Since $32 \mu\text{s}$ is much shorter than the thermal response time of the waveguides, the resulting refractive index change in the waveguide is constant and is determined by the PWM setting. Using this pulse width modulation scheme, the relative phase shift between the two waveguides is conveniently a linear function of the PWM setting.

The central part of the control system is a Field-Programmable Gate Array (FPGA) control board. This control board is connected on one side to the chips via ribbon cables, and on the other side to a computer via a USB connection and can be controlled via a Matlab interface. The control board contains 4 banks of ten switches each, which each control a pair of phase shifters. Each switch receives both a control signal from the FPGA and a constant 21.5 V delivered to the control board by an external voltage source. The control signal is used to switch this constant voltage to the phase shifters using the PWM scheme described above. A single control board can control 40 pairs of phase shifters, which corresponds to two chips. Several control boards were therefore produced and they can be interfaced to control a larger number of chips.

5.2 Characterisation

After fabrication at the University of Southampton, these chips were delivered to us for characterisation and to perform experiments.

5.2.1 Optical characterisation

Important optical properties to be measured are: loss, reflectivity of the beam splitters in the MZIs, and degree of polarisation. To measure these properties, we first couple the chips to a 24 fibre polarisation-maintaining V-groove array on both sides using two six axis coupling stages. With a bit of experience, this coupling process can be performed in roughly an hour. Given the large number of optical inputs and outputs, we use two 1 by 16 polarisation maintaining optical switches to automate parts of the characterisation process. 8 optical inputs on the chip are therefore not used during the characterisation process, but this is acceptable for initial testing.

Loss: We measure the loss in two steps. We first measure the fibre-to-fibre loss by comparing the input power to the output power. The resulting value, however, does not give us any indication as to how much of the loss originates from the fibre to chip coupling and how much comes from propagation loss.

To measure the propagation loss directly, we use a method demonstrated by Rogers *et al.*[¹⁸¹]. The four straight test waveguides on the sides of the chip contain weakly reflecting Bragg gratings written at different locations along the waveguides and at different wavelengths. By sending light into both extremities of the waveguides, monitoring the back-reflection spectra, and comparing the relative intensities of the reflection peaks (Fig. 5.3b), the linear propagation loss in the waveguide can be determined. Specifically, the power

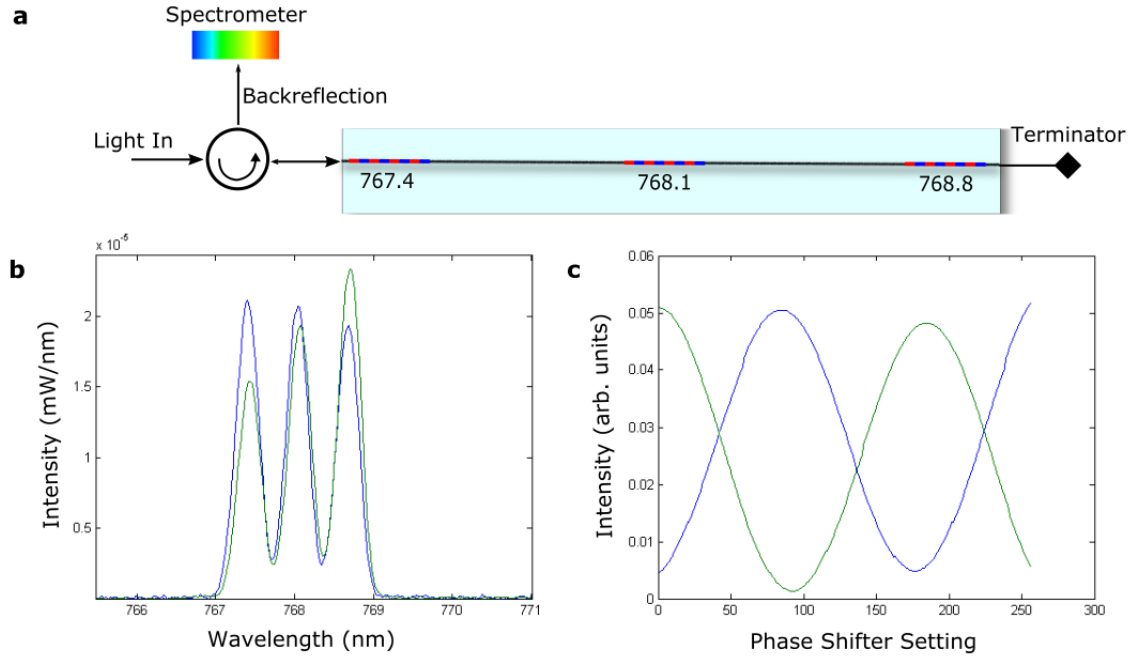


Figure 5.3: Characterisation of the modular chips. A) Method for measuring the propagation loss. Comparing the spectrum (shown in B) of the backreflection from three weakly reflecting Bragg gratings to the spectrum of the backreflection from the other side allows the propagation loss to be determined. C) Sending light into one input of an MZI and monitoring both outputs allows us to test the phase shifters. This graph shows the intensities at the outputs as a function of the pulse width modulation setting.

reflected by a Bragg reflector labelled i from the right and from the left is:

$$R_{left}^{(i)} = P_{left} r_i e^{-2\alpha x_i}, \quad R_{right}^{(i)} = P_{right} r_i e^{-2\alpha(L-x_i)} \quad (5.1)$$

where P represents the input power in the waveguide taking into account the optical losses, r_i is the reflectivity of the Bragg reflector, α is the linear propagation loss that we aim to determine, x_i is the spatial position of the reflector, and L is the total length of the chip. This equation leads to:

$$\ln \frac{R_{left}^{(i)}}{R_{right}^{(i)}} = \ln \eta - 4\alpha x_i \quad (5.2)$$

where $\eta = \frac{P_{left}}{P_{right}} e^{-2\alpha L}$. With several Bragg gratings in known locations, the left-hand side of equation 5.2 can be plotted versus x to find α . Furthermore, when several chips are glued together, this method also allows us to determine the chip to chip coupling loss.

We measure about 2 dB total fibre-to-fibre loss through the straight waveguides, with an average propagation loss of about 0.3 dB/cm. This implies that the fibre to the chip coupling loss is about 0.8 dB. Chip to chip coupling was found to introduce about 0.2 dB loss per interface. We also measure a total fibre-to-fibre loss of 6 dB through the Mach-Zehnder interferometers, when adding the sum of the two output optical powers. This is much higher than for the straight waveguides and implies that the Mach-Zehnders introduce an excess loss of 4 dB. We believe that this excess loss is due to changes of the index profile in the coupler due to thermal effects in the fabrication of the thermo-optic phase-shifters. The behaviour of these couplers is very sensitive to small refractive index changes, and their design had been optimised neglecting this thermal effect.

Beam splitter ratios: The splitting ratios of the beam splitters can be determined in a similar way. Each Mach-Zehnder interferometer has six Bragg gratings. Four of them are located at the four inputs and outputs, and two are in the centre of the interferometers. Measuring the backreflection spectra at all four input and output ports yields information about the reflectivities of the beam splitters.

We aim for reflectivities of 50% since this is the value that yields the widest range of possible transformations implemented by Mach-Zehnder interferometers, as discussed in the previous chapter. We measure reflectivities ranging from 0.5 to 0.64, with an average of about 0.58. However, these measurements are somewhat noisy so not very reliable. Due to the large excess loss in the MZIs, the back-reflection spectra from the Bragg gratings

are quite weak and of the same order of magnitude as other processes that scatter light backwards towards our detector.

Polarisation: We can measure how well the chips preserve polarisation by sending polarised light in and measuring the degree of polarisation at the output using a polarising beam splitter. We found that light sent into an input fibre with a degree of polarisation of 1:100 exits the output fibre with a degree of polarisation of 1:30. Moreover, we found that the loss and the splitting ratios are independent of the polarisation of the input light. For the experiments described in the following, we therefore arbitrarily choose to use transverse-magnetic (TM) polarisation.

5.2.2 Electrical characterisation

The phase shifters must also be characterised. To do so, we send light into one input, and scan the PWM settings as we monitor the power at both outputs (see Fig. 5.3c). Several properties of the chips can be obtained in this way.

First, we obtain the magnitude of the phase shift that we achieve. As shown in the previous chapter, we expect a sinusoidal response of the intensities at the output as a function of PWM setting. We experimentally confirm this sinusoidal response (see Fig. 5.3c). Furthermore, except for some phase shifters that seem damaged and are unresponsive, a phase modulation of more than 2π is consistently achieved.

Second, we obtain the thermal crosstalk from one MZI to its neighbours. We expect some amount of crosstalk due to the heat generated by the phase shifters spreading to nearby waveguides. To measure crosstalk, a MZI was placed close to its 50:50 point and its outputs measured as settings of adjacent heaters were varied. This was carried out both in

the case of complementary heating and with one heater in each pair disabled. We find that when achieving a π phase shift on the target MZI, our dual heaters induce a crosstalk of about 0.01π to the neighbouring MZI and of 0.007π to the next nearest MZI, whereas using a single phase shifter to achieve the same phase shift induces about twice as much crosstalk. This improvement justifies the use of our dual heater design.

Third, we measure the stability and repeatability of the phase shifters. The phase stability of these devices over time was determined by configuring a MZI close to its 50:50 point, sending light in one input and monitoring the intensity at the two outputs over time. Over 30 minutes, we find a standard deviation of the splitting ratio of 0.17%. We measure the repeatability of the PWM settings by periodically changing the PWM setting back and forth from one setting to another and verifying the splitting ratio after each change. We find that the repeatability of the splitting ratio for a given PWM setting is 0.6%.

However, we also find intriguing behaviour that is consistent with multimode behaviour in the X couplers^[182]. Firstly, the depth of the modulation is lower than is expected given the estimated beam splitter reflectivities. Secondly, the PWM setting corresponding to the minimum of the modulation of one output does not quite correspond to PWM setting for the maximum of the other output. With additional modes in the couplers, there is no longer a constraint for the maxima and minima of the MZI outputs measured using single mode fibre to line up or for them to reach particularly low modulation depths. These additional modes are not transmitted by the waveguides themselves and so are not observed at the output of the chip and contribute to the loss in the system. We believe single mode behaviour can be recovered once the thermal effects during fabrication of the heaters mentioned earlier are accounted for.

5.2.3 Experiment Planning

Our characterisation results inform our choice of experiments to be performed with these devices. We find that the loss through these chips, and in particular the excess loss at the MZIs, makes the use of these chips impractical for multiphoton experiments. This is because linear optics experiments typically require every photon to make it through the circuit and be detected. Even with postselection on successful trials, very high losses cause the rate of successful trials to drop sharply. For example, consider a three photon experiment performed using a device consisting of three modular chips. With the photon sources available in our lab, the detection rate of three heralded photons is about 100 Hz. Three modular chips with 60% excess MZI loss, 15% fibre to chip loss, 5% loss per chip to chip interface and a total of 19% propagation loss (corresponding to 0.3 dB/cm loss over three 1 cm long chips), the total transmission we expect to have is 3%. The probability that all three photons make it through is therefore $0.03^3 \approx 3 \times 10^{-5}$, so that three photon rates at the output would be about 0.003 Hz, or about ten events per hour. Collecting useful statistics for different settings of the modular chips can therefore be expected to take about a month, which is very impractical. We therefore decide to fabricate a new generation of chips designed for 1550 nm. Moving to 1550 nm allows us to use state of the art superconducting detectors, and since the modes are larger they are less sensitive to fabrication imperfections such as waveguide roughness. We intend to perform quantum optics experiments with those new chips instead of our current chips.

Although we decide not to perform quantum optics experiments with our 830 nm devices due to high loss, these losses do not preclude a classical demonstration of their capabilities. In particular, we can demonstrate their use as universal multiport interferometers using

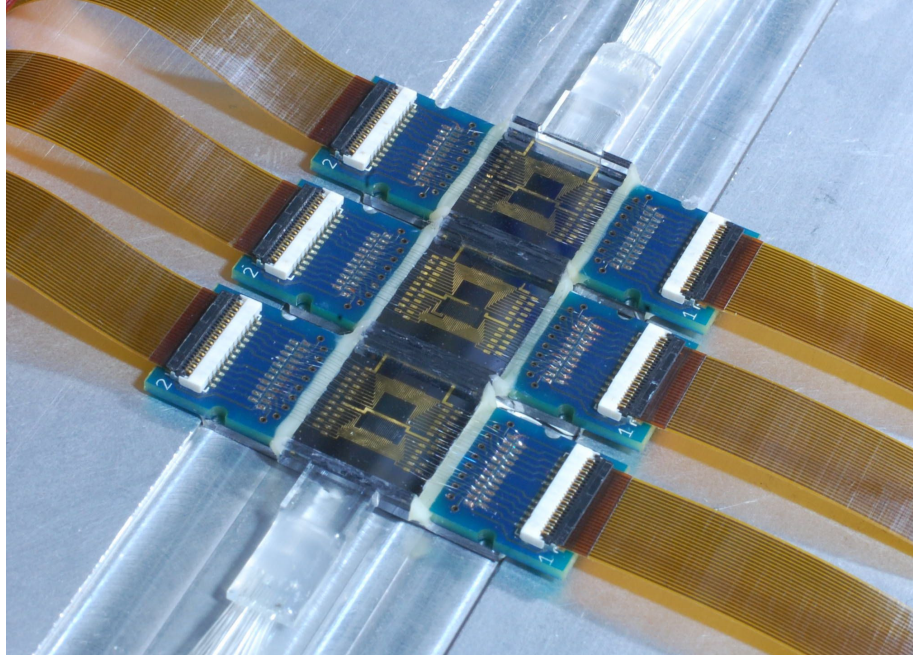


Figure 5.4: Picture of 3 assembled modular chips.

classical laser light.

5.3 Characterising a three chip assembly

To perform a demonstration of these devices, we start by assembling three of the modular chips (see Fig. 5.4). Three chips is the minimal number that we can use to demonstrate a non trivial 3×3 universal multiport interferometer. Furthermore, three chips is the number that is required to build a circuit that can perform quantum teleportation^[37], which is an important building block of linear optical quantum information schemes. We aim to show that our assembly can implement a wide range of useful optical transformations.

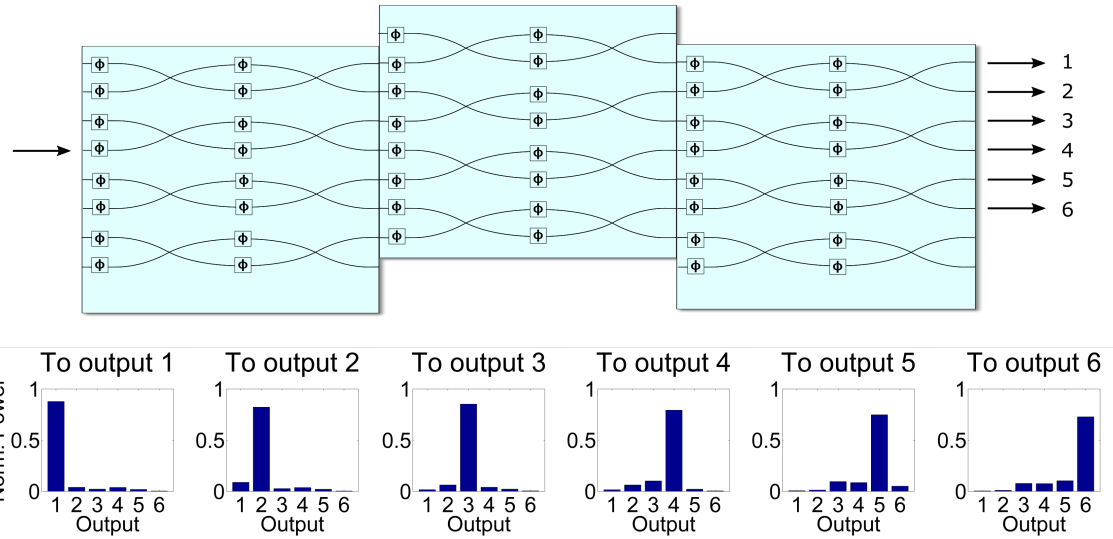


Figure 5.5: Using our three chip assembly as a switch. Top: layout of the waveguides on the chip. Any one input can reach six outputs. Bottom: experimental results. Each bar chart shows the distribution of power among the outputs after maximising the amount of light at one target output. The six charts correspond to the six target outputs, and are normalised so that the sum of powers is 1.

5.3.1 Switching between optical outputs

As a first demonstration of our three chip assembly, we show that light from one input can be switched to any of its six available outputs. The procedure for doing so is straightforward. We send light into the input, monitor the output that we seek to switch the light into, and sequentially optimise the MZIs on each chip along the path to that output to maximise the measured power. The two central outputs can be reached by two possible paths; we arbitrarily choose one of these paths.

Our results are shown in Fig. 5.5. We see that our chip assembly successfully routes most of the light to the desired output, for all six outputs. However, some leakage does occur (with crosstalk values of about -10 dB in the worst channels), which originates from the imperfect splitting ratios of the couplers and their multimode behaviour.

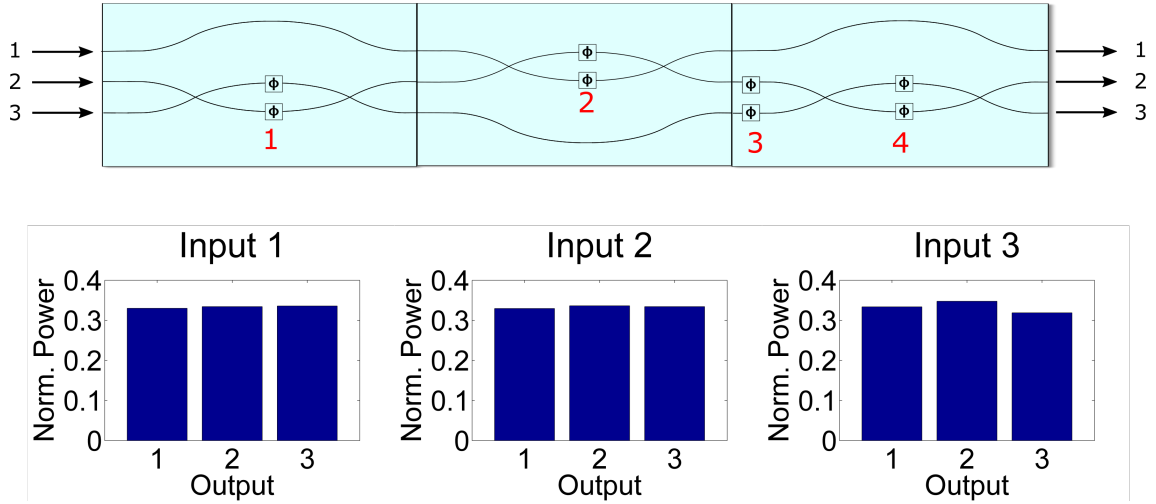


Figure 5.6: Using our three chip assembly as a balanced 3×3 interferometer (a tritter). Top: layout of the waveguides on the chip. Any three neighbouring modes can in principle be used to implement a tritter. Bottom: experimental results. Each bar chart shows the distribution of power among the three outputs after implementing a tritter. The three charts correspond to the three input ports, and are normalised so that the sum of powers is 1.

5.3.2 Implementing a tritter

Next, we show that our chip assembly can implement a balanced 3×3 interferometer, also known as a tritter. Tritters can be used for fundamental studies of quantum interference^[39], as well as for classical photonics applications.

We use a self-configuring approach to implement a tritter^[151]. First, since we only want the three modes under study to interfere with each other, we start by isolating them from the other modes by setting superfluous MZIs to act as identity. These fully reflective MZIs are represented as curving waveguides along the edges of the circuit in Fig. 5.6. Once this is done, we sequentially configure the relevant phase shifters to implement the tritter. Since MZI 2 uniquely determines the coupling from mode 1 to mode 1, we send light into 1, monitor output 1, and set MZI 2 so that one third of the maximum output power is measured at output 1. Once MZI 2 is set, we proceed to MZI 4 which now uniquely determines the

coupling from input 1 to outputs 2 and 3. Once MZI 4 is set, we proceed to MZI 1 which uniquely determines the coupling from 2 to 1. We then set phase shifter 3 so that one third of the light from 2 goes to 2. Now, inputs 1 and 2 are correctly split between the three output modes. Since the interferometer should be implementing a unitary transformation, the third mode should be orthogonal to the other two which in the case of a tritter should also result in equal splitting. We note that this self-configuring approach does not require detailed prior characterisation of the phase shifters, but does need a light source and a detector to be connected during the procedure.

Our results are shown in Fig. 5.6c. The l_1 distances between the three output distributions and those expected from a tritter with ideal splitting are 0.007, 0.008, and 0.03. The light is therefore roughly equally split between all output ports. In particular, inputs 1 and 2 are more equally split than input 3, which results from the fact that 1 and 2 were the inputs used for the self-configuring procedure. Since the correct splitting for input 3 is determined only by the unitarity constraint on the interferometer, our results show that the interferometer deviates from unitary behaviour. Such a deviation is expected from only looking at a subset of three outputs of a device with imperfect couplers.

5.3.3 Implementing a universal multiport interferometer

We also demonstrate that our chip assembly can be used to implement a 3×3 universal multiport interferometer using the method described in the previous chapter. The relevant optical elements to implement universal multiport interferometers are the three MZIs labelled 1, 2 and 4 and the phase shifter labelled 3 shown in figure 5.7b. We note that for the 3×3 case, there is no difference between our design and the Reck design. We use the

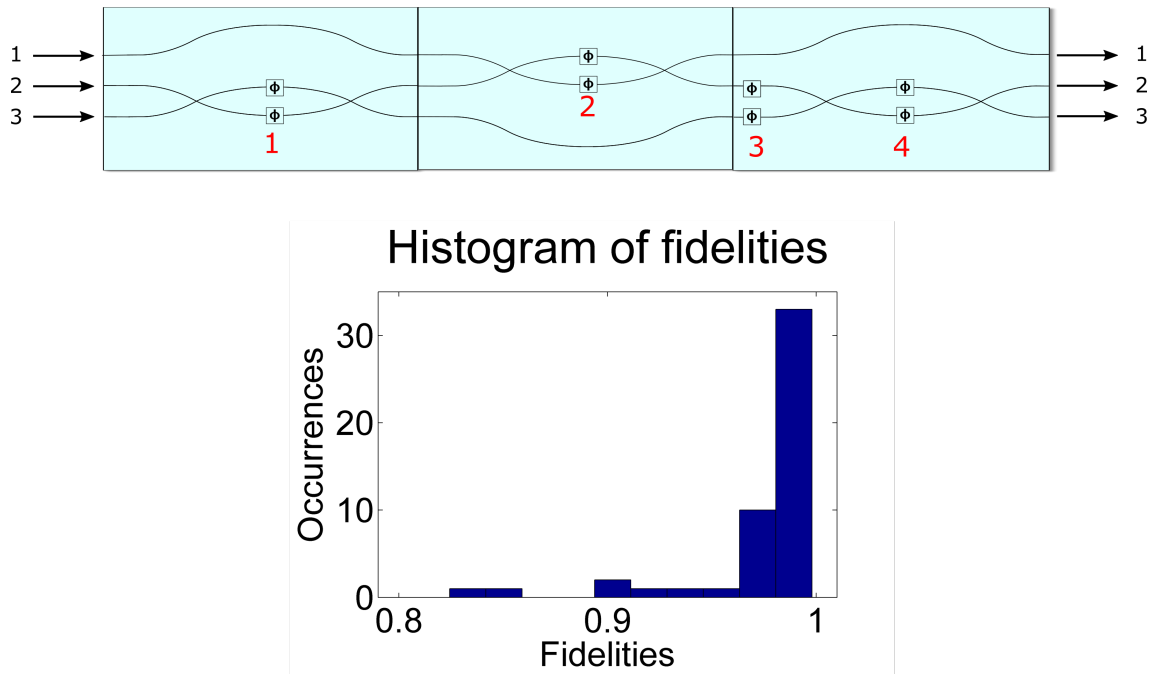


Figure 5.7: Top: Diagram of the circuit used to implement a 3×3 universal multiport interferometer. Bottom: Histogram of the fidelities that were achieved for the 50 random unitary matrices implemented using our universal multiport interferometer. An average fidelity of 97.5% was achieved.

same three modes as were used for the tritter, and in the same way we start by isolating the three modes under study by setting any superfluous MZIs to fully reflect.

Characterising the optical elements

We start by characterising the 2×2 transformations implemented by the three MZIs. We start by modelling the behaviour of the optical elements in a way that is compatible with the decomposition procedure described in the previous chapter. For each PWM setting x , we describe the transformation implemented by MZI number j by a 2×2 scattering matrix $T_j(x)$, which is assumed to be of the following form to within a constant loss factor that is

independent of the PWM setting:

$$T_j(x) = \begin{pmatrix} \cos(\theta_j(x)) & i \sin(\theta_j(x)) \\ i \sin(\theta_j(x)) & e^{i\phi_j(x)} \cos(\theta_j(x)) \end{pmatrix} \quad (5.3)$$

where $\theta_j(x)$ and $\phi_j(x)$ are parameters describing the transformation. $\phi_j(x)$ represents an additional phase offset between the two outputs that may appear at the output of the MZIs.

An important aspect of this model is that it assumes unitary behaviour of the couplers (to within constant lost at both outputs), which we know is not accurate. Nevertheless, we demonstrate in the following that this model is sufficient for us to implement a wide range of arbitrary 3×3 transformations with high fidelity. We first aim to estimate $\theta_j(x)$ and $\phi_j(x)$ for every x and j .

We note that whereas all other optical and electrical properties of the chips are measured before assembly, we find it convenient to measure θ and ϕ after assembly for our three chips. The reason for this is that since ϕ corresponds to the external phase shift, using a three chip assembly to include this phase inside an interfering loop allows for convenient characterisation of ϕ . Furthermore, ϕ contains a constant factor dependent on the chip to chip distance after assembly which needs to be determined anyway. We note that the modular approach allows for progressive characterisation of the device during assembly, so that the values of θ and ϕ thus determined will still be of use if more chips are added to the assembly.

We start by estimating $\theta_j(x)$, which is determined by the relative splitting ratio of the inputs to the outputs. This requires two sets of data for every MZI. To collect the first set of data for MZI 1 we send light into input 2 while monitoring output 1 and scanning over

the PWM settings for MZI 1. We obtain the second set of data by repeating this procedure for the $3 \rightarrow 1$ path. For MZI 4, we send light into 1 and monitor first 2 and then 3 while scanning across its PWM settings.

Further processing is required to obtain $\theta_j(x)$ from these sets of data. Both background light and unbalanced loss at the outputs have to be accounted for. We treat as background light both light that is lost early in the system before re-coupling into a waveguide and light that does not interfere as expected at a coupler due to coupler multimodeness (leading to the lower visibilities than expected described earlier). To account for this background light, we use the measurements of the splitting ratios of the beam splitters for the individual chips to estimate the modulation depth that we should get from every MZI, compare this to the measured modulation depth, and subtract the difference. To account for the unbalanced loss, we have assumed in relation 5.3 that the MZI loss does not depend on the PWM setting. The sum of the two powers should therefore be constant, and the unbalanced loss can in principle be compensated for by multiplying one of the two sets of data per MZI by a constant loss parameter such that the fluctuation in the sum of the powers is minimised. We use numerical optimisation to find this loss parameter for each MZI, and then also normalise the sum of the powers to 1 for every x so that the transformation can be described by relation 5.3.

Obtaining these two sets of data for MZI 2 is less straightforward. A first set of measurements can be performed by sending light into input 1 and monitoring output 3 while scanning across the PWM settings of MZI 2. However, to get a complementary second set of data for MZI 2 would require measuring an input-output relation through the chip assembly in which interference between two paths occurs. This interference is detrimental

to the measurement of the splitting ratio. Isolating the contribution of the path under study is possible, for example using the method proposed by Harris *et al.* which involves modulating the phase inside the interfering path at a specific frequency so that the portion of the output signal caused by the interference can be filtered out. However, this method is impractical using our control electronics. Instead, we make a further assumption on the behaviour of MZI 2; we assume that the maximum of the modulation curve given by the $1 \rightarrow 3$ measurement is the maximum of the sum of the powers at the output. Given that we have already assumed that MZI 2 is described by relation 5.3, the complementary optical power for a given PWM setting x is therefore the difference between this maximum optical power and the measured power along the $1 \rightarrow 3$ path for that x .

Next, we measure $\phi_j(x)$ for MZIs 1 and 2, which plays a role in determining the interference in the closed loop between 1 and 2. This phase can be adjusted using phase shifter 4; however, both MZIs 1 and 2 induce an additional phase into this loop that depends on their PWM settings. This additional phase must be characterised so that it can be accounted for. When we send light into input 2 and monitor output 2 while scanning the PWM settings for phase shifter 4, we obtain a sinusoidal curve with an offset given by this additional phase. This offset therefore gives us a method for measuring this phase. We measure this phase for 13 PWM settings that span the whole PWM range for both MZIs 1 and 2, and then interpolate between these 13 settings to obtain phase estimates for every PWM setting. We note that for MZI 4, $\phi_4(x)$ does not affect the interference in the circuit and we therefore do not need to measure it.

The last optical element to be characterised is phase shifter 3, which we model as only introducing an additional phase shift $\phi_3(x)$ into the bottom waveguide in the closed loop

between modes 2 and 3 for each PWM setting x . $\phi_3(x)$ can be straightforwardly determined using the modulation curves used to find $\phi_N(x)$ for MZIs 1 and 2, as described in the previous paragraph. The action of phase shifter 3 can straightforwardly be modelled using the same formalism as above by a T_3 matrix which is identity except for the last term which is $e^{i\phi_3}$.

Once we have estimated $T_j(x)$ for every PWM setting and for all MZIs and the phase shifter, we store these values in a look up table to be used in the next step of the decomposition process.

Implementing a decomposition

We now proceed to determine which PWM settings should be used for the optical elements in order to implement a transformation given by a unitary matrix U . To do this, we use an adapted version of the decomposition method described in the previous section. We aim to find parameters x_1, x_2, x_3 and x_4 such that $U = DT_4(x_4)T_3(x_3)T_2(x_2)T_1(x_1)$, where D is a diagonal matrix corresponding to single mode phase shifts, and where we have expanded the previously 2×2 T_N matrices to describe the action of the corresponding MZIs and phase shifter within the expanded 3×3 Hilbert space describing the couplings between all three modes.

We first determine the correct PWM setting for MZI 1 by attempting to null the $(1, 3)$ element of U . To do this, for every x we first look up $T_1(x)$ from our look up table, calculate $T_1^{-1}(x)$ then right multiply U by $T_1^{-1}(x)$. Since the phase at the input of the interferometer does not matter, for every x we can treat this phase as a free parameter and multiply the third column of U by whatever phase minimises the $(1, 3)$ element of $UT_1^{-1}(x)$. The desired PWM setting x_1 for MZI 1 is the value of x that minimises the $(1, 3)$ element of $UT_1^{-1}(x_1)$.

over the entire range of PWM settings and possible phases for the third column of U .

We then determine the correct PWM setting for MZI 2 by attempting to null the (1, 2) element of $UT_1^{-1}(x_1)$. Once again, x_2 is the PWM setting that minimises the (1, 2) element of $UT_1^{-1}(x_1)T_2^{-1}(x_2)$. We treat the phase of the first column of U as a free parameter for this minimisation process.

The correct settings for phase shifter 3 and MZI 4 are determined jointly, by attempting to null the (2, 3) element of $UT_1^{-1}(x_1)T_2^{-1}(x_2)$. The reason for their joint determination is that the two of them together form the basic phase shifter and reconfigurable beam splitter elements that implement the $T_{m,n}$ matrices described in the previous chapter. We jointly optimise over x_3 and x_4 such that the (2, 3) element of $UT_1^{-1}(x_1)T_2^{-1}(x_2)T_3^{-1}(x_3)T_4^{-1}(x_4)$ element is minimised.

We should now have:

$$UT_1^{-1}(x_1)T_2^{-1}(x_2)T_3^{-1}(x_3)T_4^{-1}(x_4) = D \quad (5.4)$$

where D should be almost but not quite diagonal due to the both discrete and finite tuning range of the optical elements. This leads to the desired result:

$$U = DT_4(x_4)T_3(x_3)T_2(x_2)T_1(x_1) \quad (5.5)$$

Programming the x_N settings into the four reconfigurable elements in the circuit should therefore implement transformation U to within single mode phase shifts at the input and output and some mixing described by matrix D .

Experimental results

To test our 3×3 universal multiport interferometer, we start by randomly selecting a 3×3 unitary matrix U to be implemented with our device. We perform the decomposition procedure described above and program the resulting PWM settings for the three MZIs and the phase shifter. We measure the resulting transformation by sending light into one input, measuring the power at the three outputs, and normalising the sum of these three powers to one. We repeat this process for the other two inputs, thus constructing a 3×3 transfer matrix S describing all 9 input-output relations. We repeat this process for 50 randomly selected unitary matrices and experimentally measure the transfer matrices for all of them.

We now aim to compare the measured transfer matrices to the targeted unitary matrices. We note that whereas S operates on light intensities, U operates on amplitudes. We use the following fidelity measure $F(S, U)$ to compare them:

$$F(S, U) = \frac{1}{3} \sum_{i,j} |\sqrt{S_{i,j}} U_{i,j}| \quad (5.6)$$

This fidelity measure corresponds to the classical fidelity for the distribution of single photon output probabilities when a single photon is injected into a given input, averaged over all three inputs. We find an average fidelity of 97.5% over these 50 randomly selected unitary matrices, which shows that our implementation of a universal multiport interferometer was successful. The histogram of these fidelities is shown in fig. 5.7, which shows that apart from a few outliers with low fidelity, most transformations were achieved with a fidelity higher than 0.96.

Limitations to the fidelity

Our average fidelity of 97.5% is limited by the following factors. First, even if the optical elements in the circuit exactly implement the desired T_N transformations, their both finite and discrete tuning range implies that matrix D in equation 5.5 is not quite diagonal and cannot be described as single mode phase shifts. Therefore, interferometers implementing matrices U and $T_4(x_4)T_3(x_3)T_2(x_2)T_1(x_1)$ would have different single photon outcome probabilities and therefore non-unity fidelity. Over the 50 matrices that we selected, we numerically find that in the absence of any other imperfection we would expect an average fidelity of 98.8%.

Another significant issue is the multimode behaviour of our couplers, which our model using equation 5.3 cannot account for. Our model assumes balanced and phase-independent loss at all inputs and outputs. In particular, whereas our model assumes that the loss per MZI is independent of its PWM setting, so that the sum of the two output powers per MZI should be constant, we find that in practice this is not the case. Fluctuations in the sum of the powers can sometimes be explained by unbalanced losses at the outputs of the MZIs; however, even after accounting for this effect as described earlier we still find fluctuations in the sum of the output powers in the order of 10-20% over the range of PWM settings. Furthermore, the multimodeness at our couplers causes reduced visibility of the interference at the couplers which causes background light that is not accounted for in our model.

A second effect that degrades our fidelity is the thermal crosstalk between phase shifters. This effect is mitigated in our case by the fact that none of the phase shifters that are used to implement the decomposition are next to each other. Given that the crosstalk for neighbouring phase shifters was previously found to be roughly 1%, and that the coupler multimodeness is expected to be the main source of error, we choose to not account for the

crosstalk in this implementation of a 3×3 universal multiport interferometer.

One last error that degraded the fidelity in our data is the presence of two transfer matrices in our measured data set that are very far from their target U , with fidelities below 90% (see Fig. 5.7). Four additional matrices have fidelities between 0.9 and 0.95, whereas all the others have fidelities above 0.95. We have observed a communication issue between our computer and our control board which rarely causes commands to not be executed; this issue may be responsible for the two outlying fidelity values.

5.4 Conclusion

In this chapter, we proposed a modular architecture for building reconfigurable multiport interferometers. This architecture, consisting of identical silica-on-silicon chips that can be assembled to build large circuits, can provide more experimental flexibility than monolithic interferometers. Using three of our modules, we experimentally demonstrated that we could implement a wide range of optical transformations, including the universal transformations discussed in the previous chapter.

Photon Detectors

The final step in a linear quantum optics experiment consists of performing a measurement on a set of optical modes. The choice of measurement and detector depends on the experimental scheme. Here, we focus on measurements in the photon number basis, which are used in many areas from boson sampling^[62] to universal quantum computation^[50]. We reviewed some of the most commonly used photon detectors in part 1 of this thesis.

In this chapter, we focus on two fields of study within that of photon detection. In the first section, we address the issue of measuring photon detection efficiencies. We describe an experimental scheme for measuring this efficiency without using an external reference, which we demonstrate using two types of detectors. In the second section, we describe the operation of transition edge sensors, which are of particular interest for experiments in which high efficiencies and photon number resolution are required.

6.1 Measuring the efficiency of photon detectors

For optical quantum information tasks, the efficiency of a photon detector is often its most important attribute. High system efficiencies are necessary in metrology to demonstrate quantum enhancements over classical strategies, and in quantum information processing protocols to exceed loss-tolerance thresholds. For example, quantum-enhanced phase estimation can be demonstrated with Holland-Burnett states if the total system efficiency is greater than 70%^[183], and efficient linear optical quantum computation is possible in principle if the product of source efficiency and detector efficiency is greater than two thirds^[184].

Measuring detector efficiencies is a difficult problem; calibrating a detector requires a calibrated light source, but making a calibrated light source typically requires a calibrated detector in the first place. Being able to accurately measure such efficiencies is an important part not only of demonstrating that high efficiencies have been attained, but also of characterising systems with complex responses such as TESs^[185]. Accurate calibration can be done independently in metrological institutes, for example using cryogenic electrical substitution radiometry^[186]. This technique involves comparing the heat generated by optical absorption to that generated by Joule heating in a cryogenic optical absorber with a known resistance to determine the input optical power. However, this solution is costly and technically challenging. Furthermore, power meter efficiencies can drift over the time scale of a year and are affected by environmental conditions. Ideally, measurements of photon detector efficiency would be performed without resorting to these institutes.

Another commonly used approach for measuring efficiencies involves using a photon pair source, where each photon of the pair is sent to a different detector. By measuring the ratio of coincidence counts between the detectors to single counts where only one detector fires,

the total system efficiency from the photon pair source to the detectors can be inferred^[187].

However, this technique requires both a photon pair source at the right wavelength and accurate measurements of the losses through the entire system to single out the detector efficiency. The requirement for a photon pair source in particular can be burdensome, so this method is not always suitable.

In order to solve this detector calibration problem, we follow the work of T. Lunghi *et al*^[188] and B. Sanguinetti *et al*^[189] and develop our own absolute calibration system that does not require a photon pair source. The objective of this work is to greatly improve our calibration accuracy over the 12% previously achieved in our research group using a more rudimentary method^[185]. We use this method to calibrate four SNSPDs and four InGaAs SPADs, both to within a relative error of 2.6%.

6.1.1 Overview of the scheme

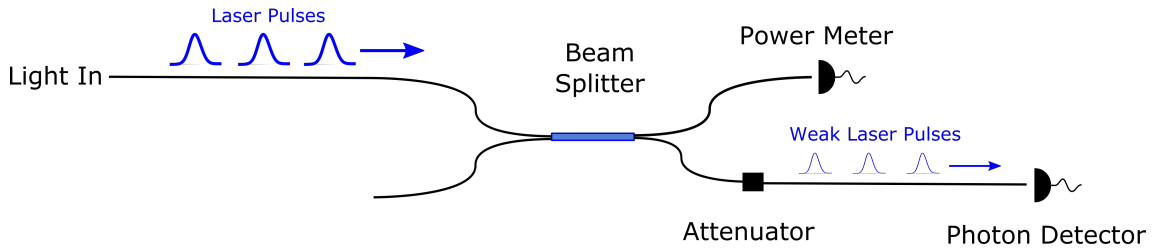


Figure 6.1: Overview of the scheme for measuring the efficiency of photon detectors. A train of laser pulses is sent to a beam splitter. One output of this beam splitter is sent to a power meter, and the other is attenuated so that the resulting coherent states have single photon level intensities. The beam splitting ratio, power meter and attenuation factor are all calibrated so that the intensity of these weak pulses is known to high accuracy. The pulses are then measured by a photon detector. Comparing the response of the detector to the known intensity of the weak pulses allows us to determine the efficiency of the photon detector.

An overview of the scheme that we use for measuring the efficiency of photon detectors is shown in figure 6.1. Our experimental method for implementing this scheme consists of three steps, detailed in the following sections. In the first step, we assemble a radiometer

using standard fibre optic components, and use this radiometer to calibrate a commercial optical power meter. In the second step, we build and calibrate an optical attenuation stage. In combination with the optical power meter calibrated in the first step, we use this attenuation stage to produce calibrated weak optical pulses. In the third step, these weak pulses are sent to a photon detector. By comparing the number of photons detected to the known intensity of these weak pulses, the efficiency of the photon detector can be inferred. Our implementation of this experimental scheme is based on previous work by T. Lunghi *et al*^[188].

The main figure of merit for this scheme is the error that can be achieved in the final estimation of the photon detection efficiency. Lunghi *et al*^[188] report a total relative error of 0.73%. In each of the following sections, we identify and quantify the main sources of error in order to achieve an estimate of the overall error.

6.1.2 Radiometer

The calibration process for measuring the efficiency of a photon detector requires a calibrated optical power meter. Standard off the shelf commercial power meters are usually calibrated to about $\pm 5\%$. Higher accuracies down to below 10^{-4} can be reached by metrological institutes using a cryogenic radiometer and dedicated equipment^[190]. Such radiometers can then be used as a reference against which to calibrate some commercial power meters to typical accuracies of about 1-2%. However, it can be impractical to use these calibrated commercial power meters; they tend to be expensive and their calibration drifts over time.

It was shown by B. Sanguinetti *et al*^[189] that a radiometer can be built using standard fibre optic components, and T. Lunghi *et al*^[188] demonstrated that such a device can be used

to measure the efficiency of photon detectors with an accuracy better than 1%. The following first describes the working principle of this radiometer, then describes its implementation, and finally discusses our calibration results.

Working Principle

A power meter that is uncalibrated but assumed to be linear obeys the following law:

$$P_{measured} = kP_{real} \quad (6.1)$$

The objective of the calibration process is to determine k with good accuracy.

To determine k , the scheme proposed by B. Sanguinetti *et al* uses the physical properties of optical gain media. We first consider a spontaneous emitter of radiation that emits an average number of photons g into a given optical mode. If this mode is initially populated with seed light containing an average number of photons N_{in} , then by stimulated emission the emitter emits an additional average number of photons gN_{in} . After interacting with this gain medium, the optical mode under consideration therefore contains the following average number of photons, which is the sum of the spontaneous emission, the stimulated emission, and the initial number of photons:

$$N_{out} = N_{in} + gN_{in} + g \quad (6.2)$$

This expression can be rewritten as:

$$N_{out} = GN_{in} + G - 1 \quad (6.3)$$

where $G = g + 1$ is the optical gain through the medium. G can be accurately determined with a linear power meter:

$$G = \frac{P_{\text{stimulated}}^m - P_{\text{spontaneous}}^m}{P_{\text{in}}^m} \quad (6.4)$$

where the superscript m refers to the measured power at the power meter. Importantly, the value of G is independent of that of the calibration factor k .

Equation 6.3 is the basis for the radiometry scheme proposed by B. Sanguinetti *et al.* To see why, consider the spontaneous emission term in this equation. For any given optical mode, the average number of photons spontaneously emitted into that mode is determined only by G , which can be measured by an uncalibrated linear power meter. Knowing the gain, one can therefore in principle know exactly the number of photons that is emitted by the gain medium by spontaneous emissions and use this information as an absolute reference against which to calibrate a power meter.

To make use of equation 6.3, which applies only to a single optical mode, we need to relate it to a more readily measurable quantity such as an optical power. In single mode fibre, relating the average number of photons in the fundamental mode to an optical power requires counting the number of polarisation and temporal optical modes per second in the optical field that is being measured. It has been shown^[191,192] that, during a time T , an electric field can be decomposed into T/τ_c independent modes, where τ_c is related to the autocorrelation function γ of the electric field as follows:

$$\tau_c = \int_{-\infty}^{+\infty} |\gamma(t)|^2 dt \quad (6.5)$$

where we have normalised γ such that $\gamma(0) = 1$. τ_c is known as the coherence time of the light. Conveniently, it can be shown using equation 6.5 and the Wiener-Khinchin theorem, which relates the autocorrelation function to the power spectral density, that the number of modes per second within a frequency range $\Delta\nu$ with a constant optical power across this range is exactly $\Delta\nu^{[189]}$. Within such a frequency range, the power in an optical fibre is therefore the number of modes per second $\Delta\nu$, times the average number of photons per mode N_{out} , times the energy per photon $h\nu$, times 2 for the two possible polarisations. The total power from the spontaneous emission is calculated by integrating over the spectrum of the measured light:

$$P_{sp} = \int_{-\infty}^{+\infty} 2h\nu(G(\nu) - 1)d\nu \quad (6.6)$$

This expression yields an absolute optical power which can be used to calibrate optical power meters, and only requires a linear (but not necessarily calibrated) power meter for gain measurements and knowledge of the spectrum of the measured light.

In practice, it can be more convenient to use the power of the seed light as an absolute reference, since the properties of the seed can be more easily controlled than those of the spontaneous emission. Within a frequency range $\Delta\nu$, the optical powers for the spontaneous and stimulated emissions can be written as:

$$P_{sp}(\nu) = 2h\nu(G(\nu) - 1)\Delta\nu \quad (6.7)$$

$$P_{st}(\nu) = 2h\nu(G(\nu)N_{in} + G(\nu) - 1)\Delta\nu \quad (6.8)$$

The average input number of photons per mode is therefore:

$$N_{in} = (1 - 1/G(\nu))(P_{st}(\nu)/P_{sp}(\nu) - 1) \quad (6.9)$$

$P_{st}(\nu)/P_{sp}(\nu)$ being a ratio of powers, this quantity is independent of k and can be measured accurately using a spectrometer. The absolute power of the seed light is therefore:

$$P_{in} = \int_{-\infty}^{+\infty} 2h\nu(1 - 1/G(\nu))(P_{st}^m(\nu)/P_{sp}^m(\nu) - 1)d\nu \quad (6.10)$$

where the superscript m still refers to the measured powers. We note that as opposed to equation 6.6, this expression only requires measuring the gain over the bandwidth of the seed light as opposed to the entire bandwidth of the spontaneous emission.

Experimental setup for the Radiometer

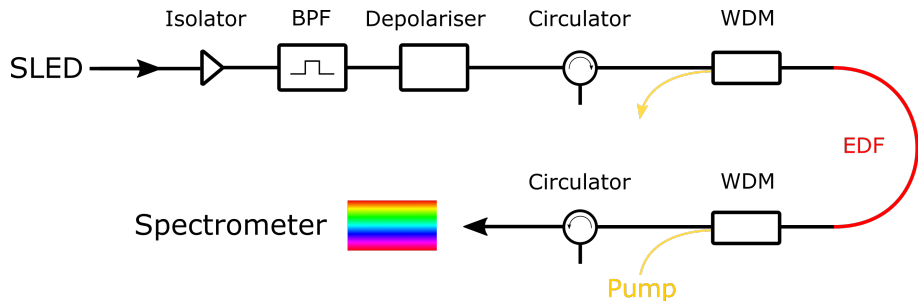


Figure 6.2: Overview of the radiometer set-up. Seed light from a source of amplified spontaneous emission (SLED) is prepared using a band pass filter (BPF) and a depolariser. It is then sent through an erbium-doped fibre (EDF) which is pumped using counterpropagating light that is coupled in and out of the system with wavelength demultiplexers (WDM). By measuring the spectra of the input light and both the stimulated and spontaneous emissions from the EDF, P_{in} can be determined to high accuracy. Isolators and circulators are used in this system to reduce backreflections.

Figure 6.2 shows a sketch of the optical setup that we use to realise the radiometer. It is based on the work by Sanguinetti *et al*^[189].

The gain medium is a 20 cm length of erbium-doped fibre (EDF). The EDF is pumped by 300 mW of laser light at 980 nm that is injected and removed using wavelength demultiplexers (WDM), and propagates counter to the seed light to minimize the amount of stray pump light that could reach the measurement equipment. Several precautions are taken to ensure that the EDF can indeed be modelled as an ideal gain medium. The short length of the EDF ensures both that intrinsic optical losses are negligible and that the gain is small enough to avoid gain saturation. Circulators are present at both the input and output of the EDF to prevent backreflections that could cause unwanted stimulated emission in the EDF. Furthermore, the high power of the pump light ensures that the EDF is fully inverted so that the gain remains stable and is not affected by small fluctuations in the pump power.

The seed light is produced by a superluminescent light emitting diode (SLED). Once again, precautions are taken to ensure that this light is suitable for our radiometry scheme. An isolator at the output of the SLED prevents backreflections that could affect its optical power. Light from the SLED is filtered down to a 3 nm bandwidth and attenuated to prevent gain saturation. The seed light is also sent through a depolariser to ensure that both polarisations contribute equally to the measured power. Furthermore, we find that the emission from the SLED is very stable over time.

Operation of this radiometer requires careful accounting for optical losses. This is because the operating principle of the radiometer as described above requires knowledge of the optical power just before and just after the gain medium to estimate the gain; however in our setup measurements are performed after the light has already propagated through lossy connectors or WDMs. Optical losses after the EDF can be measured by sending seed light through the setup with the pump light turned off and measuring the power immediately

after the EDF and just before the detector. The connector loss at the input of the EDF can also be measured^[189]. These measurements are performed using an integrating sphere photodiode, since these detectors are insensitive to inconsistencies in handling the fibres the output of which is being measured. Furthermore, we account in our measurements for the return loss from an unterminated optical fibre, which is typically 3.4%.

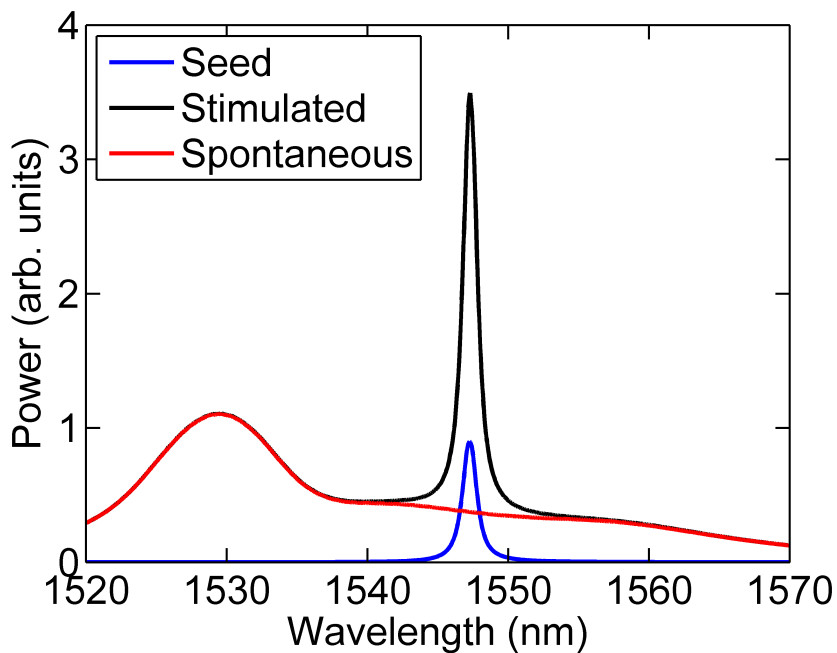


Figure 6.3: Spectra measured for the radiometry process. The blue, black and red spectra respectively indicate the spectra for the seed light, the stimulated emission, and the spontaneous emission. The seed spectrum was measured independently of the other two at a much higher power, and is shown here in the same graph for illustrative purposes only.

Measurements of the spectra of the seed light and of the spontaneous and stimulated emissions are performed using an optical spectrum analyser (OSA). Figure 6.3 shows measured spectra for a given run of the radiometer. The powers for the stimulated, spontaneous, and seed light are all measured using the same integrating sphere photodiode, the linearity of which had previously been verified over the range of powers that was measured. These powers are used to determine the total gain experienced by the seed light averaged over its

spectrum; the spectral distribution of this gain is then inferred from both the spectrum of the spontaneous emission and that of the seed.

Error estimation

In principle, the radiometry setup discussed above can yield an absolute power of the seed light that can then be used to measure the calibration factor k of commercial power meters. However, two types of error can occur due to experimental imperfections.

First, our estimate contains some degree of imprecision. Every run of the radiometer yields a slightly different value for the calibration factors. We perform 11 separate measurements of the calibration factors of a Newport 818-IG/DB InGaAs power meter using our radiometer, and use the standard deviation of these measurements as our estimate of the precision. We find a standard deviation of 1.7%, which is higher than the value of 0.4% reported by Lunghi *et al.* We attribute part of this error to tension inadvertently applied to fibres in the setup during the measurement process, which slightly changes the transmission through fibre connectors. We expect that this issue can be solved by making our setup less compact.

There may also be a systematic error due to imperfections in the setup or in the protocol. One such imperfection is residual polarisation of the seed beam when it enters the EDF, due to polarisation dependent loss in the WDM or imperfect depolarisation. This affects our results since the theory of operation of the radiometer assumes that the seed light is matched to the spontaneous emission, which is depolarised. We estimate that this source of imperfection can lead to a 1% error in our result, which added to the (assumed to be uncorrelated) 1.7% error discussed in the previous paragraph leads to a total error for our

radiometer of 2%.

There may also be other undetected sources of systematic error. Lunghi *et al*^[188] found that their setup, which ours is based on, yielded calibration values that were within 0.2% of those measured by a metrological institute. In the absence of the resources of a metrological institute, we compare the calibration factor yielded by our radiometer for a Newport 818-IG/DB InGaAs power meter to its specified accuracy of $\pm 2\%$. We find a calibration factor of $k = 0.98 \pm 1\%$, which is within the specifications for this power meter and gives credence to our protocol.

We use the results of this radiometer in the next two steps of the procedure for estimating the efficiency of photon detectors. We assume that the radiometer is accurate and use the Newport 818-IG/DB InGaAs power meter as the calibrated power meter to be used in the following (see Fig.6.1). Our estimated 2% error on this calibration will be used in the final tally of the overall error on the efficiency estimate.

6.1.3 Attenuation Stage

An attenuation stage is needed to bridge the gap between the macroscopic light pulses that can be measured with optical power meters and the weak pulses that are to be used for measuring the efficiency of photon detectors. We require roughly 80 dB of attenuation.

Experimental Setup for the Attenuation Stage

The setup for the attenuation stage is shown in Fig. 6.4. The objective of this setup is to use power measurements at A to precisely determine the output power at D. This objective requires measuring the splitting ratio between A and D. Since the desired 80 dB of attenuation is beyond the linear dynamic range of standard power meters, the attenuation

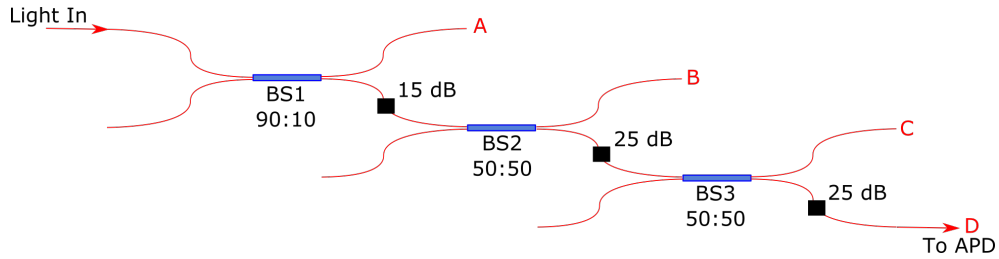


Figure 6.4: Sketch of the attenuation setup. BS: Beam Splitter, with splitting ratios indicated. The black boxes correspond to attenuators, with the attenuation indicated. The other outputs from the beam splitters are used for calibration.

setup is composed of three stages. To measure the total splitting ratio, we first send light into the input of BS3, and we measure the C/D ratio. BS2 is then connected to BS3, light is sent into BS2, and we measure the B/C ratio. Finally, BS1 is connected to BS2, light is sent into BS1, and we measure the A/B ratio. The product of these three ratios is the desired A/D ratio.

Several factors must be taken into account for this measurement process. First, the light source must be stable, at the wavelength at which the power meter was calibrated, and its polarisation state must be known in order to account for the polarisation dependent loss present in most beam splitters. To meet these requirements, we use the same SLED that we used for the radiometry setup, to which we add an isolator, a band pass filter, a depolariser, and a polariser. The combination of the depolariser and of the polariser leads to polarised output light the power of which is independent of polarisation fluctuations in the SLED. The rest of the attenuation setup then uses polarisation maintaining elements. The power measurements are once again performed using an integrating sphere photodiode the linearity of which we had previously characterised and found to be about 0.2% over the range that we are interested in.

Error Estimate

The error in the attenuator can be estimated from the following elements:

- Repeatedly measuring the splitting ratio of a given beam splitter yields a standard deviation of 0.2%. This leads to a total error for the splitting ratio of all three beam splitters of 0.35%.
- The nonlinearity of the integrating sphere power meter was measured to cause at most 0.2% error in the estimate of each splitting ratio. Since this error is not independent for the three beam splitters, this causes a total error due to the nonlinearity of 0.6%. We note that this source of error could in principle be accounted for in the measurement process.
- The beam splitters are polarisation-dependent and exhibit polarisation-dependent loss, but do not perfectly preserve the input polarisation. Even with perfectly polarised light at the input, the polarisation would change as it propagates through the attenuation stage, which affects the splitting ratios. Also accounting for the initial degree of polarisation of the input light, we find that the error caused by this effect is bounded at 1.1%.

Since these three sources of error are uncorrelated, the total error for the measurement of the attenuation ratio is 1.3%.

6.1.4 Photon Counting

We use the setup described in Fig. 6.1 to measure the efficiencies of two kinds of photon detectors: single photon avalanche diodes (APDs) and superconducting nanowire single

photon detectors (SNSPD). We use a different approach for each of these two types of detectors; for SPADs, pulsed light is used, whereas for SNSPDs continuous wave (CW) light is used. Both approaches involve comparing the number of photons detected by the detectors to the intensity of the light that they measure.

Superconducting Single Photon Detectors

We first measure the efficiencies of four tungsten silicide (WSi) superconducting nanowire single photon detectors. These detectors are polarisation sensitive, and we aim to measure their peak efficiency.

We use the following measurement procedure. Our light source is a filtered and polarised CW SLED. Its power is set in such a way that about 30000 photons per second arrive at the detector, and its polarisation after the attenuation stage is controlled by fibre polarisation rotators to maximise the number of counts at the detector. The SNSPDs are kept inside a dilution refrigerator at 40 mK, and their bias voltage is set to maximise the efficiency while keeping their dark count rate below 100 Hz. We record counts for 10 seconds, subtract the estimated number of dark counts from the total, and compare the result to the input number of photons.

We estimate the error due to the drift in the laser power to be negligible over the measurement time, and the statistical error from the photon counts is typically about 0.2% given that about 300000 counts are recorded for each measurement. Separately, we find that turning the fibre polarisation rotators can cause a roughly 1% change in the output power. The error from the photon counting process is therefore dominated by the effect of these polarisation rotators. The overall relative error for the entire photon detection efficiency

process from the radiometry to photon counting is therefore 2.6%.

We find the following efficiencies for our four WSi SNSPDs, which are typical for these devices. The variations in efficiencies may be caused by a combination of imperfections in fabrication, differences in splicing, and connector losses.

SNSPD	Efficiency
SNSPD 1	78% ($\pm 1.0\%$)
SNSPD 2	91% ($\pm 1.2\%$)
SNSPD 3	87% ($\pm 1.2\%$)
SNSPD 4	82% ($\pm 1.1\%$)

Table 6.1: Estimated photon detection efficiencies for four WSi SNSPDs.

SPADs

We also measure the efficiencies of four single photon avalanche diodes. Commercial InGaAs SPADs operating at telecom wavelengths typically have a dark count rate of several kHz and a hold off time of about $10 \mu s$. To make our calibration procedure insensitive to these effects, we use pulsed light at the input of the attenuator, and only consider photon counts from the SPAD within a small time window corresponding to the time at which pulses reach the detector.

We use the following measurement procedure. The pulsed light is generated by a laser diode at 1548 nm that is driven by an electrical pulse generator. The laser emits pulses with a repetition rate of 10 kHz, and an average photon number after attenuation of about 0.02. We keep the photon number low in order to prevent two photon events from occurring. The measurement time is 200 s, which we find allows us to record a sufficient number of clicks to have low statistical error and is short enough to prevent the laser power from drifting significantly.

We estimate the error due to the drift in the laser power to be 0.4% over the measurement time, and the statistical error from the photon counts is typically about 1% given that about 10000 counts are recorded for each measurement. The total error from the photon counting process is therefore 1.1%. The overall relative error for the entire photon detection efficiency process from the radiometry to photon counting is therefore 2.6%.

We use this measurement procedure to estimate the efficiencies of four different SPADs. These four SPADs have different settings for the bias voltage and hold off times that affect their efficiency. We find the following peak efficiencies, which are once again as expected:

SPAD	Efficiency
SPAD 1	24.0% ($\pm 0.3\%$)
SPAD 2	23.1% ($\pm 0.3\%$)
SPAD 3	20.0% ($\pm 0.3\%$)
SPAD 4	19.0% ($\pm 0.3\%$)

Table 6.2: Estimated photon detection efficiencies for four InGaAs SPADs.

6.2 Operation of transition edge sensors

Due to their exceptionally high efficiencies and photon number resolving capabilities, transition edge sensors are of particular interest to quantum optics. The following section describes the TESs that we use for our experiments, the dilution refrigerator that we use to keep them cold, and the method of operation of the TESs.

6.2.1 Experimental apparatus

Transition Edge Sensors

For our experiments, we use four TESs fabricated by the National Institute of Standards and Technology (NIST)^[193]. These TESs consist of $25\mu\text{m} \times 25\mu\text{m} \times 20\text{ nm}$ slabs of tungsten

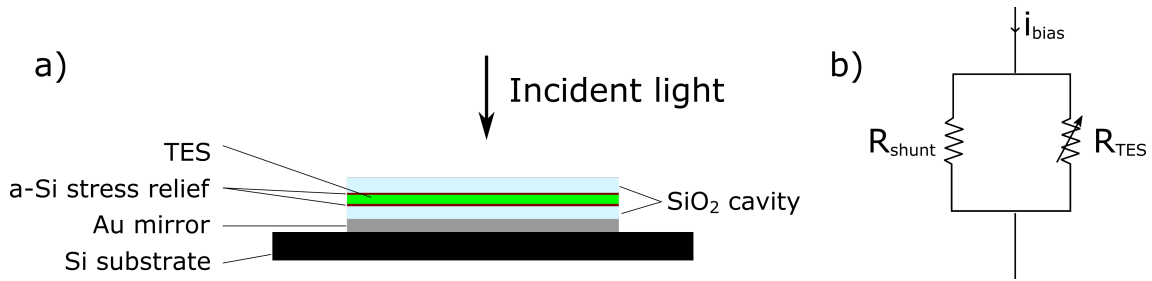


Figure 6.5: a) TES structure. The TES is located within a silica optical cavity with a silver back reflector, and this structure is built on a silicon substrate. b) Diagram of the circuit used to lock the TES to its transition temperature.

inside an optical cavity designed to maximise absorption at 1550 nm. Tungsten is an ideal material for TESs since it can simultaneously provide high optical absorption, small heat capacitance, and a weak thermal link to restore them to their original temperature^[142].

The TESs are first cooled below their transition temperature of about 100 mK, and then heated back to their transition temperature by applying a bias current with the circuit shown in figure 6.5. This circuit also locks the TES to its transition temperature via an electro-thermal feedback effect^[142]. With this constant bias current and with a shunt resistor in parallel, if the temperature of the TES decreases its resistance also decreases. More current then gets shunted towards it, thus providing additional heating via the Joule effect. Conversely, if its temperature increases then the resistance also increases, leading to less Joule heating. Furthermore, this electro-thermal feedback effect allows the TES to return to its initial temperature after photon absorption more quickly than the weak thermal link would allow on its own^[194].

At the transition temperature of the TES, its resistance is very sensitive to small changes in temperature, with $d(\log R)/d(\log T) \approx 100$ (see Fig. 3.3). When a photon is absorbed, the resistance of the TES increases. For this increase to be measurable, both a very small TES heat capacity and low noise levels are necessary. Heat capacity decreases with temperature.

Furthermore, the main sources of noise, phonon noise and Johnson noise, are temperature dependent^[195]. Operating the TES at 100 mK allows us to satisfy both conditions. To keep them at this temperature, the TESs are operated inside a dilution refrigerator and kept inside a sealed box to protect them from surrounding black body radiation. After a photon absorption event, it takes about 5 μ s for the TES to return to its original temperature, via the electro thermal feedback effect.

The number of photons that can be resolved with a TES depends on the width of its transition region. There is a trade off between noise and the number of photons that can be resolved, which is determined by the dimensions of the TES. A larger TES will have smaller increases in temperature when absorbing photons so will be able to resolve more photons within its transition region, but the noise will decrease the ability to clearly distinguish between photon numbers. Conversely, a smaller TES will be able to resolve fewer photons but with less noise. Our TESs were designed to clearly resolve up to about 12 photons, although higher photon number resolutions can be attained with more involved data analysis techniques^[144].

Optics

To maximise the detection efficiency at our chosen wavelength of 1550 nm, the TES is located in an optical cavity with a silver back reflector, and the input optical fibre is positioned to within 10 μ m of the TES surface. In principle, detection efficiencies of 98% can be achieved with these devices. Once fibre splices and connector losses are taken into account the final detection efficiency is still typically about 95%^[193], which is still higher than in any other type of photon detector.

The optical fibres that lead to the TESs are at room temperature on the other end, and the resulting blackbody radiation can lead to a significant amount of noise on the detectors. A single mode fibre carrying two polarisation modes that is perfectly coupled to a blackbody emitter at temperature T carries the following amount of optical power^[196]:

$$P = \frac{\pi^2}{3} \frac{(kT)^2}{h} \quad (6.11)$$

where k is the Boltzmann factor and h is Planck's constant. At room temperature (300 K), $P = 85$ nW. The amount of blackbody energy incident onto the TES over the $5\ \mu\text{s}$ duration of the 1550 nm photon detection signal would therefore be 1.75×10^{-14} J, which is orders of magnitude higher than the energy of the detected photon at 1550 which is 1.28×10^{-19} J. Although a lot of this radiation is at long wavelengths that are not transmitted through standard telecom fibre, the transmitted portion can still cause a lot of noise on our TES detectors so we require a method to reduce it significantly. A simple way of doing so involves coiling the fibres inside the cryostat; this introduces significant bending losses for higher wavelengths that are not incurred by the target 1550 nm light. Ten loops with a bending diameter of 2.1 cm has been found to reduce the amount of blackbody radiation by a factor of 10^4 ^[197]. We find that this method allows us to reduce the number of dark counts on both our SNSPDs and TESs to a few tens of Hz.

Electronics

Two amplification stages are required for the signal from the TESs to be read out by standard electronics. First, low-temperature amplification is achieved using superconducting quantum amplification devices (SQUID) designed for this purpose and fabricated by NIST. These

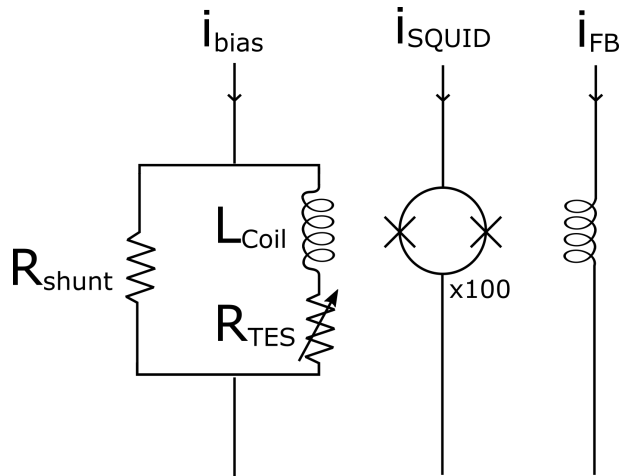


Figure 6.6: Diagram of the low temperature amplification system. When a TES absorbs a photon, its change in resistance translates into a change in current going through the coil. The coil is inductively coupled to an array of 100 SQUIDS which amplify the signal so that it can be sent to room-temperature electronics. Since SQUIDS have a sinusoidal response to the current going through the coil, a feedback bias line is used to set them at the most sensitive point of their response curve.

devices consist of a superconducting ring containing two Josephson junctions in parallel, and are well suited to provide low noise amplification for a low impedance device such as a TES^[195]. To read out the signal from the TES, they are inductively coupled to a coil that is in series with the TES (see Fig. 6.6), so that a change in resistance of the TES translates into a change in magnetic flux through the SQUID. We note that the inductance of the coil limits the signal rise-time to about 100 ns, which in addition to noise in the system places a bound on the achievable jitter. Further amplification is achieved by placing an array of several of these SQUIDS in series so that their responses all coherently add up^[198]. Since SQUIDS have a sinusoidal voltage response to the magnetic flux, a feedback bias line can be used to set the SQUID array at the steepest point of its response curve.

The output signal from this SQUID array is around $10 \mu\text{V}$, whereas the readout electronics we use require mV level signals. We therefore use an additional $\times 100$ low noise two stage pre-amplifier at room temperature placed on the same circuit as the bias electronics. At

these low voltages, the signal from the SQUIDs can easily be corrupted by surrounding RF radiation in the building. The cable to the pre-amplifier is therefore shielded inside a metal conduit. The output from the pre-amplifier is also amplified and filtered using bandpass filters from 1 kHz to 1 MHz to get rid of any excess noise before being fed to our read-out electronics.

6.2.2 Dilution refrigerator

Reaching the low temperatures required to operate our TESs is not straightforward. Relatively simple and compact cryostats that typically rely on the evaporative cooling power of liquid helium can be used to reach temperatures of about 1 K. These cryostats are typically used to operate SNSPDs, for example. However, the vapour pressure of helium decreases with temperature which limits the achievable evaporative cooling power, and alternative cooling methods are required to go significantly below 1 K. In our research group, we use a dilution refrigerator that can reach a base temperature of about 40 mK.

Principle of operation

To reach temperatures below 1 K, dilution refrigerators continually circulate a mixture of two isotopes of helium: ^3He and ^4He (see Fig. 6.7). At temperatures below 1 K, a phase transition occurs and these isotopes are separated into a rich phase that is almost entirely ^3He and a dilute phase which contains 6.4% ^3He . This phase transition occurs in the “mixing chamber” of the dilution refrigerator, which is the coldest part of the cryostat. At the phase transition, we can think of ^3He as evaporating from the rich phase into the dilute phase, and this evaporation process takes energy from the environment and provides the required cooling power. To drive this evaporation process, the dilute phase is connected to a “still”,

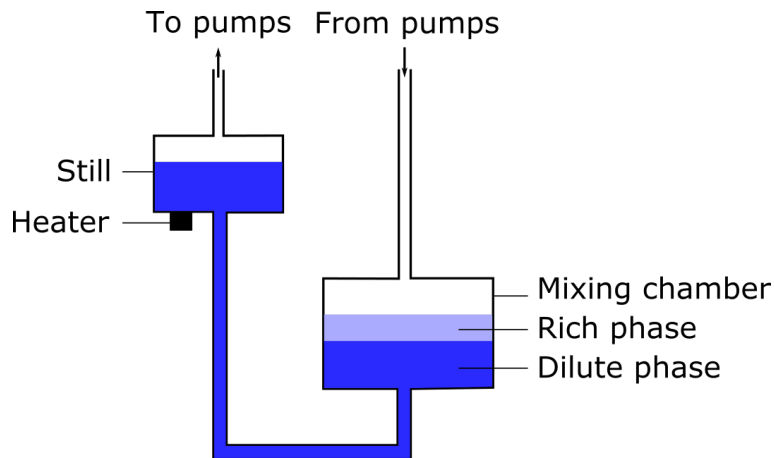


Figure 6.7: Diagram of the circulation of ${}^3\text{He}$ in a dilution refrigerator. At temperatures below 1 K, a phase transition occurs with a rich phase which is mostly ${}^3\text{He}$ and a dilute phase with 6.4% ${}^3\text{He}$. Pumping on the still reduces the concentration of ${}^3\text{He}$ in the dilute phase, which by osmosis pushes ${}^3\text{He}$ from the rich phase through the phase boundary and cools the mixing chamber. A heater at the still drives the evaporation of the ${}^3\text{He}$.

which is continually pumped on so that a low pressure is maintained. In these conditions, the partial pressure of ${}^3\text{He}$ is higher than that of ${}^4\text{He}$ and more of it evaporates than ${}^4\text{He}$. This causes a decrease in concentration of ${}^3\text{He}$ in the dilute phase, which by osmosis causes evaporation of ${}^3\text{He}$ from the rich phase into the dilute phase. A heater at the still is used to maintain a constant rate of evaporation. The ${}^3\text{He}$ is then pressurised at the pumps, cooled by thermal exchangers in the cryostat, and injected back into the mixing chamber to complete the circulation process.

To reach 1 K in the first place so that the phase separation occurs, the dilution refrigerator is kept in an inner vacuum chamber (IVC) inside a bath of liquid ${}^4\text{He}$ which has to be regularly replenished. A small amount of helium from this bath is injected into a 1 K pot inside the IVC where it is continuously pumped on to achieve a temperature of about 1.6 K. This is enough to liquefy the circulating ${}^3\text{He}/{}^4\text{He}$ mixture. Since ${}^3\text{He}$ has a higher partial pressure than ${}^4\text{He}$, evaporation of the ${}^3\text{He}$ in the still allows the system to cool down below 1 K so that the phase transition can happen in the mixing chamber. We note that recent

commercial dilution refrigerators now typically use a pulse tube cooler instead of a bath of liquid ^4He to reach temperatures low enough to liquefy helium.

Description of our experimental system

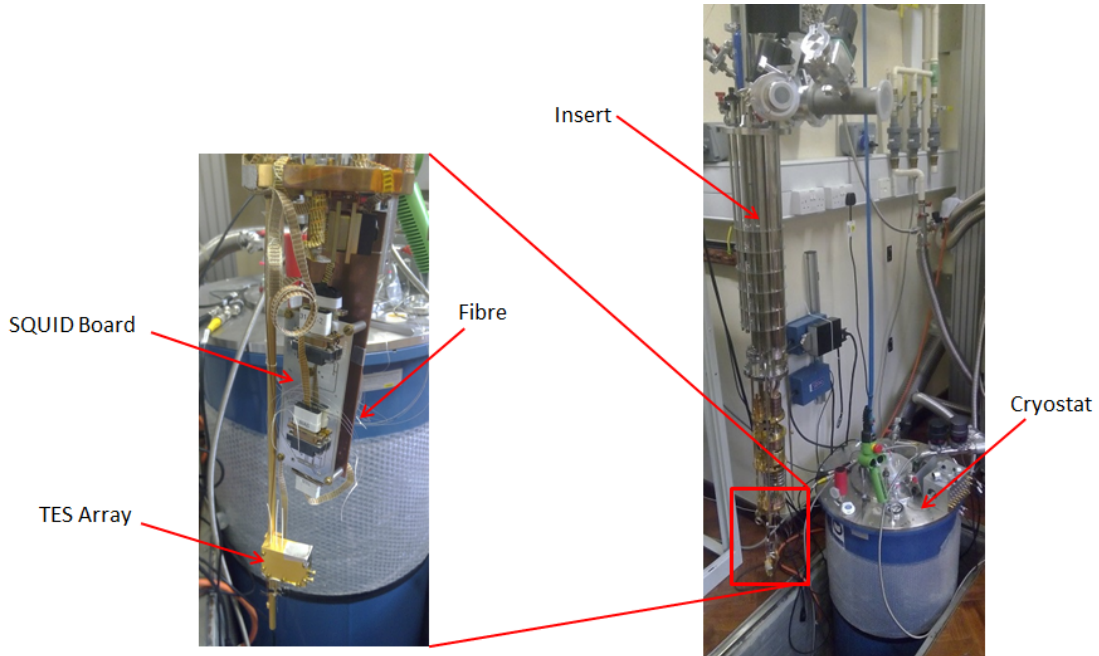


Figure 6.8: Pictures of our dilution refrigeration system.

We use a commercial KelvinoxMX400 dilution refrigerator supplied by Oxford Instruments, which is specified to achieve a base temperature of 12 mK (Fig. 6.8). Dilution refrigerators are large and expensive, and we thus have a dedicated laboratory used specifically for hosting and operating our dilution refrigerator. The cryostat itself is located in a pit (nicknamed the pit of oblivion due to the multitude of screws and O-rings lost inside it), and is connected to several pumps in an adjoining shed. This laboratory is connected via an optical fibre link to our main optics laboratory.

To reach its base temperature, the cryostat has several different temperature stages. A bath of liquid helium is kept inside an outer vacuum chamber. The IVC is sealed off with an

indium seal, located in the helium bath, and contains several thermally isolated plates with different cooling mechanisms. The top plate of the IVC is in contact with the helium so is kept at 4.2 K. The second plate contains the 1 K pot, which is controlled by a needle valve. The third plate contains the still, and the coldest plate at the bottom contains the mixing chamber. We keep both the TESs and the SQUIDs at the mixing chamber stage. The SQUIDs produce some excess heat that increases the base temperature by about 20 mK. They could in principle be placed at the still plate where the cooling power is greater, but space constraints force us to place them on the mixing chamber plate.

Electrical connections to the TESs are made using cryogenic looms consisting of 12 twisted pairs and soldered onto hermetically sealed Fischer connectors at the top of the cryostat. We also have hermetically sealed SMA connectors and coaxial cables that we can use to operate SNSPDs. Optical connections are made using a bundle of 16 bare fibres that go through a hermetic seal to the IVC. These fibres are then fusion spliced to our four TESs and four nanowires at the mixing chamber plate, and to fibre ends screwed into fixed ferrule connectors (FC) in a breakout box at the top of the cryostat.

To circulate the helium mixture, we use three different pumps in an adjoining shed. One sealed roots pump is used to circulate the mixture, and is backed by a sealed rotary pump. Although the mixture circulates in a closed cycle, some impurities can enter the system so we use both a liquid nitrogen cold trap and a helium cold trap. These cold traps consist of porous materials such as charcoal that at low temperatures trap molecules of air but not helium, thus keeping the mixture pure and preventing blockages. Both the main bath and the rotary pump for the 1 K pot are connected to a helium return system for the physics building. Since our system consumes about 150 L of liquid helium a week, this return line

allows us to significantly reduce our operating costs.

Cooldown process

Reaching base temperature from room temperature typically takes about three days. The first, crucial step consists in leak checking the system. Despite the presence of cold traps, if enough air enters the system it can freeze and block the circulation of the mixture. Furthermore, the mixture itself is extremely expensive and must not be lost. ^3He is only commercially produced in very small amounts as a by-product of the nuclear weapons industry, and its cost is in the order of a few thousand pounds per litre. Our dilution fridge uses 16 g of ^3He , so there is a strong incentive to find and fix leaks. To do so, we use a leak detector that consists of a rotary pump with a helium mass spectrometer. When the leak detector pumps on the volume under vacuum, we spray helium all over the outside of this volume and the presence of a leak is heralded by a spike in the amount of helium detected by the mass spectrometer. We can then identify and fix the leak. Once all leaks have been fixed, we then put both the outer vacuum chamber and the inner vacuum chamber under vacuum.

A first precool is achieved by filling the main bath with nitrogen. Nitrogen has a higher enthalpy of vaporisation than helium and is cheaper, so using nitrogen for the precool helps us reduce our costs. Once the inner vacuum chamber has reached liquid nitrogen temperature at 77 K, we evacuate the nitrogen and fill the main bath with helium. When the inner vacuum chamber reaches liquid helium temperature, we turn on the 1 K pot, and then start condensing the mixture into the mixing chamber simply by opening the valves leading to the mixing chamber. Once most of the mixture has condensed, we then start the

circulation by turning on the sealed helium rotary pump. When the pressure at the still is low enough, we can then safely turn on the roots pump. Finally, we turn on the still heater to provide 10 mW of heat to drive the circulation of the ${}^3\text{He}$.

6.2.3 Method of operation

Once the TESs have reached base temperature, the SQUIDs and TESs have to be configured and the output signal needs to be processed to determine the number of photons that was detected.

Configuring the TESs

The bias currents for the TES, the SQUIDs, and the feedback coil (see Fig. 6.6) are all controlled with an 8-channel bias box connected to a low noise voltage source. Each channel can control one TES, and contains three screw-controlled potentiometers to individually set the bias currents. Both the TES bias current and the feedback coil current can be connected to an external function generator. In addition, each channel has a “zap” button that allows to momentarily connect the SQUIDs to a high current source, thus heating them and removing any trapped magnetic fluxes that would reduce the modulation depth.

The first step in configuring the TESs is to set the bias current for the SQUID. When this current is close to the critical current, the Josephson junctions become resistive and a voltage drop occurs that varies sinusoidally with the magnetic flux threading the superconducting loop. We use an external function generator to sweep the feedback loop with a triangular wave, thus creating a linearly varying magnetic flux through the SQUID that translates into an output voltage that varies sinusoidally with time and can be observed on an oscilloscope. The SQUIDs are properly set when the amplitude of their modulation is maximised.

Next, we set the TES bias. We first connect the TES bias line to the external function generator. When the TES is superconducting, most of the current goes through the TES so as this current is swept large modulations of the SQUID output can be observed. When the TESs are normal, most of the current goes through the shunt resistor so the current varies much less, which translates into a flat response of the SQUIDs. The TES bias is close to its correct value when both a superconducting region and a normal region can be seen on the SQUID response within one period of the signal from the function generator.

At this point, when the function generator is turned off weak pulses corresponding to photon detection events should be observed on the TES. These pulses are typically weak because the SQUID bias current is at this point set to a random part of its sinusoidal response curve. We therefore use the feedback bias coil to bias the SQUID to the most sensitive region of its response curve. Further tweaking of the TES bias can also be used to create stronger pulses.

Signal Processing

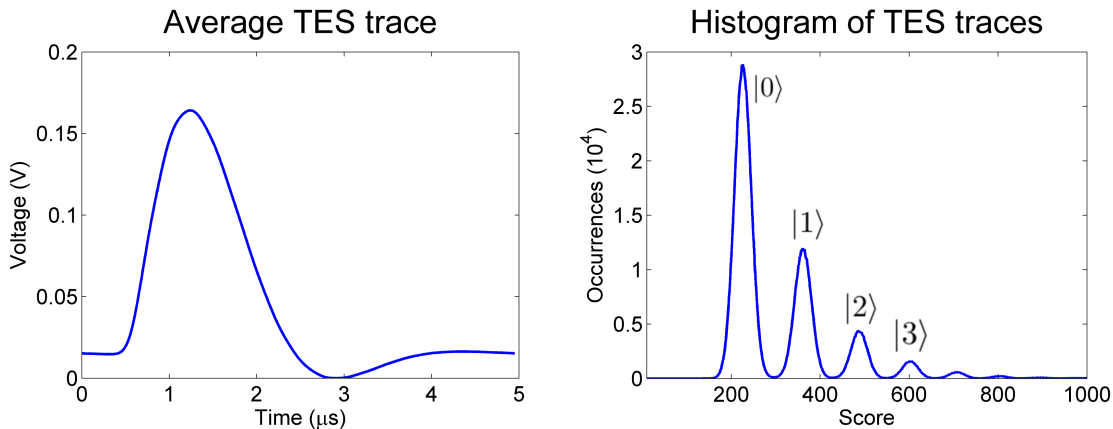


Figure 6.9: Analysing TES traces. A) A typical TES trace such as this one appears as a $5 \mu\text{s}$ long voltage signal. Different photon numbers appear as different traces of different heights. B) For each trace, we calculate a score based on its overlap with a reference trace. Plotting a histogram of these scores for many traces clearly shows different photon numbers.

The output signal from the SQUID is a $5 \mu\text{s}$ time varying pulse (Fig. 6.9a). The detection of different photon numbers corresponds to different pulses, so a processing step is required to extract the photon numbers from the pulses.

After trying several data processing methods^[194], we adopted the following signal processing method that we found to be good at discriminating between different photon numbers. We send the train of pulses to be measured to the detector. These pulses are typically either coherent states or thermal states, which contain a collection of different photon numbers that lead to different responses on the TES. For each pulse, we use a trigger as a signal to start collecting a $5 \mu\text{s}$ long sample containing 500 data points. From the first 16000 traces we collect, we build a histogram of the maximum pulse heights. This histogram is typically noisy and is unsuitable for high-resolution photon number detection, but is enough to identify a threshold pulse height beyond which we are reasonably confident that at least one photon was in the measured pulse. We then use the following pulses to calculate an average trace of all the traces that beat this threshold. We can monitor on screen the build up of this average trace, and once we are visually satisfied that there is not much noise on it we then use it as a reference trace. For all subsequent pulses, we calculate a score for the pulse which is the overlap between this reference trace and the measured trace. Plotting the histogram of these scores clearly shows distinct peaks (Fig. 6.9b). After collecting on the order of 100000 points on this histogram, we allocate a photon number to each peak and bin the calibration pulses, as well as any subsequent pulses, according to which peak they are closest to.

An important figure of merit for this process is how clearly distinct the different peaks are in the histogram of these overlaps. With appropriate grounding of our electronics and

optimisation of the bias currents for the TES and the feedback coil, we can typically reach a minimum between the peaks corresponding to 0 photons and to 1 photon that is less than 5% of the height of the peaks. Given the Gaussian nature of the noise, this gives a probability of mis-attributing the photon numbers in a given trace of less than 0.2%.

Since we operate our experiments that use TESs at a repetition rate of about 100 kHz, fast signal processing electronics are required. We use an Alazar digitiser to calculate the score of every incoming pulse and we store only this score in the computer's memory. Binning these scores into distinct photon numbers can then be done in post-processing.

6.2.4 Experiments

These TESs were used in a wide variety of experiments. In addition to an experiment aiming to simulate molecular spectra discussed in detail in the next chapter, these TESs were used for an experiment demonstrating the concept of detector-independent verification of quantum light^[199,200] and for an experiment demonstrating that optical interference of Fock states can be used to compute a function known as the fractional Kravchuk-Fourier transform^[201].

6.3 Conclusion

In this chapter, we first demonstrated a method for measuring the efficiency of photon detectors that does not depend on an external reference. We used this method to characterise two types of photon detectors. We also described the operation of transition edge sensors, which provide both high efficiencies and photon number resolution. Well-characterised and high efficiency photon detectors will enable a wide range of applications in quantum optics,

such as the simulation of vibronic spectroscopy described in the next chapter.

Part III

Applications of Linear Optics

Quantum Optical Simulation of Vibronic Spectroscopy¹

Simulating quantum processes in nature is a promising application for quantum computers.

Since the size of the Hilbert space used to describe a quantum system increases exponentially with the size of the system, the ability of classical computers to simulate these processes is severely limited. However, a quantum computation device may be able to directly mimic the evolution of a quantum system and yield useful information in a scalable manner. Small-scale demonstrations of quantum simulation protocols with quantum optics have already been performed. Some examples of such demonstrations include the calculation of molecular energies^[145], the determination of ground states of spin chains^[202], and bosonic transport simulations^[59].

In this chapter, we study the use of a linear optics experimental protocol to simulate the vibronic spectra of molecules. We start by explaining what vibronic spectra are and how

¹The contents of this chapter relate to the author's publication entitled "Experimental Quantum Optical Approximation of Vibronic Spectroscopy"

they can in principle be simulated using quantum optics. We then proceed to study the performance of this protocol in the presence of experimental imperfections. First, we show that the protocol for simulating these spectra can be adjusted to account for experimental imperfections, and that the impact of these imperfections can be quantified. We then perform a proof of principle demonstration of this protocol, which illustrates our method for accounting for imperfections. Finally, we discuss our experimental results in light of our analysis.

7.1 Background

7.1.1 Vibronic spectroscopy

Vibronic spectra arise from simultaneous electronic and vibrational transitions in molecules. Molecules have a large number of vibrational degrees of freedom, each of which can be populated with many different Fock states corresponding to different energies. If we consider a molecule with an electronic transition at a frequency ω , due to these many different available vibrational states the molecule will be able to absorb not only photons with energy $\hbar\omega$, but also photons at any energy corresponding to $\hbar\omega$ plus the energy required to excite any one of the vibrational states. Every electronic transition therefore has a complicated spectrum due to these vibrational modes. This spectrum is known as the vibronic spectrum of the molecule.

Since vibronic spectra encode structural information about the molecule and its vibrational degrees of freedom, they play an important role in determining the optical and chemical properties of molecules. In addition to being useful for fundamental research in molecular physics and chemistry, calculating these spectra helps in assessing the performance

of different molecules for applications in photovoltaics^[203], biology^[204], and other forms of industry^[205].

Harmonic approximation of the normal modes of a molecule

Several techniques exist to determine the geometry of a molecule^[206–208]. Once this geometry has been determined, we assume that the motion of the electrons and that of the nuclei can be decoupled^[209]. The vibrational modes under study correspond to the normal modes of motion of the nuclei.

Specifically, we consider a molecule at rest consisting of N atoms. The position and momenta of these atoms are each described by $3N$ spatial coordinates. Since the Hamiltonian corresponding to the respective motion of these nuclei does not depend on the absolute orientation or position in space of the molecule, the Hamiltonian is a function of $3N - 6$ position coordinates q_i and $3N - 6$ momentum coordinates p_i . We note that this becomes $3N - 5$ in the case of linear molecules. We can write this Hamiltonian as follows:

$$H = \sum_i \frac{p_i^2}{2m_i} + V(\mathbf{q}) \quad (7.1)$$

where m_i is the mass of nucleus i and $V(\mathbf{q})$ is the potential energy of the molecule and is a function of all the q_i . The precise expression of $V(\mathbf{q})$ depends both on the electronic configuration of the molecule and its geometry. We perform a Taylor expansion of this potential:

$$V(\mathbf{q}) = V_0 + \sum_i \frac{\partial V}{\partial q_i} q_i + \frac{1}{2} \sum_{i,j} \frac{\partial^2 V}{\partial q_i \partial q_j} q_i q_j \quad (7.2)$$

In this expression, we have performed an approximation, known as the harmonic approximation, where we have neglected coupling terms beyond the second order. We can set $V_0 = 0$, and we can place the origin of the coordinates such that $\frac{\partial V}{\partial q_i} \Big|_{q_i=0} = 0$. The Hamiltonian in 7.1 then becomes:

$$H = \sum_i \frac{p_i^2}{2m_i} + \frac{1}{2} \sum_{i,j} \frac{\partial^2 V}{\partial q_i \partial q_j} q_i q_j \quad (7.3)$$

We now switch to using mass-weighted coordinates \tilde{q}_i and \tilde{p}_i , where $\tilde{q}_i = \sqrt{m_i} q_i$, so that 7.3 can be written as:

$$H = \sum_i \frac{\tilde{p}_i^2}{2} + \frac{1}{2} \sum_{i,j} \frac{\partial^2 V}{\partial \tilde{q}_i \partial \tilde{q}_j} \tilde{q}_i \tilde{q}_j \quad (7.4)$$

The matrix with values $\frac{\partial^2 V}{\partial \tilde{q}_i \partial \tilde{q}_j}$ at position (i, j) is symmetric, so we can perform a singular value decomposition of this matrix with a basis of Q_i and corresponding P_i such that equation 7.4 becomes:

$$H = \sum_i \frac{P_i^2}{2} + \frac{F_i}{2} Q_i^2 \quad (7.5)$$

where the F_i are the singular values.

The Q_i are now independent and correspond to the normal coordinates of the molecule. We can quantise the position and momenta of the molecule, so that the Hamiltonian in 7.5 describes an ensemble of quantum harmonic oscillators where oscillator i has a frequency $\sqrt{F_i}$. Excitations of these normal modes correspond to vibrational excitations.

Mode transformation

The change in configuration of a molecule caused by an electronic excitation causes a change in its normal modes. Within this harmonic approximation, Duschinsky^[210] proposed that the change in mass-weighted normal coordinates associated with the electronic transitions under study can be written as the following change of basis:

$$\vec{Q}' = U\vec{Q} + d \quad (7.6)$$

where U is a real rotation matrix and d is a displacement vector. This is the Duschinsky relation^[210]. This canonical transformation maps onto the creation and annihilation operators \hat{a}^\dagger, \hat{a} associated to the vibrational modes in the following way:

$$\hat{a}'^\dagger = \frac{1}{2}(J - (J^t)^{-1})\hat{a} + \frac{1}{2}(J + (J^t)^{-1})\hat{a}^\dagger + \frac{1}{\sqrt{2}}\vec{\delta} \quad (7.7)$$

where

$$J = \Omega'U\Omega^{-1}, \vec{\delta} = \Omega'\vec{d} \quad (7.8)$$

and

$$\Omega = \text{diag}(\sqrt{\omega_1} \dots \sqrt{\omega_N}), \Omega' = \text{diag}(\sqrt{\omega'_1} \dots \sqrt{\omega'_N}) \quad (7.9)$$

where ω_i and ω'_i are the frequencies of the initial and final electronic state and diag denotes the diagonal matrix^[211,212].

Using the Bloch-Messiah decomposition^[28], we can write:

$$\frac{1}{2}(J - (J^t)^{-1}) = UA_D V^T \quad (7.10)$$

$$\frac{1}{2}(J + (J^t)^{-1}) = UB_D V^\dagger \quad (7.11)$$

where U and V are unitary matrices and A_D and B_D are diagonal matrices with $A_D^2 = B_D^2 + 1$.

Transformation 7.7 can now be interpreted as a change of basis consisting of a first multimode rotation described by V , a set of single-mode squeezing operations with squeezing parameters which are the diagonal elements of $\text{acosh}(A_D)$, a second rotation described by U , and a displacement described by δ . If the initial physical state is the ground state of the harmonic oscillator, for example for a system at 0 K, then rotation V does not do anything and the transformation can be interpreted as a set of single mode squeezing operations, followed by rotation U and displacement δ .

According to the Franck-Condon principle^[213,214], the intensity of a given vibrational transition is proportional to the overlap between the wave function of its initial vibrational state and that of its final vibrational state after the change of basis. If the initial vibrational state is the ground state and the final state, written as $|\mathbf{m}\rangle$, has m_1 energy quanta in mode 1, m_2 energy quanta in mode 2, etc., then this overlap can be written as:

$$P(\mathbf{m}) = \left| \langle \mathbf{m} | \hat{U}_{Dok} | 0, 0 \rangle \right|^2 \quad (7.12)$$

where \hat{U}_{Dok} is the operator implementing mode transformation 7.18, known as the Doktorov operator^[211], that is such that transformation 7.7 can be rewritten $\hat{a}^{\dagger\prime} = \hat{U}_{Dok}^\dagger \hat{a}^\dagger \hat{U}_{Dok}$. $P(\mathbf{m})$

is then known as the Franck-Condon factor for this transition. The vibronic spectrum VS as a function of frequency ω_{vib} of the molecule is given by the set of all of its Franck-Condon factors:

$$\text{VS}(\omega_{\text{vib}}) = \sum_{\mathbf{m}} P(\mathbf{m}) \delta \left(\omega_{\text{vib}} - \sum_k \omega'_k m_k \right) \quad (7.13)$$

where the summation over k is over all the modes.

7.1.2 Quantum optical simulation of vibronic spectroscopy

There is no known efficient classical algorithm for estimating the Franck-Condon factors in the vibronic spectra of molecules. However, it has recently been shown that the estimation of molecular vibronic spectra can in principle be done using a quantum optics simulator^[212,215]. This proposed experimental protocol is based on an analogy between vibronic spectra and quantum optics, which we explain in the following.

Analogy between vibronic spectra and quantum optics

Both the vibrational modes of a molecule in the harmonic approximation and modes of the electromagnetic field are described by quantum harmonic oscillators. An N mode vibrational state of a molecule can therefore in principle be simulated by an N mode optical state. Specifically, a Fock state of the vibrational modes of a molecule described by \mathbf{m} has a direct analogy in quantum optics as a state of an optical field with m_1 photons in mode 1, m_2 photons in mode 2, etc. Furthermore, the mode transformations described above have an analogy in quantum optics. The change of basis describing the vibrational modes of a molecule after an electronic transition occurring at 0 K can be mapped onto an op-

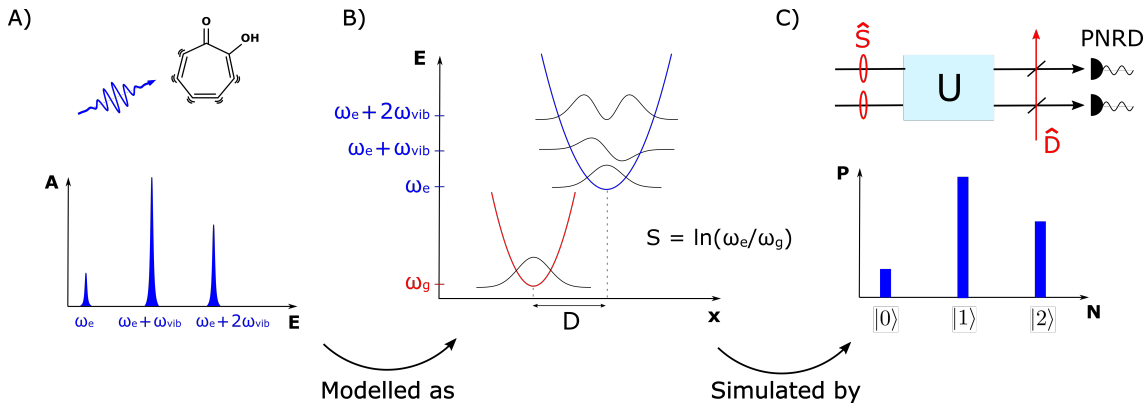


Figure 7.1: Overview of the scheme for estimating vibronic spectra. A) A vibronic transition in a molecule such as tropolone (pictured, top) consists of a joint electronic and vibrational excitation. Depending on the energy of the absorbed photon, different vibrational states are excited, leading to complex spectra (bottom). The heights of the peaks depend on the overlaps between the ground state of the molecule and the excited vibrational states of the excited molecule. B) We model vibronic transitions using a harmonic approximation of the vibrational modes. The harmonic oscillators describing the excited state (in blue) are squeezed by S and displaced by D with respect to the ground state (in red). The overlaps between the different Fock states determine the heights of the spectral peaks. C) We simulate this process using a quantum optics experiment with squeezing S and displacement D (top). Each optical mode is mapped onto a vibrational mode of the molecule; in our case we consider two coupled vibrational modes of tropolone. The probabilities of measuring photon number outcomes using photon number resolving detectors (PNRD) are mapped onto the heights of the peaks in the spectrum (bottom).

tical transformation that sends vacuum first into a set of single mode squeezing operations described by $\text{acosh}(A_D)$, then into a multiport interferometer implementing transformation U , and is finally displaced.

The Franck-Condon factors can be estimated using photon number resolving measurements on the resulting state. In vibronic spectroscopy, the Franck Condon factor $P(\mathbf{m})$ for a specific transition is equal to the overlap between the ground state and the excited state of the harmonic oscillators described by $|\mathbf{m}\rangle$ after the change of basis. For the optics experiment, the overlap between the optical state and photon number configuration $|\mathbf{m}\rangle$ after the optical transformations is equal to the probability of measuring outcome $|\mathbf{m}\rangle$ using photon number resolving detectors. The probability of measuring photon number configuration $|\mathbf{m}\rangle$ is therefore equal to $P(\mathbf{m})$. Multiple experimental trials can be used to estimate

the probabilities of all the measurement outcomes, and therefore determine $P(\mathbf{m})$ for every $|\mathbf{m}\rangle$, thus reconstructing the Franck-Condon profile of the molecule.

Scaling of this protocol

Since the size of the Hilbert space of the system increases exponentially with the number of modes whereas the speed at which samples are collected in principle takes constant time, it is worth discussing the scalability of this experimental protocol. As in boson sampling, we cannot expect to use the sampling procedure to efficiently calculate the probabilities of all the possible outcomes and all the corresponding Franck-Condon factors. However, in the vibronic spectra estimation protocol we are interested only in producing an estimate of the leading Franck-Condon factors, which correspond to the subset of the total Hilbert space with the highest probability of producing samples. The protocol is therefore tractable as long as a small number of Franck-Condon factors dominate all the others.

However, since even the number of relevant Franck-Condon factors can be expected to increase rapidly with the number of modes, the vibronic spectra estimation protocol becomes inefficient after a certain point. This does not make this protocol irrelevant. Even if it ultimately fails for very large systems, a quantum optics-based simulation may still be able to provide useful information about Franck-Condon spectra for systems that are too large for classical computers. Exactly for what type and size of molecule this advantage may exist is beyond the scope of this thesis; in the following we will focus on the applicability of the vibronic spectra estimation protocol in the face of imperfect experimental implementations.

Comparison to other quantum optics protocols

The proposed experimental protocol for estimating vibronic spectra is considerably simpler than other quantum simulation protocols that require particle interactions or even full quantum computing. All that is required is a linear optics setup involving relatively simple operations: squeezing, interference, displacement, and photon number measurements. Furthermore, in contrast to several linear optics protocols, no post-selection is required.

This experimental protocol is similar to boson sampling: quantum states are prepared in several modes, interfered, and then measured in the photon number basis. However, the original boson sampling protocol requires single photon inputs, random unitary matrices, and many more modes than photons. The protocol for estimating vibronic spectra uses squeezed state inputs, specific matrices corresponding to the structure of the molecules being simulated, and as many modes as squeezed states. As discussed in the introduction, the original hardness proof for boson sampling has been extended to the case of Gaussian state input. However, the use of specific as opposed to random matrices and the equal number of modes and squeezers implies that the hardness of the vibronic spectra protocol is still an open question.

State of the Art

Since the original proposal by Huh *et al*^[212] describing the simulation of vibronic spectra for molecules at 0 K, an extension of the theory has been proposed to address the simulation of molecules at different temperatures^[215]. This extension requires single photon inputs instead of vacuum and an additional interferometer before the squeezing operation.

Experimentally, vibronic spectra have been estimated using experimental platforms other

than linear optics. Any platform that makes use of quantum harmonic oscillators can indeed be used to simulate the change in vibrational modes. A system involving a superconducting qubit coupled to a cavity has thus been used to calculate simple vibronic spectra involving only displacements in a single mode^[216]. A single trapped ion with two radial degrees of freedom described as quantum harmonic oscillators has also been used to simulate the spectrum of sulphur dioxide^[217].

Recently, an integrated quantum optics experiment^[218] has used the analogy between optical modes and vibrational modes of molecules to simulate the time evolution of vibrational excitations in molecules, energy transport in molecules, and effects such as anharmonicities and thermal relaxation. However, this work stops short of investigating vibronic spectra and the effects of experimental error and imperfections on their simulations which may affect their scalability.

7.2 Dealing with imperfections

Any experimental implementation of a quantum algorithm on a platform that does not have a fault-tolerant architecture is necessarily degraded by imperfections in the system operations. This is a potential limitation to the performance of all specialised quantum processors. Quantum optics is a promising platform for implementing this quantum algorithm for simulating vibronic spectra due to the availability of good sources of squeezing^[219] and high-efficiency photon number resolving detectors, as well as the potential for manipulating a large number of optical modes^[220,221]. However, scattering and absorption losses, mode mismatches, detector noise and unanticipated correlations may all contribute to less than ideal operation. The presence of experimental imperfections in any platform was not

considered in the original proposal. These imperfections can be expected to affect the simulation, possibly reducing both the accuracy and precision of the results.

In the following, we study the impact of such imperfections and how to account for them in an experiment. We show in theory that imperfect experiments can still yield approximations of molecular vibronic spectra. First, we show that optimal experimental parameters can be efficiently determined for any experimental setup. Second, we show that the error on experimental estimates of vibronic spectra can be efficiently bounded. Third, we show that such experiments can outperform a classicality criterion.

7.2.1 Designing an experiment

In the absence of imperfections, equation 7.7 would be used to determine which squeezing parameter and beam splitter reflectivity to use in an experiment. With the above-mentioned imperfections, however, these experimental parameters will not yield the target optical state. In the following, we propose a method for determining, in a scalable way and in the presence of imperfections, experimental parameters that yield a state that is as close as possible to the target optical state.

We first note that the Gaussian state formalism discussed in the introduction can be applied here. The initial state (vacuum) and all the subsequent optical operations (squeezing, rotation, and displacement) are Gaussian before the photon number measurement. Furthermore, many sources of imperfection such as loss, mode mismatch, and dark counts on detectors can also be described using the Gaussian state formalism. We will therefore make use of the Gaussian state formalism and describe both the target optical state and the experimentally generated state using their covariance matrices and displacement vectors.

We require a metric to compare the experimentally generated state to the target state. We cannot directly compare the experimentally generated state to the target state in the photon number basis because there is no known efficient classical algorithm for calculating the photon number statistics of a general Gaussian state. However, the fidelity between two Gaussian states can be efficiently calculated using their covariance matrices and displacement vectors^[222–224]. We therefore use the fidelity as our metric.

We now consider the problem of designing an experiment in order to maximise the fidelity to a target state. Typically, an experimental setup has a certain number of experimental parameters that can be controlled, such as the pump power determining the squeezing and the interference between the modes, and a certain number of parameters that cannot be controlled such as the loss and the detector dark counts. The task of producing the state with the highest fidelity to the target state can be formulated as an optimisation problem over the controllable parameters given the presence of the uncontrollable parameters. To efficiently optimise the fidelity, an accurate description of the experimentally generated state must first be formulated as a function of all the experimental parameters, using a number of steps at most polynomial in the number of modes. First, the squeezers can all be characterised independently, as can the detectors. If the interference is provided by a universal multiport interferometer, then the characterisation steps described in the previous chapters can be used. Losses at the input and output of the interferometer can be individually characterised using classical light. Mode overlaps can be determined using their pair-wise Hong-Ou-Mandel dip visibility. The experimentally generated state can therefore in principle be accurately described for any combination of experimental parameters.

Finally, the numerical optimisation procedure itself must be efficient. Since the fidelity

can be expected to be a nonlinear function of all the experimental parameters, the optimisation procedure is not straightforward so this condition cannot in general be satisfied. However, numerical optimisation can be used to at least find a local optimum in parameter space, which depending on the desired accuracy of the simulation may be suitable.

7.2.2 Bounding the error

In the presence of experimental imperfections, we can in general expect that even if a global optimum for the fidelity is found then this optimum will in general still not be unity. This is because imperfections such as loss degrade the purity of an optical state, whereas the target state is a pure state. We can therefore expect the resulting estimate of the vibronic spectra to contain some degree of error. For our experimental results to yield a useful approximation of vibronic spectra, we require a method for bounding this error. The fidelity can be used to provide such a bound.

The fidelity F between two states described by density matrices ρ_1 and ρ_2 is related to the trace distance D by^[4]:

$$D(\rho_1, \rho_2) \leq \sqrt{1 - F(\rho_1, \rho_2)^2} \quad (7.14)$$

D is related to the maximum classical l_1 distance between different possible measurement outcomes by:

$$D(\rho_1, \rho_2) = \max_{\{E_m\}} D(p_m, q_m) \quad (7.15)$$

where the maximisation is over all sets of detector positive-operator valued measures (POVMs)

$\{E_m\}$ at the output of the network, and $p_m = \text{tr}(\rho_1 E_m)$ and $q_m = \text{tr}(\rho_2 E_m)$. If we consider the POVMs projecting onto photon numbers, we then have that:

$$\|P_1 - P_2\| \leq \sqrt{1 - F(\rho_1, \rho_2)^2} \quad (7.16)$$

where P_1 and P_2 correspond to the photon number statistics associated with states ρ_1 and ρ_2 .

Equation 7.16 now gives us an efficiently calculable measure for determining how close experimental photon number statistics are to those of the ideal state. If ρ_1 is the density matrix corresponding to the experimentally generated state and ρ_2 is that of the ideal state, we can use this inequality to bound the error on an experimental estimate of Franck-Condon factors.

In addition to the error bound calculated in this way, we can also account both for the statistical error in estimating the Franck-Condon factors due to the finite number of experimental samples and for small deviations from a Gaussian model of an experiment. If we assume that the statistical error can be bounded by ϵ_{stat} and the error caused by deviations from a Gaussian model of an experiment can be bounded by $\epsilon_{\text{nonGauss}}$, then the distance between the estimated photon number statistics P_{exp} derived from the set of measurement results and the Franck-Condon factors P can be straightforwardly bounded by:

$$\|P_{\text{exp}} - P\| \leq \sqrt{1 - F(\rho_{\text{exp}}, \rho_{\text{ideal}})^2} + \epsilon_{\text{stat}} + \epsilon_{\text{nonGauss}} \quad (7.17)$$

where ρ_{exp} corresponds to the Gaussian description of the experimentally generated state

and ρ_{ideal} is the density matrix of the target state.

7.2.3 Classicality criterion

Quantum optical experiments aiming to estimate vibronic spectra are worthwhile if they outperform known classical algorithms. Although the idealised original proposal by Huh *et al* does outperform known classical algorithms when the Franck-Condon factors are localised in the Hilbert space describing the optical state, it is not a priori clear that an imperfect experiment also does so. For example, it is known in the case of boson sampling that imperfections such as loss and photon distinguishability can make an experiment efficiently classically simulable^[68,69]. Furthermore, while there is no known efficient exact classical algorithm for calculating vibronic spectra, some classical approximation strategies do exist. One case-by-case strategy involves guessing which transitions are likely to contribute the most to the spectrum and only calculating the corresponding Franck-Condon factors^[225]. A quantum optics experiment with imperfections will only be worthwhile if such other approximation strategies yield worse estimates of vibronic spectra than the experiment.

We propose the following efficient classical approximation algorithm as a minimum benchmark that experiments must outperform in order to produce better than classical estimates of vibronic spectra. This algorithm is conceptually similar to the quantum simulation protocol, so that the same analysis tools can be used in both cases.

We start by finding the classical optical state, defined as having a regular P-function in phase space^[17], that maximises the fidelity to the target state within the space of all optical states. First, we note that the displacement operation that occurs in the state preparation process can in principle occur before the interferometer instead of after, so

that the vibronic spectroscopy experiment consists of squeezed and displaced states sent into an interferometer. The fidelity being invariant under unitary transformations such as multimode interference, finding the closest classical state to the ideal target state is equivalent to finding the closest classical state to these initial displaced squeezed states. The closest single mode classical state to a single mode displaced Gaussian state is known to be a coherent state with the same displacement^[226]. Therefore, the closest multimode classical state to the target state is a multimode coherent state with the same displacement.

Next, we simulate sampling from the photon number statistics of this state. Since this state is classical, its photon number statistics can efficiently be sampled from using a classical algorithm^[31]. Since this state is also Gaussian, equation 7.16 can be used to estimate the target vibronic spectrum to within some error bound. To outperform this classical algorithm, a quantum experiment must yield an error bound given by equation 7.17 that is smaller than that yielded by the classical state.

This classical approximation strategy can also be used as a classicality witness for the optical state: any experimental state with a higher fidelity must have a non-regular P-function. We therefore use this best classical state as our minimum criterion for demonstrating a quantum advantage in experiment. Any experimental optical state that beats the witness is both a non-classical state and produces a better approximation of vibronic spectra than would be possible with any classical state. Furthermore, we note that if an experimentally generated state beats our classicality criterion, then currently known efficient classical simulation algorithms based on the phase space description of the state are generally not applicable^[31,227].

7.3 Experiments

To provide a concrete example for our study of the impact of imperfections in an experiment, and to demonstrate our method for estimating spectra in the presence of imperfections, we realise a proof of principle experiment. We use the example of tropolone ($C_7H_6O_2$), which is a molecule contributing to the taste and colour of black tea^[228] (see Fig. 7.1).

We choose tropolone to illustrate our findings for the following reasons. First, the vibronic transition that we study does not include a displacement, which is otherwise present in many other molecules. Displacements can be implemented in quantum optics using classical laser light, and do not affect whether an optical state is classical, as defined by having a regular P-function in phase space^[17], or not. Furthermore, the squeezing parameters for the two modes in the ideal experiment are quite large compared to most other molecules. The absence of displacement and these large squeezing parameters allow us to focus our analysis on the quantum mechanical aspects of the experiment. These factors also allow us to highlight the impact of imperfections such as loss, which squeezing is strongly affected by, on an experiment.

7.3.1 Application to tropolone

In the 370 nm electronic transition in tropolone, the change in molecular configuration caused by the electronic excitation distorts the vibrational modes and couples them to each other. In the following, we focus on a subset of two of these modes which couple only to each other^[229]. The change in mass-weighted normal coordinates (Q_1, Q_2) of the two modes

under study is^[210,229]:

$$\begin{pmatrix} Q'_1 \\ Q'_2 \end{pmatrix} = \begin{pmatrix} 0.9 & 0.436 \\ -0.436 & 0.9 \end{pmatrix} \begin{pmatrix} Q_1 \\ Q_2 \end{pmatrix} \quad (7.18)$$

Our experiment aims to determine the Franck-Condon factors that are associated with this transformation. If the initial vibrational state is the ground state and the final state has m_1 energy quanta in mode 1 and m_2 energy quanta in mode 2, then:

$$P(m_1, m_2) = \left| \langle m_1, m_2 | \hat{U}_{Dok} | 0, 0 \rangle \right|^2 \quad (7.19)$$

is the Franck-Condon factor of the transition at frequency $m_1\omega_1 + m_2\omega_2$, where $\omega_1 = 176 \text{ cm}^{-1}$ and $\omega_2 = 110 \text{ cm}^{-1}$ are the excited state vibrational frequencies of modes 1 and 2.

We now consider the quantum optics analogy to the vibrational transition described above. According to our earlier discussion, the transformation described by equation 7.18 can be achieved in quantum optics via two single-mode squeezing operations and a beam splitter. Inserting the Duschinsky rotation and the frequencies for the ground and excited states of the molecules into equation 7.7, we get the parameters shown in table 7.1 for producing the ideal state.

Tropolone	
Squeezing parameter 1	0.190
Squeezing parameter 2	0.720
Beam splitter transmittivity	0.10

Table 7.1: Experimental parameters for generating the ideal optical state to simulate tropolone.

These parameters allow us to describe the state at any step in this state generation

process using its covariance matrix and displacement vector^[34,230], and also to determine the corresponding exact photon number statistics (albeit with exponential overhead in the number of modes)^[33]. $P(m_1, m_2)$ is now the probability of detecting m_1 photons in mode 1 and m_2 photons in mode 2. An ideal quantum optics experiment that prepares two appropriate single mode squeezed vacuums (SMSV), interferes them on a beam splitter with the appropriate reflectivity, and measures the resulting photon number distribution using photon-number resolving detectors can therefore be used to estimate the Franck-Condon factors associated with the 370 nm transition in tropolone.

7.3.2 Experimental Setup

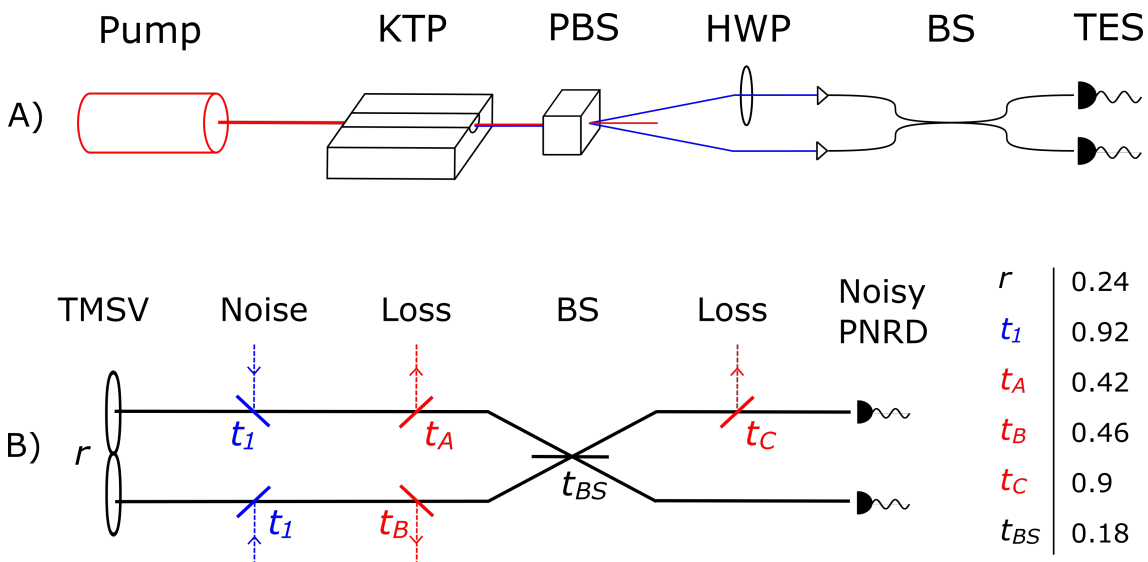


Figure 7.2: A) We approximate the Franck-Condon factors of tropolone experimentally by sending pump pulses at 780 nm into a periodically poled KTP waveguide, separating the two orthogonally polarised downconverted modes at 1560 nm using a polarising beam splitter (PBS), and rotating the polarisation of one of the two modes using a half wave plate (HWP). We then couple these two modes into polarisation-maintaining (PM) fibre, interfere them in a tunable PM beam splitter (BS), and measure them using two fibre-coupled transition-edge sensors (TES). B) We model this experiment as a two mode squeezed vacuum (TMSV) interfered on a beam splitter and measured by noisy photon number resolving detectors (PNRD), in the presence of loss and noise produced by the non-overlapping parts of the two modes. The squeezing parameter r of the TMSV and the transmissions of the beam splitters in our model of the experiment are shown in the table on the right.

Our setup (Fig. 7.2A) consists of squeezed light sources, an interferometer implemented by a variable polarisation-maintaining (PM) fibre beam splitter, and photon number resolving detectors.

Our photon source consists of a 8 mm long periodically poled potassium titanyl phosphate (KTP) crystal^[231], pumped with a mode-locked titanium-sapphire laser the output of which is stretched, picked off and amplified in a regenerative amplifier, and compressed. The resulting pulses have a centre wavelength of about 780 nm, a bandwidth of about 2-4 nm, and occur at a repetition rate of 100 kHz. After the KTP crystal, the pump light is filtered out. The output horizontal and vertical polarisation modes have a centre wavelength at about 1560 nm. The optical state in these modes is typically described as a two mode squeezed vacuum (TMSV). These modes are spatially separated using a Wollaston prism and individually filtered using 3 nm bandpass filters to remove any excess noise at the wrong wavelengths. The two modes are then coupled into (PM) fibre at the two inputs of our variable fibre beam splitter. The two outputs are monitored by photon-number resolving transition-edge sensors (TES) described in the chapter on photon detectors.

Our setup suffers from several imperfections. Firstly, we approximate the two independent SMSVs that are required in an ideal setup using a two mode squeezed vacuum, since TMSVs are experimentally simpler to generate and mode-match. The TMSV can be converted into two identical SMSVs using the beam splitter in our setup. Furthermore, as we show in the following section, the two modes are not exactly identical, the 60% loss in our setup is significant, and our detectors have a small but finite amount of noise.

7.3.3 Characterising the experimental setup

To produce an optical state that maximises the fidelity to the target state in the presence of imperfections, we first characterise the experimental setup in order to realise a model for the experiment within the Gaussian state formalism. In this section, we explain how this characterisation and modelling is performed. Figure 7.2 shows the model that we use as a result of this characterisation process.

Detectors

We model the TESs as photon number-resolving detectors that, despite having a very low intrinsic dark count rate, suffer from the following noise mechanisms.

Firstly, the binning procedure that we use to extract photon numbers from the analogue output signal is susceptible to noise on our detectors. With a vacuum input, we experimentally find that there still is a 0.2% probability of wrongly registering a one photon event. We approximate this noise as a dark count mechanism, which can be accounted for within a Gaussian model by considering that our detector is sensitive to both a noiseless input signal and to an additional mode containing a thermal state with a 0.2% single photon component.

Secondly, some pump photons leak through our setup and make it to the detectors. Since TESs resolve the energy of incoming photons, these pump photons are counted as two-photon events. We find that our TESs have a 0.1% probability of detecting these pump photons. This noise mechanism can be included within our model by considering that our detector is sensitive to an additional pump mode containing a weak coherent state with a 0.1% single photon component. This noise can be included in our estimate of the fidelity. Both additional noise modes have a fidelity of about 0.998 to vacuum, and since the fidelity

for a product state is the product of the fidelities, the total fidelity of these noise modes to vacuum is 0.9958. This fidelity must then be multiplied by the estimated fidelity of the optical state before the detectors in order to determine the total fidelity.

Our TESs also have some degree of inefficiency. This inefficiency is accounted for in our estimate of the total system efficiency described in the following paragraph.

Squeezing and loss

We characterise the total loss (including detector inefficiency) and squeezing in our system using a tomography technique similar to that described in^[232], which proceeds as follows. We model our photon source as a perfect TMSV with additional loss in the two modes and use our model for the detectors described above. We then numerically find the squeezing parameter and the distribution of the loss in both arms which yield the photon number statistics that most closely match the experimental photon number statistics. We follow this procedure for the beam splitter set first to 100:0, and then to 0:100, in order to determine how the losses in the system are distributed in both modes both before and after the beam splitter. We note that since balanced losses can mathematically be commuted through the beam splitter, we need to consider losses in only one of the output ports of the beam splitter in our model.

To verify that our estimate of the losses is reliable, we perform this tomographic procedure for one of the two beam splitter settings for several different pump powers ranging from 10 μW to 300 μW . We find that at powers exceeding 100 μW our results are skewed as higher order nonlinearities such as self-phase modulation start affecting the pump and the downconverted modes^[233]. We therefore use the values for the loss that are found in

the low power region in Fig. 7.3, and experimentally estimate the error on these values to be $\pm 2\%$. These values are also consistent with the heralding efficiencies estimated from the photon number statistics in this plateau region.

The tomography procedure yields the squeezing parameter that we can directly use in our Gaussian model. The squeezing parameter r is related to the pump power P in the single mode approximation by the following relation:

$$P \propto r^2 \quad (7.20)$$

Once the squeezing parameter has been determined for one power, we can use equation 7.20 to determine the squeezing for any power. To estimate the error on our estimate of the squeezing parameter, we fit the squeezing parameters determined from our optimisation procedure to a curve given by equation 7.20 in the plateau region. This fit is shown in Fig. 7.3. We experimentally estimate the error on our estimate of the value of the squeezing parameter at low powers to be 0.01.

We can also use our tomography results to estimate the error stemming from our Gaussian approximation of the experiment. Fig 7.3 shows the deviation, quantified by l_1 distance, between the measured photon number statistics and those of the closest lossy TMSV measured with noisy detectors determined by our tomography technique. At low powers, we find that this error is less than 10^{-3} , so we consider that our description of the optical state and of our detectors is satisfactory.

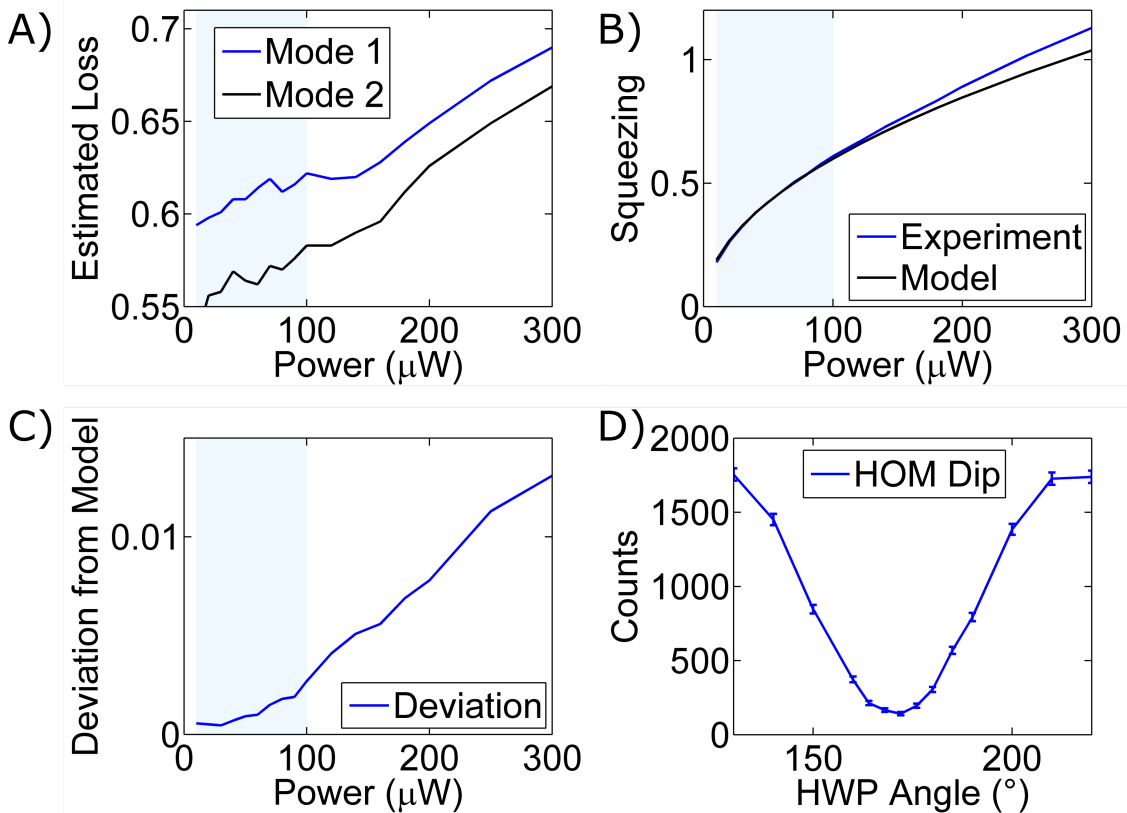


Figure 7.3: Characterisation data for our experiment. A) Total losses for the two modes in our setup, estimated from our tomography procedure for different pump powers, with the beam splitter set to full transmission. We use the average and the standard deviation of the values in the shaded area for our estimate of the experimental parameters. B) Squeezing parameter, estimated from our tomography procedure, as a function of pump power. Within the shaded area, we find that the relation between squeezing parameter and pump power is very close to the theoretical relation $P \propto r^2$. C) Deviation between our experimental photon number statistics and the theoretical photon number statistics given by our model for the optical state, quantified by the l_1 distance. D) Coincidence counts on our detectors measured as a function of the angle of the half wave plate (HWP) in our setup. We observe non-classical Hong-Ou-Mandel interference^[38].

Distinguishability

We characterise the distinguishability δ between the optical modes by using the depth of the Hong-Ou-Mandel interference^[38], shown in Fig. 7.3, measured by setting the beam splitter to 50:50 and measuring the number of coincidence counts at the outputs as we rotate the HWP in our experimental setup. We use SNSPDs as our photon detectors for this procedure due to their greater ease of operation. Considering that non-overlapping parts of the two modes can be modelled as noise photons, the ratio of noise photons to signal photons in the system is then δ . We choose to model this noise as virtual beam splitters of reflectivity δ , placed just after the squeezing operation for both modes, between each mode and a virtual thermal state containing the same average number of photons as the TMSV. The $\pm 2\%$ error on our estimate of δ comes from the error on the estimate of the depth of the measured Hong-Ou-Mandel dip. We note that our model for the noise given by the distinguishability is only an approximation of the full description of this noise, which would require taking several additional non-interfering modes into account. However, our model provides a rough estimate of the contribution of this noise towards the degradation of the fidelity.

Beam splitter reflectivity

The beam splitter reflectivity was set by blocking one mode in our experiment, setting the beam splitter to be fully transmissive so that the maximum photon number at the detector for that mode could be determined for a given pump power, and then adjusting the beam splitter until the average photon number at the detector was the desired fraction of the maximum. The error on our estimate of the reflectivity was experimentally estimated to be $\pm 1\%$.

7.3.4 Results for tropolone

Finding the optimal state

The characterisation procedure described previously yields a Gaussian model for the experiment. For any value of the beam splitter reflectivity and squeezing parameter, we now have a Gaussian description of the output state that accounts for the imperfections in the setup.

To find the values of the squeezing parameter r and beam splitter reflectivity t_{BS} that maximise the fidelity of the experimentally generated state to the target state, we use Matlab's built-in fminsearch procedure. In this simple problem in which the fidelity can be expected to be a convex function of only two parameters, this routine finds the global optimum for the fidelity. Fig. 7.2B shows the values of r and t_{BS} that maximise the fidelity within our model. This maximum theoretical fidelity is 0.891.

Given the errors in our model, we expect not to achieve this maximum fidelity in practice. To obtain a more reasonable estimate of the fidelity, we use a Monte Carlo method to determine the most likely value of the fidelity that we achieve as well as the error on this value. We simulate 100 states produced by our experiment, where we randomly select the experimental parameters from a Gaussian probability distribution determined by the estimated mean and standard deviations given by our analysis. The mean and standard deviation in the fidelity of these samples are used as our fidelity estimate and as the error on this estimate. With this method, we revise our estimate of the fidelity to the target state to be 0.890(1).

Estimated Franck-Condon factors

We collected 1638370 samples over the course of about 20 seconds from the photon number statistics of our state from which we estimate the Franck-Condon factors of the transition under study. Table 7.2 compares our experimental estimate to the exact theoretical target values numerically calculated using equations 7.18 and 7.12. By comparing our experimental values to the exact values, we find a difference of 0.206 with a statistical error smaller than 10^{-3} . This difference is significant; the following section will provide a detailed analysis of the sources of error.

Frequency	Experiment	Ideal
0	0.9628	0.7731
ω_1	0.0129	0
ω_2	0.0127	0
$2\omega_1$	0.0035	0.1097
$2\omega_2$	0.0038	0.0041
$\omega_1 + \omega_2$	0.0035	0.0469
$4\omega_1$	$< 10^{-4}$	0.0233
$3\omega_1 + \omega_2$	$< 10^{-4}$	0.0200

Table 7.2: Most significant Franck-Condon factors estimated by our experiment and by simulations for an ideal experiment.

Error Analysis and classicality

We apply equation 7.17 to our experiment to determine the theoretical error bound using our analysis of the fidelity, the statistical error and the observed deviation from Gaussian behaviour in our system. We find a bound for the trace distance of 0.455. Our experimental results are therefore indeed within this bound.

We also apply our classicality criterion to this experiment. The classical state with the highest fidelity to the target state is vacuum, since there is no displacement and any amount of squeezing contributes to non-classicality. Vacuum has a fidelity of 0.879 to the target

state. Our experiment has a higher fidelity by about 10 standard deviations and therefore satisfies our classicality criterion. Using vacuum, the classical approximation algorithm described above would yield an error bound of 0.476, which is worse than what we achieved in experiment. However, we note that in the specific case where the closest classical state is vacuum the total difference in photon number statistics between the target optical state and the closest classical state can be efficiently calculated, as opposed to simply bounded using the fidelity. This calculation is efficient because the exact probability of measuring a vacuum outcome for any Gaussian state can be calculated efficiently, due to vacuum also being a Gaussian state.

7.3.5 Results for benzene

To highlight the fact that experimental imperfections can in some cases eliminate any advantage to performing a quantum optical simulation, we also simulate the $S_0(^1A_{1g}) \rightarrow S_1(^1B_{2u})$ transition in benzene^[234]. A simulation of this transition requires less squeezing than tropolone. We once again only consider two modes involved in this transition that do not couple to any of the other modes, and for which there is no displacement term.

For this transition, the Duschinsky rotations and the frequencies of the initial and final electronic states (in cm^{-1}) are:

$$U = \begin{bmatrix} 0.652 & 0.758 \\ 0.758 & -0.652 \end{bmatrix} \quad (7.21)$$

$$\omega_i = [1332, 1169] \quad (7.22)$$

$$\omega_f = [1854, 1254] \quad (7.23)$$

Benzene, Ideal Experiment	
Squeezing 1	0.0076
Squeezing 2	0.208
Beam splitter transmittivity	0.02

Table 7.3: Experimental parameters for generating the ideal optical state to simulate benzene.

Benzene, Imperfect Experiment	
Beam splitter transmittivity	34%
Squeezing	0.06
Fidelity	0.9861(1)

Table 7.4: Experimental parameters used to simulate benzene.

Following the same method as for tropolone, we get the parameters shown in table 7.3 for producing the corresponding ideal optical state. To experimentally simulate benzene, we follow the procedure described above and find the values of the fidelity and optimal parameters shown in table 7.4, given the experimental parameters and the model shown in Fig. 7.2. We note that the amount of squeezing required is significantly less than for our simulation of tropolone.

Our experimental results for the Franck-Condon factors of the transition under study in benzene are shown in table 7.5. With our estimate of the fidelity for benzene and our estimate for the deviation of our state from a TMSV in photon number statistics, we can bound the error on the l_1 distance of our Franck-Condon factors to the actual Franck-Condon factors to 0.1663 using equation 7.17. By comparing our experimental results to those that would be yielded by the ideal target state, we find an actual error of 0.0198, which is well within the bound.

We compare our results for benzene to those yielded by the classical approximation procedure discussed in the main text. Vacuum has a fidelity of 0.9893 to the ideal state. We note that this is higher than the fidelity of 0.9861 for our experimental state; the weakness

Frequency	Experiment	Theory
0	0.9925	0.9787
ω_1	0.0027	0
ω_2	0.0022	0
$2\omega_1$	0.0012	0.0196
$2\omega_2$	0.0009	$< 10^{-4}$
$\omega_1 + \omega_2$	0.0002	0.0010
$4\omega_1$	$< 10^{-4}$	0.0006

Table 7.5: Most significant experimental and theoretical Franck-Condon factors for the transition under study in Benzene.

of the squeezing when compared to the experimental imperfections therefore causes our experiment to perform less well than our efficient classical estimation technique. The error bound using the fidelity for the classical state and equation 3 from the main text is 0.1459, which is smaller than the 0.1663 bound for our experimental state. The actual error in the corresponding estimation of the Franck-Condon factors for benzene is 0.0213 for the classical simulation, which is close to the 0.0198 error that we achieved experimentally.

7.4 Discussion

In this section, we discuss our experimental results, and in particular we analyse the main ways in which different experimental imperfections contribute to the degradation of the fidelity. We also apply the theoretical tools developed above to analyse the performance of quantum optics experiments for the simulation of other molecules.

7.4.1 Analysis of the simulation of tropolone

Figure 7.4 shows the effect of different sources of imperfection on the fidelity in our experimental setup. An ideal experiment consists of SMSVs and ideal detectors (black solid line). The additional dashed and dotted lines indicate the effect of additional imperfections

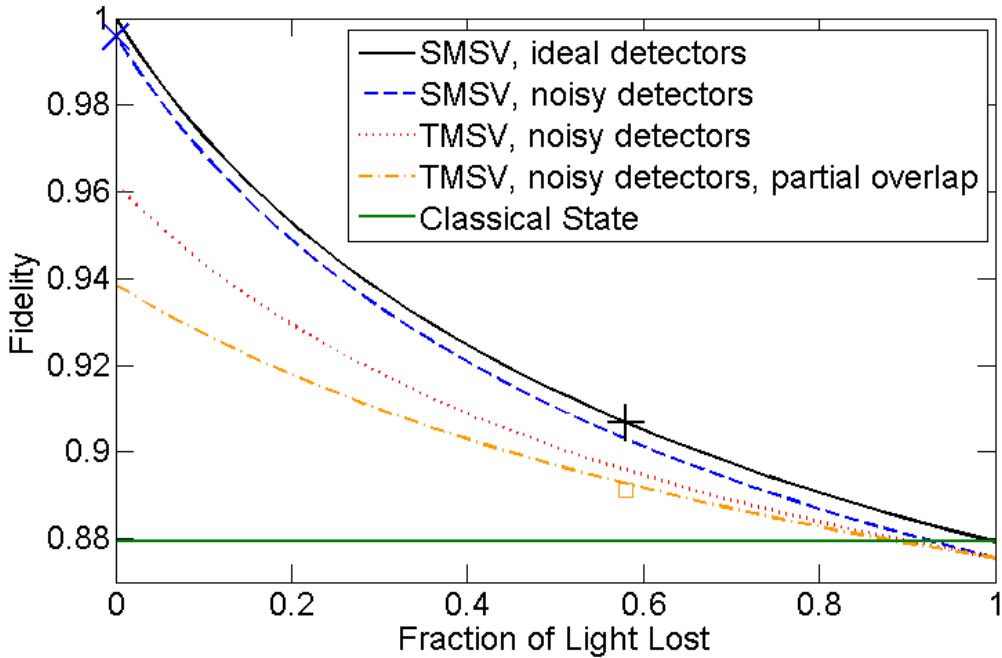


Figure 7.4: Maximum achievable fidelity as a function of the fraction of light lost in a simulation of tropolone, for different imperfections in an experimental setup. We simulate an ideal setup that is only affected by loss (black solid line), to which we add our noisy detectors (blue dashed line), then replace the SMSVs by a TMSV (red dotted line), then add our measured partial overlap between the modes (orange dashed-dotted line). The + and X signs (the X is located on the y axis) respectively indicate the best SMSV for our level of loss and the best SMSV without loss but with noisy detectors, yielding the estimated Franck-Condon factors shown in Table 7.6. The orange square indicates the experimental parameters used for our experiment. For this analysis, we assume equal loss in both modes, hence the discrepancy between the orange square and the position of the orange dashed-dotted line.

that must be accounted for in our experiment. The orange dashed and dotted line indicates the effect of all the parameters that we account for in our analysis, and the orange square corresponds to our experiment. The flat green solid line indicates the maximum fidelity that can be achieved with the best classical state. These theoretical curves can easily be derived using our Gaussian model for the experiment.

We see that our classicality criterion is relatively tolerant of experimental imperfections to simulate transitions that involve large amounts of squeezing. An enhancement over the best classical state can be achieved with values of loss up to 90%, with noisy detectors,

and with the use of a TMSV instead of two SMSVs. For loss exceeding 90%, the noise on our detectors degrades the fidelity below that of the best classical state. For transitions in other molecules that involve less squeezing, such as the $S_0(^1A_{1g}) \rightarrow S_1(^1B_{2u})$ transition in benzene or the $\text{SO}_2^- \rightarrow \text{SO}_2$ transition discussed later, we find that our level of detector noise prevents us from outperforming this criterion for any level of loss.

Frequency	Experiment	Ideal	Lossy SMSVs	Best SMSVs
0	0.9628	0.7731	0.9327	0.7631
ω_1	0.0129	0	0.0377	0.0015
ω_2	0.0127	0	0.0073	0.0015
$2\omega_1$	0.0035	0.1097	0.0136	0.1102
$2\omega_2$	0.0038	0.0041	0.0004	0.0046
$\omega_1 + \omega_2$	0.0035	0.0469	0.0053	0.0466
$4\omega_1$	$< 10^{-4}$	0.0233	0.0004	0.0234
$3\omega_1 + \omega_2$	$< 10^{-4}$	0.0200	0.0003	0.0199
Fidelity	0.890(1)	1	0.9068	0.9958
Error	0.206	0	0.195	0.005

Table 7.6: Most significant Franck-Condon factors, fidelities, and errors estimated by our experiment, and by simulations for an ideal experiment, the best SMSVs for our level of loss, and the best SMSV in a lossless experiment but with noisy detectors.

A comparison of our experimental results and of the ideal theoretical results for a perfect experiment to simulations of other intermediate states is shown in Table 7.6. The loss leads to an overestimate of the Franck-Condon factor corresponding to vacuum, both for our experiment and for a theoretical lossy SMSV. Furthermore, whereas the Franck-Condon factors for odd numbers of excitations should be 0 due to the difference in symmetry between the ground state and the odd-numbered excited states, our experiment finds these to be non-zero due to photons which would correspond to higher order Franck-Condon factors being lost. The use of a TMSV instead of two independent SMSVs causes us to experimentally find photon numbers that are roughly symmetric in both modes, to within the imbalance in the loss in the two arms. We see from our results that, in the case of tropolone, although

the high squeezing and absence of displacement has allowed us to highlight the issue of imperfections in an experiment, by the same token our simulations result in a large error in estimating Franck-Condon factors.

7.4.2 Sulfur dioxide

We theoretically analyse the use of a quantum optics experiment to simulate the vibronic spectrum of the $\text{SO}_2^- \rightarrow \text{SO}_2$ transition, which was simulated using trapped ions^[217]. This transition provides an interesting comparison to that which we studied in tropolone. As opposed to tropolone, the $\text{SO}_2^- \rightarrow \text{SO}_2$ transition requires less squeezing and some amount of displacement, so that the resulting Franck-Condon factors arise mostly from the displacement term. Squeezing is vulnerable to loss whereas displacement is not, since if the loss in an experimental setup is known then the displacement can be adjusted to exactly compensate for it. We expect that such molecules can therefore be simulated with quantum optics with a much higher fidelity.

The Duschinsky transformation between the two normal modes of this molecule is as follows^[235]:

$$\begin{pmatrix} Q'_1 \\ Q'_2 \end{pmatrix} = \begin{pmatrix} 0.9979 & 0.646 \\ -0.646 & 0.9979 \end{pmatrix} \begin{pmatrix} Q_1 \\ Q_2 \end{pmatrix} + \begin{pmatrix} -0.3185 \\ 0.1160 \end{pmatrix} \quad (7.24)$$

The ground and excited state frequencies are (in cm^{-1}):

$$\omega_i = [990, 451]$$

$$\omega_f = [1178, 519]$$

SO₂	
Squeezing 1	0.051
Squeezing 2	0.107
Displacement 1	-1.33
Displacement 2	0.32
Beam splitter transmittivity	0.32

Table 7.7: Experimental parameters required to produce the ideal state to simulate sulfur dioxide

SO₂	
Squeezing	0.043
Displacement 1	-1.33
Displacement 2	0.32
Beam splitter transmittivity	0.97

Table 7.8: Experimental parameters required to produce the best state to simulate sulfur dioxide in the presence of imperfections.

The ideal optical state to simulate this transition, with the displacement occurring after the squeezing and beam splitter operations, is produced with the experimental parameters shown in table 7.7.

These low squeezing parameters compared to the displacement cause the Franck-Condon factors to be dominated by the displacement term. This fact is reflected in the fidelity of the closest classical state to this ideal optical state, which is 0.9965. This classical state is the coherent state with the same displacement as the ideal state.

As discussed in part 1, displacements can be induced using classical laser light and a beam splitter and can be adjusted to account for the loss. An experimental setup that implements these displacements and otherwise contains the same imperfections as our setup (in terms of loss, detector noise, imperfect overlaps between the modes and the use of a TSMV instead of an SMSV) would require the parameters shown in table 7.8 to maximise the fidelity to the target state:

The fidelity of the resulting experimental state to the target state would be 0.993, leading

to an error bound in the estimate of the vibronic spectrum following equation 3 in the main text of 0.118. We note that this fidelity is smaller than that of the closest classical state; since the required squeezing is quite low, noisy detectors are enough to degrade the fidelity of the experimental state below that of the closest classical state.

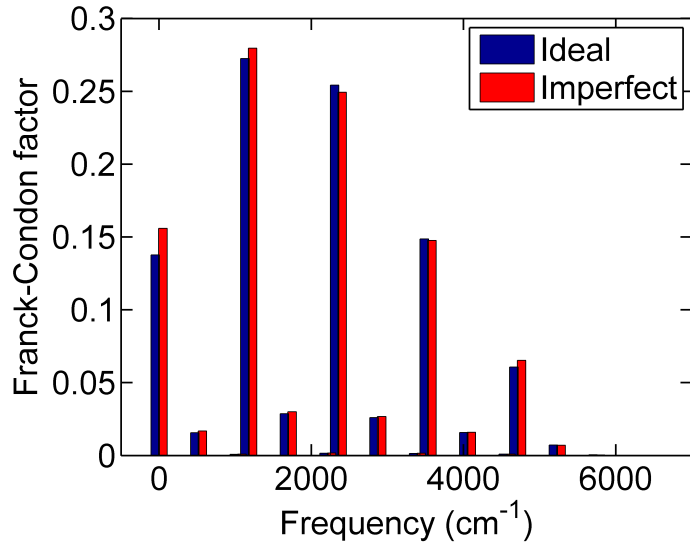


Figure 7.5: Expected vibronic spectrum of the $\text{SO}_2^- \rightarrow \text{SO}_2$ transition yielded by (blue) an ideal experimental setup and (red) an experimental setup perfectly implementing displacements and affected by the same imperfections as our experimental setup.

We can calculate the expected vibronic spectrum yielded from performing this experiment and compare it to that produced by the ideal optical state. This comparison is shown in figure 7.5. There is good qualitative agreement between the expected experimental results and theory, with a total $l1$ distance between the corresponding probability distributions of 0.0394.

This simulation of the $\text{SO}_2^- \rightarrow \text{SO}_2$ transition highlights the different roles played by displacement and by squeezing. This transition is dominated by the displacement term. A quantum optical experiment can in principle accurately implement displacements even in the presence of loss, which is why there is good qualitative agreement between the predicted

results and the ideal case. Squeezing plays only a marginal role in this transition, so that outperforming the closest classical state requires an experimental setup with a very small amount of imperfections.

7.4.3 Nonclassicality Analysis

Here, we analytically study the effects of loss and mode distinguishability on the classicality of the state that we sample from in the simulation of tropolone, defined by the regularity of its P function. We assume balanced loss in our setup and no detector noise for this analysis.

In order for the P function to be regular, the covariance matrix \mathbf{V}_{out} of the output state must satisfy^[236,237]:

$$\mathbf{V}_{out} - \frac{1}{2}\mathbf{I}_4 \geq 0, \quad (7.25)$$

where \mathbf{I}_4 is the 4×4 identity matrix. Since all the optical transformations in our model are Gaussian, \mathbf{V}_{out} can be readily obtained from the symplectic transformations^[230] corresponding to squeezing with squeezing parameter r and the virtual beam splitters with transmittivities $t_A = t_B = t_{AB}$, t_D and $1 - \delta$ which describe the photon losses in both modes, detector inefficiency, and the noise photons which are related to the distinguishability in our model, respectively. It can be shown that condition (7.25) is equivalent to the following expression:

$$t_{AB}t_D \left(\sinh(r)^2 - \sinh(r) \cosh(r)(1 - \delta) \right) \geq 0 \quad (7.26)$$

Inequality (7.26) is a sufficient condition for the P function of the state to be regular. Inequality (7.26) indicates that the main source of classicality in our experiment is the

distinguishability of the input optical modes. The expression in the parentheses gives a lower value for the distinguishability δ that renders the output state classical, i.e. $0.76 \lesssim \delta$ for $r \approx 0.25$.

Interestingly, this lower value decreases when the squeezing r increases, which means that the output state becomes classical in our model at squeezing $r \geq 1.1$ (and $\delta \approx 0.2$). This is due to the noise photons produced by our model for the distinguishability. Larger values of r yield higher numbers of these noise photons, which washes out the non-classicality caused by the squeezing. Moreover, we see that photon losses and detector inefficiencies contribute equally to the classicality of our experiment, when $t_{AB}t_D$ goes to zero.

7.5 Conclusion

In this chapter, we studied the experimental feasibility of a theoretical proposal for using a simple linear optics scheme to simulate vibronic spectroscopy. We found that this proposal can be adapted to account for inevitable experimental imperfections, and demonstrated a proof of principle experiment that illustrated our findings. We anticipate that our method of accounting for imperfections will be useful for designing future experiments.

Gaussian Optical Ising Machines

While research into quantum computers aims to transcend classical computation, within the framework of classical computation there also is a lot of research into developing new methods. Although conventional computers can in principle be used to solve any classically computable problem, there are many problems for which these computers are inefficient and for which alternative computation methods are desirable. Examples of such classes of problems include combinatorial optimisation, such as the travelling salesman problem, and some implementations of machine learning algorithms such as neural networks. For solving these problems, the use of special-purpose hardware that can provide practical advantages over conventional computers has been proposed. For solving combinatorial problems, examples of such proposals include analog electrical circuits^[238,239] and molecular computing^[240,241]. For machine learning, several hardware architectures specifically designed to implement neural networks have also been demonstrated^[242].

Motivated by the notion that coherence in quantum mechanics leads to the possibility of quantum computers, there has been increasing interest in using coherence, in particular

¹The contents of this chapter relate to the author's publication entitled "Gaussian Optical Ising Machines"

in optics, to find solutions to some of these difficult combinatorial problems. Optics is a promising candidate for implementing classical computation paradigms, due to the availability of a large number of modes and high bandwidths that allow for high computation speeds. Some tasks that optics has been used for include reservoir computing for speech recognition^[243–245] and classification tasks using support vector machines^[246]. Optics has also been proposed for hardware implementations of neural networks^[104,247].

8.1 Background

A combinatorial optimization problem of particular note that we focus on in the following is the Ising problem^[248]. The Ising problem, in the absence of an external magnetic field, consists of finding the configuration of a network of coupled spins that minimises the following Hamiltonian:

$$H = - \sum_{i,j} J_{ij} \sigma_i \sigma_j \quad (8.1)$$

where σ_i and σ_j are the values of the spins of sites i and j that can be either -1 or 1, and J_{ij} is the (i,j) entry of a matrix \mathbf{J} describing the spin-spin couplings. The Ising problem maps onto several physical and combinatorial problems, such as the maximum cut problem^[249]. It is known to be NP-hard, but special-purpose hardware may find solutions to the problem faster than conventional computers.

8.1.1 Optical Ising machines

It has recently been suggested that an optical setup, consisting of a train of coupled pulses undergoing parametric amplification in a cavity, can be used to find low-energy solutions of the Ising problem^[250,251]. This proposal relies on the fact that optical parametric oscillators (OPO) can adopt either a 0 or a π phase with respect to the pump light, so that these two phases can be used to encode up or down spin directions. Coupling between pulses can be arranged in such a way that the system preferentially oscillates in a configuration that minimises the Hamiltonian in equation 8.1.

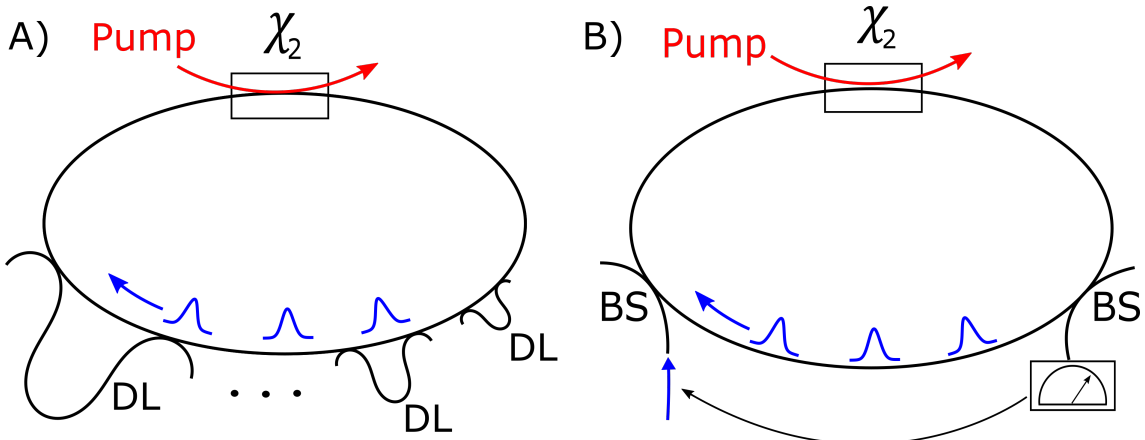


Figure 8.1: Overview of two types of optical Ising machines. A) In the optical delay line scheme, a part of each pulse is picked off into a delay line (DL) and interfered with a consecutive pulse. With a sufficient number of delay lines, every pulse can be made to couple to every other pulse. B) In measurement and injection feedback Ising machines, in every loop optical pulses undergo parametric amplification in a nonlinear (χ_2) material. A beam splitter (BS) picks off a fraction of each pulse for measurement by homodyne detection. The pulses are then displaced at a second BS by an amplitude dependent on the measurement result.

Figure 8.1 provides an overview of the two different schemes for implementing optical Ising machines that are considered in this work. In both cases, a train of pulses, initially in a vacuum state, circulates in a fiber loop with parametric gain. These pulses can be coupled with each other in two different ways to achieve the desired spin configuration.

Coupling between the pulses can be achieved in an optical delay line (ODL) architecture

(see Fig. 8.1a). In the general case for N pulses, N optical delay lines each split off a part of each pulse and interfere this fraction with a subsequent pulse at a beam splitter. Delay line i provides a delay of i times the repetition time between pulses and pulse n is thus coupled to pulse $n + i$. The length of each delay line is adjusted so that this coupling is performed with either a 0 or a π phase shift with respect to the original picked off pulse, depending on matrix \mathbf{J} . The number of delay lines that is required depends on the connectivity of matrix \mathbf{J} .

More recently, a new measurement and injection feedback (MIF) scheme, that implements the required coupling using partial homodyne measurements and electronic feedback, was demonstrated with up to two thousand coupled pulses^[220,221] (see Fig. 8.1b). In the MIF scheme, this coupling is produced by splitting off a fraction of each pulse, upon which homodyne measurement is performed. Each pulse is then displaced in phase space via optical feedback, with an amplitude and phase determined by the collective measurement results of all the other pulses as well as matrix \mathbf{J} .

In both cases, the gain or the feedback is increased with each round trip and the system settles into a final configuration of steady state OPO pulses with well-defined phases. The sign of the phases of the pulses can then be measured and mapped onto spin orientations in an Ising model, in which the spin-spin coupling is determined by the optical coupling. The system preferentially settles into a configuration that corresponds to a low energy in the Ising model. Intuitively, this is because optical states in which the phases are configured in a way that maximise the feedback term are subject to higher gain than other optical states.

8.1.2 State of the art

Both ODL and MIF Ising machines have been experimentally demonstrated. The ODL Ising machines demonstrated to date have low connectivity between the encoded spins^[252,253], due to the challenge inherent in building many phase stable delay lines. Increasing connectivity and scale is an active area of research^[254]. Large scale MIF devices have been demonstrated and have been shown to outperform several other combinatorial optimization algorithms; in particular, Inagaki *et al.*^[221] demonstrated that their device could find a low energy configuration of a coupled system of 2000 spins up to 50 times faster than a conventional commercial computer.

In light of their experimental demonstrations of OPO Ising machines, Inagaki *et al.*^[221] and McMahon *et al.*^[220] raised interesting questions concerning the nature and role of quantum features and thresholding behaviour in the operation of their devices. Given the complex dynamics of the OPO and pump fields below and above threshold, elucidating the relevant computational mechanisms presents challenges.

8.2 Gaussian optical Ising machines

In the following, we address these challenges by studying MIF and ODL Ising machines that operate with simplified dynamics described by the Gaussian state formalism^[34]. We show that these simplified dynamics are sufficient to attain high success probabilities similar to what has been experimentally demonstrated. Based on these results, we propose simplifications to experimental realisations of these devices, which we envisage will be of use to scaling them up to many more coupled pulses.

8.2.1 Theoretical framework

OPO Ising machines are usually described using the stochastic master equation formalism^[255,256], which describes the interaction between the pump and the signal both below and above threshold. Specifically, the stochastic master equation formalism for N pulses involves calculating the evolution of a coupled system, consisting of N signal fields denoted s , N pump fields denoted p , and an external reservoir, governed by the following Hamiltonian^[250]:

$$H = H_{\text{free}} + H_{\text{int}} + H_{\text{irr}} + H_{\text{coupling}} \quad (8.2)$$

where H_{coupling} represents the coupling Hamiltonian between the signal pulses, the exact expression of which depends on the coupling scheme, and the other Hamiltonians in this expression are given by:

$$H_{\text{free}} = \hbar\omega_s \sum_i \hat{a}_{si}^\dagger \hat{a}_{si} + \hbar\omega_p \sum_i \hat{a}_{pi}^\dagger \hat{a}_{pi} \quad (8.3)$$

$$H_{\text{int}} = i\hbar\kappa \sum_i (\hat{a}_{si}^{\dagger 2} \hat{a}_{pi} - \hat{a}_{si}^2 \hat{a}_{pi}^\dagger) \quad (8.4)$$

$$H_{\text{irr}} = i\hbar\sqrt{\gamma_s} \sum_i (\hat{a}_{si}^\dagger \hat{B}_{si} - \hat{a}_{si} \hat{B}_{si}^\dagger) \quad (8.5)$$

In these equations, H_{free} is the free Hamiltonian, H_{int} is the coupling Hamiltonian between the pump and the signal, and H_{irr} describes the irreversible interaction between the signal photons and the reservoir photons. ω_s and ω_p are respectively the frequencies

of the signal and of the pump, κ is the gain of the parametric amplification process, γ_s is the loss rate of the signal photons, and \hat{B} corresponds to the reservoir operators. In these equations, we have assumed that only the signal fields propagate in the cavity, whereas the pump fields only interact with the signal fields in the nonlinear medium and are discarded after the interaction. From these Hamiltonians, and by treating the reservoir operators as Gaussian noise, stochastic c-number Langevin equations can be derived that describe the joint evolution of the signal and pump fields^[255].

We use a different approach to describe the evolution of these Ising machines. We observe that, in Hamiltonian 8.2, several of the terms correspond to Gaussian processes. Both H_{free} and H_{irr} are at most quadratic in the creation and annihilation operators. As for the coupling term, both the beam splitters and delay lines used in the ODL architecture and the homodyne and displacement operations used in the MIF scheme also correspond to Gaussian processes. Furthermore, in the limit of weak pump depletion, the \hat{a}_{pi} terms in H_{int} can be treated as constant complex numbers, so that H_{int} is also quadratic in this limit and can be described as a simple Gaussian squeezing operation^[257].

Based on the observation that many of the relevant processes are Gaussian, in the following we consider optical Ising machines that are governed entirely by the simplified dynamics described by the Gaussian state formalism. We treat the pump fields classically and only consider the signal fields. As stated in the introduction, we describe a state consisting of N signal fields by its $2N \times 2N$ covariance matrix \mathbf{M} and its $2N$ -length displacement vector \mathbf{d} . Operations on this state are described by simple matrix operations on the covariance matrix and displacement vector. The exact formulae used for our simulations are described in Appendix A.

8.2.2 Gaussian measurement-feedback Ising machines

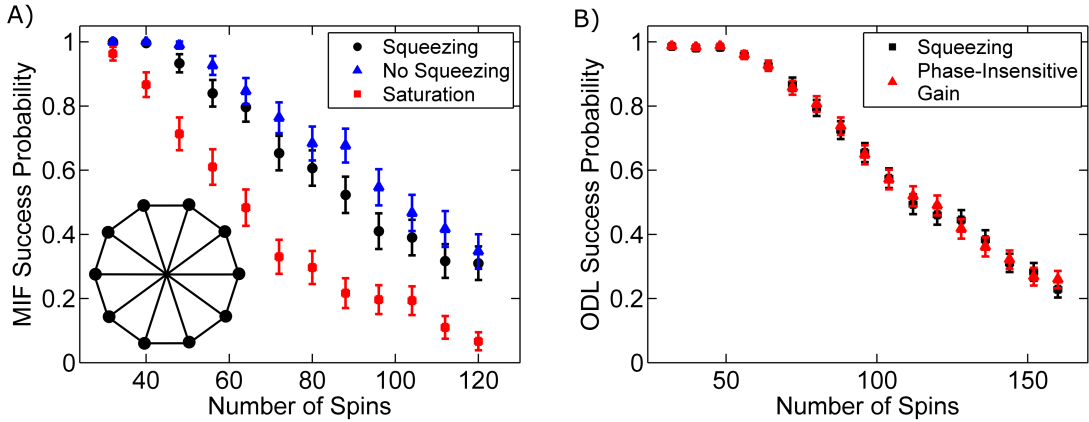


Figure 8.2: Estimated probabilities of finding the correct ground state energies for Möbius ladder graphs of different sizes. A) Simulation of MIF Ising machines including squeezing (circles), without squeezing (triangles), and with saturated feedback (squares). The inset depicts a Möbius ladder graph. B) Simulations of ODL Ising machines with squeezing (circles) and a phase-insensitive gain medium (triangles). All error bars indicate a 95% confidence interval.

We first simulate a Gaussian analogue of the MIF Ising machine demonstrated by McMahon *et al.*^[220]. To provide a comparison of our results to their work, we calculate the success probabilities for finding the ground state energies of specific Ising systems, where the spin-spin couplings are given by Möbius ladder graphs (see figure 8.2a). The (i, j) entry of the **J** matrix corresponding to these Möbius ladders is -1 if nodes i and j are connected in the graph representing the Möbius ladder, and 0 otherwise. McMahon *et al.* found that their experimental system could find the correct ground state energy with a probability going from nearly 100% for small systems to about 20% for a 100-spin system.

Our simulation proceeds as follows. The N pulses start in a vacuum state. In every loop, each pulse undergoes squeezing with a squeezing parameter of 0.2 , followed by 30% loss. We then pick off 10% of each pulse on a beam splitter, on which we perform a simulated homodyne measurement. This simulated measurement performed on each pulse yields a set of N real numbers corresponding to the measurement results. These numbers are written

as a vector \mathbf{c} . As described by McMahon *et al.* we then displace the modes as follows:

$$\mathbf{d} \rightarrow \mathbf{d} + n\eta\mathbf{J}\mathbf{c} \quad (8.6)$$

where n is the loop number and $\eta = 0.001$ is the feedback strength. With these parameters, the pump power is initially roughly 25% below the oscillation threshold of the system with $\eta = 0$, which is similar to what was used in the experiment by McMahon *et al.* We note that when $\eta > 0$, the feedback term in equation 8.6 is sufficient to bring the system above threshold since the feedback continually increases over time.

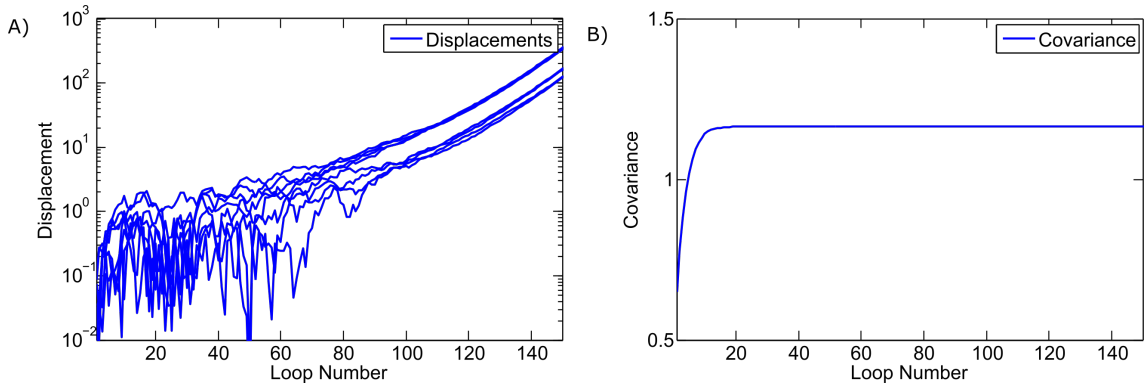


Figure 8.3: Evolution of the pulses in an 8 pulse MIF Ising machine. A) Evolution of the absolute value of the elements of the displacement vector during the course of a single simulation run, plotted for the first 150 loops. B) Evolution of the covariance terms corresponding to the measured quadratures.

Figure 8.3 shows a typical evolution of the pulses in a given run of our simulations. We see from the evolution of the displacement that all the pulses are close to vacuum for about the first 100 loops. After a while, the increase in the feedback term forces the displacements to diverge towards a configuration that minimises the Ising Hamiltonian. On the other hand, the covariance corresponding to the measured quadrature quickly reaches a

steady state, which is determined by the balance between the loss, the squeezing, and the quadrature measurement. We note that because there is no optical interference between the pulses and all the operations are done along the same axis in phase space, the covariance matrix does not have any off-diagonal elements.

After 300 loops through the system, we take the sign of the elements of \mathbf{d} to be the orientation of the corresponding spins, with which we calculate the energy of the spin configuration using equation 8.1. We repeat this process with graphs of up to 120 spins. The probabilities of finding the correct result for these different sizes, estimated from 300 trials for each size, are shown in figure 2a. We find a probability greater than 50% of finding the correct result for sizes up to about 90 spins.

Gain saturation

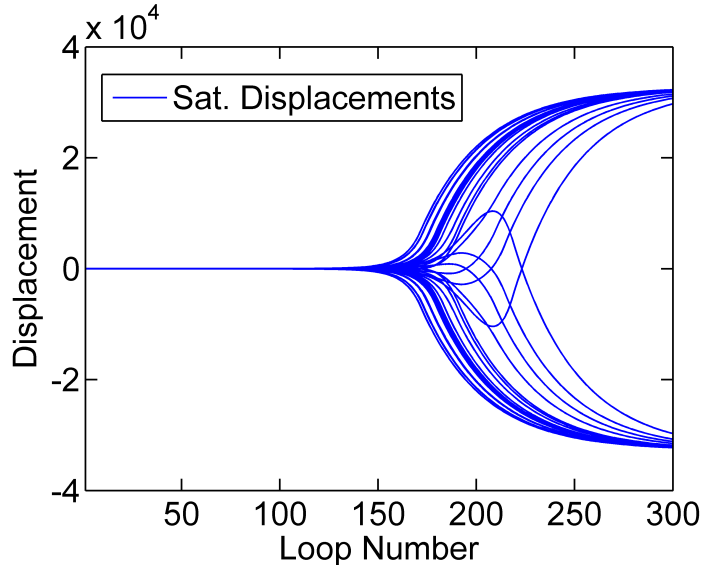


Figure 8.4: Evolution of the displacements of the pulses in a 40 pulse MIF Ising machine with saturated displacement.

The simulation above does not include gain saturation that would be present in a realistic machine, for example due to pump depletion, and that could affect the success probability.

To investigate the influence of saturation, we repeat our MIF simulations with the feedback displacement capped at 1000. The evolution of the displacements of the pulses is shown in Fig. 8.4. The dynamics are now different than they were without the displacement. Whereas earlier when the pulses had become macroscopic their displacement would not change sign, now some of the displacements do change sign quite late in the process. This behaviour is possible now whereas it was not possible in our previous simulations because the capped displacement imposes a limit to the strength of the pulse to pulse coupling, so that one or two pulses diverging can no longer drag all the other pulses along in a specific direction in phase space. Similar behaviour where pulses changed sign quite late in the evolution has been observed experimentally by McMahon *et al* on their system.

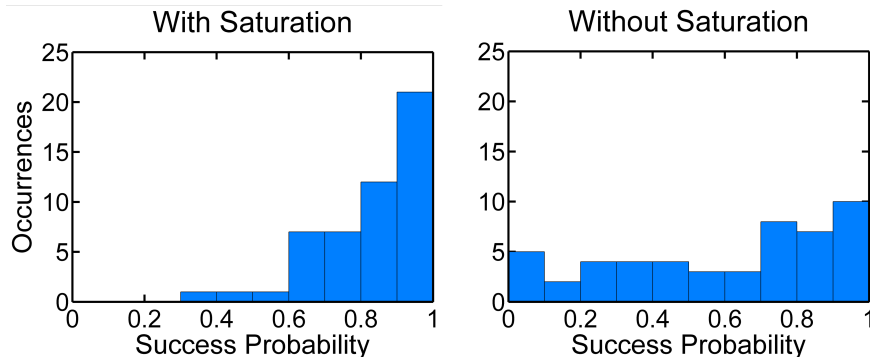


Figure 8.5: Histograms of the success probabilities for 50 randomly selected cubic graphs with 16 spins, for a MIF Ising machine with (left) and without (right) saturated feedback. The probabilities are estimated from 100 simulation trials per graph.

This difference in behaviour affects the performance of the Ising machine. In the case of a Möbius ladder graph the performance is adversely affected (Fig. 8.1). However, we find that the change in performance is different for different graphs. Following McMahon *et al.*^[220], we calculate the success probability for 50 randomly chosen 16-spin cubic graphs, for which each spin is connected to exactly three others, using 100 trials per graph. Figure 8.5 compares our results for a saturated and an unsaturated MIF Ising machine. With

saturation, low success probabilities are not observed. However, not every graph benefits. The success probability is only increased in 29 out of 50 cases. We observe similar outcomes for different values of the maximum feedback displacement, ranging from 100 to 10^6 .

8.2.3 Gaussian optical delay line Ising machines

We also study a Gaussian analogue to ODL Ising machines. In our simulation, the pulses circulate around the loop 100 times. In every round trip, each pulse undergoes squeezing with a squeezing parameter of 0.2. Then, for every pair of pulses (i, j) , if J_{ij} is -1 , 10% of pulse i is picked off on a beam splitter, given a π phase shift, and interfered with pulse j on a 90:10 beam splitter.

This evolution is described entirely by the covariance matrix of the optical pulses. As opposed to our simulation of the MIF Ising machine, the evolution of the optical state is deterministic and there is no stochastic element until the final measurement. Furthermore, the displacement vector is always **0**. Over the course of many round-trips, the elements of the covariance matrix become larger and larger, which reflects the large classical uncertainty on the state of the system. However, despite this uncertainty, the interference induced by the beam splitters and delay lines introduces correlations into the covariance matrix that depend on matrix J_{ij} .

After 100 round trips, we read out the state of the system by simulating a homodyne measurement on each pulse, thus yielding N measurement results drawn from the probability distribution determined by the covariance matrix of the state. Each of these measurement results maps onto a spin orientation in the Ising model, and then onto an energy based on equation 8.1. To simulate multiple trials as would be done in an experiment, we simulate

this homodyne measurement procedure on the optical state 1000 times. We use these 1000 trials to estimate the probability of success (Fig. 2b) for a given Möbius ladder graph. We find a success probability greater than 50% for sizes up to about 110 spins, which is similar to what we found for the MIF scheme.

Instead of simulating homodyne measurements on the system, another approach for finding a state that minimises the Hamiltonian in equation 8.1 would be to directly inspect the elements of the covariance matrix. Since the covariance matrix evolve deterministically and the correlations in the system are encoded in the signs of the elements of this matrix, we can simply read out these signs. We note that in the special case of Möbius ladder graphs, reading off the elements of the covariance matrix correctly yields a spin configuration that minimises the Ising Hamiltonian for graphs up to size 160. However, we find that the spin configuration found from reading out the elements of the covariance matrix in general does not correspond to a spin configuration that is as low as other configurations that could probabilistically be found by the simulated homodyne measurements. Furthermore, doing so would yield a single spin configuration, whereas the multiple homodyne measurements yield many possible candidates.

8.2.4 Interpretation

We analyse the workings of our simulations to provide an intuitive understanding of the underlying mechanisms and comparisons to similar classical algorithms. Our simulation of Gaussian MIF Ising machines can be understood as implementing a classical discrete random walk in optical phase space, in which the position of the walker is specified by the displacement vector. Each step taken by the walker is directed by the random outcome of

the homodyne measurements via the feedback operation. As the feedback strength increases over time, the walker tends to move towards a specific direction in phase space away from the origin. This direction corresponds to a spin configuration that minimises the Ising energy. This process is reminiscent of other Monte Carlo optimisation schemes such as simulated annealing^[258], in which a classical random walk probes parameter space.

In our simulation of Gaussian ODL Ising machines, we deterministically generate a probability distribution which is a multivariate Gaussian function. A specific spin configuration is found by drawing a sample from this distribution. This procedure is reminiscent of boson sampling with Gaussian states and Gaussian measurements^[62].

We note that both classes of optical Ising machines can be efficiently emulated by classical computation. This can be seen as a consequence of the fact that Gaussian optical Ising machines involve only Gaussian measurements on Gaussian states^[32].

8.3 Simplified Ising machines

The OPO Ising machines demonstrated by Inagaki *et al* and McMahon *et al* can potentially scale up to tens of thousands of coupled pulses^[251]. Based on our understanding of the computational mechanism of Gaussian optical Ising machines developed above, we propose simplified Ising machines that may provide a route to building large scale devices.

8.3.1 Replacing squeezing with other gain mechanisms

We first consider Gaussian MIF Ising machines. Based on our interpretation of their working mechanism and the invariance of the covariance matrix after just a few round-trips, we propose that the squeezing operation does not play an essential role beyond that of providing

gain in the system. To show this, we numerically simulate a Gaussian MIF Ising machine in which we simply remove the squeezing but maintain the measurement and feedback. The pulses in the system are therefore coherent states. In the absence of the gain from the squeezing that previously partially compensated for the loss, we double the feedback strength to $\eta = 0.002$. The random walk process implemented by these simulations follows the same pattern as in the simulation with parametric gain, but random numbers are now drawn from a narrower distribution around the average displacement due to the absence of squeezing. Even though the phase of a coherent state is not intrinsically bistable as for OPOs, the use of measurement and injection that displaces along only one quadrature axis effectively makes the phase bistable. Our simulation results are shown in figure 8.1. We find that removing the squeezing only has a small influence on the success probability.

Another alternative to an OPO-based MIF Ising machine involves the use of phase insensitive gain media instead of parametric gain, as has been previously proposed^[259]. Phase insensitive amplifiers add an equal amount of uncertainty to both quadratures; however the correlations between the quadratures of the pulses acquired during their evolution in an Ising machine are still present. Since the correlations between the phases of the pulses are still present, the relative orientations between the spins in the corresponding Ising model still map onto low energy solutions. Furthermore, such an experimental scheme would allow for tuning the uncertainty on the quadratures of the pulses, thus adding an additional controllable degree of freedom to the random walk implemented by MIF Ising machines.

We now consider Gaussian ODL Ising machines. Once again, we propose that the squeezing mechanism is not necessary beyond its role in providing gain. To demonstrate this, we simulate a Gaussian ODL Ising machine as discussed above, except the squeezing

operation is now replaced with phase insensitive gain. In this case, the phases of the pulses are no longer bistable, but they remain correlated due to their mutual couplings. Our results are shown in figure 8.1. The performance with phase insensitive gain is essentially identical to that with squeezing.

8.3.2 Outlook

These findings suggest that current optical Ising machines can be greatly simplified. Parametric gain involves a strong pump field that is phase locked to the pulses circulating in the cavity. The choice of operating wavelength and repetition rate is then largely determined by the availability of nonlinear materials and pump lasers. By removing the need for parametric gain media, the design of optical Ising machines can be greatly simplified. Furthermore, we envisage that our analysis of optical Ising machines can be applied to many other instances of optical Ising machines to inform their design. Given that existing optical Ising machines can already outperform conventional commercial computers in terms of computation time^[221], we expect that simplified and larger Ising machines may be useful tools for solving difficult combinatorial optimisation problems.

We note that although these devices can be understood in terms of classical computation, the optical states in our simulations have quantum features that could be used for other protocols. For example, due to the squeezing operation, all the optical states that we simulate in our MIF Ising machine have a non-regular P-function, which indicates non-classicality. Furthermore, pulses of squeezed light in delay lines could be used for one-way quantum computing^[260]. An open question is also whether the quantum features of optical Ising machines could be harnessed in future implementations to find low-energy solutions to

the Ising problem more efficiently than with classical methods. Similar questions have for example been explored in the recent development of adiabatic quantum computing^[261,262], which also aims to solve hard combinatorial problems using superconducting architectures.

8.4 Conclusion

In this chapter, we studied a class of optical devices that can be used to find low energy solutions to the Ising model. We introduced a theoretical framework using the Gaussian state formalism to analyse their working mechanism. We used the insight gained from this study to propose simplifications to these devices, which we anticipate will help them address larger scale problems.

Chapter **9**

Conclusion

The last few years have seen significant progress in the field of quantum optics. New experimental tools have been developed, and the number of applications of quantum optical systems has also increased to encompass several fields from metrology to quantum computation. This thesis has aimed to contribute to these developments. In the following, we summarise the work presented in this thesis, and then discuss potential directions of future research.

9.1 Summary

9.1.1 Components for linear optics

We first studied methods for developing and characterising essential components of linear optics: interferometers and detectors.

Reconfigurable interferometers

In chapter 4, we presented a new design for a universal multiport interferometer, capable of implementing any linear transformation between any number of optical modes. These universal interferometers have a wide range of applications. Since they can implement any interference pattern between any number of modes, they can be used in any linear optics scheme.

For interfering N optical modes, our design consists of a compact rectangular mesh of $N(N - 1)/2$ reconfigurable beam splitters and phase shifters. Given a targeted unitary transformation, we have demonstrated a constructive method for determining the settings of the optical elements such that the mesh implements the transformation. We have shown that our design improves upon previous designs by being maximally compact and less sensitive to loss. In addition, we have conducted a numerical analysis of the tolerance of our design to fabrication imperfections such as loss and imperfect splitting ratios, which we expect can inform future fabrication efforts.

In chapter 5, we experimentally demonstrated a modular design for reconfigurable integrated interferometers. This design consists of silica on silicon chips containing 10 reconfigurable Mach-Zehnder interferometers each. These chips can be connected to each other to form large interferometers. Experimentally, we found low coupling losses to optical fibre, low chip-to-chip coupling loss, and a wide tuning range of the phase shifters on the chips. However, we found a large amount of loss at the MZIs.

We implemented a wide range of optical transformations using a three chip assembly to demonstrate the flexibility of our approach. We first used the chip assembly as a switch, and successfully demonstrated switching from one input to any of six different outputs. Using a

self-configuring programming method, we then implemented a balanced 3×3 interferometer. Finally, we applied our algorithm for universal multiport interferometers to implement a set of 50 randomly chosen unitary transformations, with an average fidelity of 97.5%.

Photon detectors

In chapter 6, we started by measuring the efficiency of photon detectors using a method that does not require external calibration. We first constructed a radiometer to provide an absolute reference for optical power against which we can calibrate optical power meters. We then built a calibrated attenuator that we used to produce light at the few photon level with accurately known intensities. These few photon states of light were then used to accurately measure the detection efficiencies of several SPADs and SNSPDs.

We then described the operation of a type of superconducting photon detector of particular interest to quantum optics: the transition edge sensor. These high efficiency and photon-number resolving detectors require temperatures of about 100 mK, as well as SQUIDs and further stages of amplification. We explained how these temperatures are achieved, how to configure the TESs, and how photon numbers are extracted from the analog signal at the output. These TESs were then used for several experiments within our research group.

9.1.2 Applications of linear optics

We also studied two applications of linear optics in the fields of quantum simulation and classical computation.

Simulation of vibronic spectroscopy

In chapter 7, we explored the feasibility of a protocol for estimating molecular vibronic spectra in the presence of experimental imperfections. These spectra play an important role in quantum chemistry, and the quantum optics protocol for calculating them is of particular interest due to its experimental simplicity and the absence of efficient classical algorithms for doing so. However, due to the analog nature of the quantum simulation, experimental errors are bound to degrade the quality of the estimation.

We showed in theory that the impact of these imperfections can be accounted for. We proposed an efficiently calculable metric for evaluating the impact of experimental errors on an experiment. This metric can be used to optimise the experimental parameters to obtain an optical state that is as close as possible to the targeted state. Furthermore, we have shown that a non-classicality condition can be derived using this metric, and can be used as a criterion for outperforming a classical algorithm.

We then performed an experiment highlighting the impact of imperfections and demonstrating the applicability of our theory. Our experiment simulated part of the spectrum of tropolone. By carefully characterising our experimental setup, we were able to describe the optical state we produced, bound the error on our estimate of the spectrum, and analyse the main sources of imperfection in our experiment: optical loss and the use of a TMSV to approximate two SMSVs. We also extended our analysis to the simulation of other molecules such as benzene and sulphur dioxide.

Optical Ising machines

In chapter 8, we studied coherent Ising machines. These machines use coupled pulses of light, with gain provided by parametric amplification, to find the ground states of Ising systems. Since the Ising problem is an NP-hard problem, systems capable of finding solutions faster than standard computing hardware are highly desirable. The coherent Ising machines demonstrated to date have consisted of up to 2000 coupled pulses and have been shown to be as much as 50 times faster than standard electronic computing hardware.

We introduced a Gaussian approximation of these devices. We found that this Gaussian approximation found solutions to the Ising problem with probabilities similar to those found in experiment. We then explored methods by which coherent Ising machines could be simplified while maintaining equally high success probabilities. We found that parametric amplification is not necessary and can be replaced by phase-insensitive gain or feedback. Without the requirement for parametric amplification, we expect that increasing the number of coupled pulses in coherent Ising machines will be easier.

9.2 Directions for future research

In the following, we discuss ways in which the research presented in this thesis can be pursued to further the field of linear quantum optics.

9.2.1 Building larger quantum states

One of the main challenges in linear quantum optics remains that of building and measuring larger optical quantum states. We have discussed some methods by which this objective can be achieved using new designs for interferometers, as well as superconducting detectors.

Several options exist to make further progress.

Improving the modular chips discussed in chapter 5 requires achieving lower loss and better coupling to optical fibre. We envision that moving to the telecom range for our next generation of chips will yield significant improvement due to the larger mode size in this range. Contained within a larger mode size, light is less sensitive to fabrication imperfections such as surface roughness^[108]. Moreover, in the telecom range we will have access to state of the art optical components developed by the telecommunications industry. With lower loss, many modular chips can be used to build large interferometers that can be used to manipulate many more modes. These new telecom wavelength chips are currently being developed.

To enhance current photon number resolving capabilities, we must consider ways in which to operate a larger number of TESs. At present, operating four TESs simultaneously is a significant time investment. Automation techniques and more advanced electronics control systems are being developed in our group to operate a larger number of TESs. We have also moved to a more modern and user-friendly dilution refrigerator which has room to accomodate more TESs.

Integration of more components on chip is also a promising option. Both sources^[101] and TESs^[105] have been demonstrated using the same photonic chip technology that we use for the modular chips. Building TESs or SNSPDs directly onto photonic chips will allow for lower interface losses and provide a route to measuring a larger number of modes. The use of photon sources built on the same platform will also significantly reduce losses, although filtering out the pump light will be challenging.

With improvements in both modular chips and TES control technology, a wide range of

experiments becomes accessible. Quantum states consisting of several modes with several photons per mode can be manipulated and measured. For example, optical states created on-chip can be measured and prepared in novel ways using weak field homodyne measurements^[263]. These measurements require both the phase stability naturally provided by integrated photonics and the ability to resolve several photons per mode given by TESs. New regimes of boson sampling involving higher photon numbers and different input states can also be explored. Moreover, these chips and detectors will allow us to perform vibronic spectroscopy simulation experiments beyond the range demonstrated in this thesis.

9.2.2 Developing quantum applications

We envisage that the development of more easily scalable and lower loss technology, such as our future generations of modular chips and TESs, will make larger scale quantum simulations feasible. Experiments with only a few tens of modes may outperform the best modern classical computers with currently known computation methods. In the case of vibronic spectra simulations, as discussed earlier the scalability of the protocol spectra is still an open question, and further research is required.

In addition to providing a route to building larger optical Ising machine, our work suggests some questions for future research. It has been suggested that non-Gaussian behaviour may provide a computational advantage^[264]. Why and how this is an open question. Another question is whether and how the quantum features of the optical states in the system can be harnessed to provide a computational advantage. It is indeed believed that quantum tunneling can provide a computational speedup for a range of combinatorial optimisation problems^[261]. Finally, given the ability of these coherent Ising machines to produce large

quantum states, other natural questions are exactly what types of states can be produced using related schemes and what other applications these states may have. Our research group’s activity on the manipulation of time-encoded quantum states^[56] in fibre loops places us in a good position to pursue this work.

9.3 Outlook

Quantum optics is an exciting field to be doing research in, with both a rapid rate of progress and applications in many areas of science and technology. Linear quantum optics contributes not only to the development of larger and more interesting all-optical systems for various applications, but will also form the backbone of larger quantum networks including other quantum systems such as trapped ions. These networks support quantum communication^[86], enable precise quantum metrology schemes^[87], and are a strong contender for universal quantum computation^[84]. In parallel to linear optics, the development of single photon level nonlinearities^[265,266] may also provide a whole new range of capabilities.

The potential rewards from developing large quantum systems, in both quantum optics and other fields of quantum research, justify attempting to overcome the huge challenges involved. The last few years have seen a huge number of research initiative that seek to explore different avenues to building such systems^[267,268]. This research will provide further insight into quantum physics, and will also allow for further developments in quantum technologies. Although the exact extent to which this “quantum revolution”^[12] will impact our lives is still unclear, these advances are set to expand the scope of modern technology and have a high impact on many fields of science.

Appendix **A**

Gaussian state formalism formulae

The following provides the formulae used to implement our simulations in both the “Gaussian Optical Ising Machines” and the “Quantum Optical Simulation of Vibronic Spectroscopy” chapters using the Gaussian state formalism. In our simulations, we used the convention that the covariance matrix of vacuum is $\frac{1}{2}\mathbf{1}$, but the following formulae do not depend on the choice of convention.

A.1 Simulation of squeezing and loss

Single mode squeezing on mode i of a N -mode Gaussian state changes its covariance matrix \mathbf{M} and displacement vector \mathbf{d} as follows:

$$\mathbf{M} \rightarrow \mathbf{S}\mathbf{M}\mathbf{S}^T \quad (\text{A.1})$$

$$\mathbf{d} \rightarrow \mathbf{S}\mathbf{d} \quad (\text{A.2})$$

where \mathbf{S} is unity except for entries $2i - 1$ and $2i$ along the diagonal which are equal to e^{-r} and e^r respectively, where r is the (real) squeezing parameter.

Optical loss on mode i is modelled by a beam splitter with transmission t acting between mode i and an ancilla vacuum mode. Although the overall transformation for both modes taken as a whole is unitary, in order to consider the effects on the signal mode alone we trace over the ancilla vacuum mode after this transformation. This changes \mathbf{M} and \mathbf{d} as follows:

$$\mathbf{M} \rightarrow \mathbf{T}\mathbf{M}\mathbf{T}^T + \mathbf{R}\mathbf{V}\mathbf{R}^T \quad (\text{A.3})$$

$$\mathbf{d} \rightarrow \mathbf{T}\mathbf{d} \quad (\text{A.4})$$

where \mathbf{T} is unity except for entries $2i - 1$ and $2i$ along the diagonal which are equal to \sqrt{t} , \mathbf{R} is unity except for entries $2i - 1$ and $2i$ along the diagonal which are equal to $\sqrt{1-t}$, and \mathbf{V} is the covariance matrix for an N -mode vacuum.

A.2 Simulation of homodyne measurements

A homodyne measurement on the N -th optical mode of an N -mode Gaussian state described by covariance matrix \mathbf{M} and displacement vector \mathbf{d} is simulated as follows. \mathbf{M} can be written in block-diagonal form:

$$\begin{pmatrix} \mathbf{A} & \mathbf{B} \\ \mathbf{B}^T & \mathbf{C} \end{pmatrix} \quad (\text{A.5})$$

where \mathbf{C} is the reduced 2×2 covariance matrix for the homodyned mode, \mathbf{A} is the reduced covariance matrix for the remaining $N - 1$ modes, and \mathbf{B} keeps track of the correlations between these modes. To simulate the outcome of a homodyne measurement, we draw a number c_m from the marginal Gaussian probability distribution described by \mathbf{C} and \mathbf{d} projected onto the chosen measurement axis.

To describe the state after this measurement, we project mode N onto an infinitely squeezed state which is displaced along the measurement axis by an amount c_m . We call \mathbf{c} the displacement vector of mode mode N after this projection. The remaining $N - 1$ modes are then described by a new covariance matrix \mathbf{A}' and displacement vector \mathbf{d}' :

$$\mathbf{A}' = \mathbf{A} - \mathbf{B}(\mathbf{P}\mathbf{C}\mathbf{P})^+ \mathbf{B}^T \quad (\text{A.6})$$

$$\mathbf{d}' = \mathbf{d}_A + \mathbf{B}(\mathbf{P}\mathbf{C}\mathbf{P})^+ (\mathbf{c} - \mathbf{d}_C) \quad (\text{A.7})$$

where \mathbf{P} is a projector onto the measured quadrature of mode N , ${}^+$ denotes the Moore-Penrose pseudo-inverse, and \mathbf{d}_A and \mathbf{d}_C are the original reduced displacement vectors for the first $N - 1$ modes and for the N -th mode, respectively.

A.3 Simulation of phase insensitive gain

Phase-insensitive gain on a given mode i of an N -mode state can be modelled in the Gaussian state formalism by using an ancilla vacuum mode, implementing a two-mode squeezing operation with squeezing parameter r on these two modes, and tracing out the ancilla mode. In the $(x_1, p_1, \dots, x_N, p_N)$ basis in optical phase space, the covariance matrix \mathbf{M} and

the displacement vector \mathbf{d} for the amplified mode are thus transformed as follows:

$$\mathbf{M} \rightarrow \mathbf{C}\mathbf{M}\mathbf{C}^T + \mathbf{S}\mathbf{V}\mathbf{S}^T \quad (\text{A.8})$$

$$\mathbf{d} \rightarrow \mathbf{C}\mathbf{d} \quad (\text{A.9})$$

where \mathbf{C} is unity except for entries $2i - 1$ and $2i$ along the diagonal which are equal to $\cosh(r)$, \mathbf{S} is unity except for entries $2i - 1$ and $2i$ along the diagonal which are equal to $\sinh(r)$, and \mathbf{V} is the covariance matrix for an N -mode vacuum. In our simulation of an ODL Ising machine with phase-insensitive gain, we used a squeezing parameter of $r = 0.6$, which yields an amount of gain $\cosh(r) \approx 1.19$ that is similar to the gain $e^{r_1} \approx 1.22$ provided by single mode squeezing with $r_1 = 0.2$.

Appendix B

Success probabilities for simulated optical Ising machines

The following table contains the list of graphs that were used to produce the histograms shown in the “Gain Saturation” section of the chapter on Gaussian Optical Ising Machines, along with the estimated probabilities of finding the corresponding ground state in a single run for both a saturated and an unsaturated MIF Ising machine. The probabilities were estimated from 100 runs for each graph. The graphs are shown using the compact graph6 format, in which each graph is represented by a string of ASCII characters^[269]. They are listed in increasing order of their success probability for an unsaturated MIF Ising machine.

Graph	Without Saturation	With Saturation
O}GWOKA?O@?C?E?E??o?J	0	0.84
O{O____GA?G?_?i?d?K_Ao	0	0.95
O{O_o_H@?G?O?U?G?Ag?Y	0.01	1
O{SoOKA?O@?D?C?C?@W?M	0.02	0.54

O } KGGGA?gA?G?I?D?@O?J	0.02	0.99
OsX@?gOA?K?S?O?G_B?k	0.06	1
O { O_ogG@?C?H?K?G_B??J	0.07	0.99
OsX@?gOA?G?T?_?O_EO?q	0.18	0.38
OsX@?oO@GG?S?a?Q?AG?L	0.24	0.62
O { O_ooc@?D?G?H?D?AO?R	0.24	0.49
O { S__SC@?E?C?H?D?AG?T	0.27	0.98
O { O_o_G@?G?W?S?I_D??h	0.29	0.69
OsXP?_G@_C?K?Q?I?AG?L	0.32	0.76
O { O____IA?I?_?c?W?Ag? [0.34	0.86
O { O____IA_G?_?W?Q?Ag? [0.38	0.84
O } GOWOC?_A_G?J?G?AG?J	0.43	0.64
O { O____IA?G?_?s?R?D??h	0.45	0.69
O { O____IA_G?_?R?O?EG?Y	0.45	1
O { O_o_G@OG?Q?O?J?CO?T	0.48	0.98
O { S__OE@?C_G?O?H?AW? [0.53	1
O { O_o_G@OG?O?Y?H?B??J	0.58	1
O { S__OE@?C_G?P?H?AG?T	0.61	1
OsX@GoO@?C_K?G?C_@O?J	0.65	1
OsX@?oO@GG?Q?a?O_CG?X	0.68	0.63
OsX_o_C?_B?G?G?D_A_?T	0.70	0.69
OsXP?_G@?C_O?X?Q?CG?h	0.74	0.97
O { S_gOC?_A?G?M?I?A_?J	0.76	0.69
O { O_o_E@?A?C?D?D?@O?R	0.77	0.75
O { O_o_G@OG?O?Y?K?@_?J	0.77	1

O } KGGGA?_B?G?K?D?@G?L	0.79	0.75
O { O_o_H@_G?H?G?D?@O?F	0.81	1
O } GOWSC?O@?C?E?C?@g?M	0.82	0.74
OsX_o_D?_A?C?E?D?@_?F	0.82	1
OsX_o_D?_A?C?D?C?@g?U	0.86	0.86
O } GOWSC?O@_C?C?A??w?M	0.88	0.81
O } GOOOC@?D?Q?W?Q?A_?F	0.89	0.82
O { O_ogG@?C?H?I?G_A_?b	0.90	0.80
O { S__OC@?E?S?Q?H?AO?b	0.92	0.84
O { O_ogG@?D?G?L?C?@G?J	0.93	0.99
O { S__OC@?D_O?W?P?A_?F	0.94	0.85
OsX@?gOAGK?S?O?C_@G?L	0.95	0.87
O { S__OF@?C?G?C?C_@o?Y	0.95	0.99
O { S_gOC?gA?G?I?D?@O?J	0.96	0.86
O { S__OE@?C?H?P?I?AO?b	0.97	0.90
OsXP?cG@GC?G?H?E?@_?F	0.98	0.84
O { S__OC@GE?P?O?G_AO?J	0.99	0.94
O { S__SC@?D?G?G?D_A_?T	0.99	0.92
O } GOWOC?_A?H?G?G_B_?e	1	1
O { O_oE@?A?C?E?E??o?J	1	1
O { O___IA?K?_?T?O?DG?i	1	0.95

Bibliography

- [1] Schrödinger, E. Die gegenwärtige situation in der quantenmechanik. *Naturwissenschaften* **23**, 807–812 (1935).
- [2] Horodecki, R., Horodecki, P., Horodecki, M. & Horodecki, K. Quantum entanglement. *Reviews of modern physics* **81**, 865 (2009).
- [3] Hensen, B. *et al.* Loophole-free Bell inequality violation using electron spins separated by 1.3 kilometres. *Nature* **526**, 682–686 (2015).
- [4] Nielsen, M. A. & Chuang, I. L. *Quantum computation and quantum information* (Cambridge university press, 2010).
- [5] Zurek, W. H. Decoherence and the transition from quantum to classical, revisited. In *Quantum Decoherence*, 1–31 (Springer, 2006).
- [6] Georgescu, I., Ashhab, S. & Nori, F. Quantum simulation. *Reviews of Modern Physics* **86**, 153 (2014).
- [7] Aasi, J. *et al.* Enhanced sensitivity of the LIGO gravitational wave detector by using squeezed states of light. *Nature Photonics* **7**, 613–619 (2013).
- [8] Peters, A., Chung, K. Y. & Chu, S. High-precision gravity measurements using atom interferometry. *Metrologia* **38**, 25 (2001).
- [9] Wasilewski, W., Jensen, K., Krauter, H., Renema, J. J., Balabas, M. & Polzik, E. S. Quantum noise limited and entanglement-assisted magnetometry. *Physical Review Letters* **104**, 133601 (2010).
- [10] Balasubramanian, G. *et al.* Nanoscale imaging magnetometry with diamond spins under ambient conditions. *Nature* **455**, 648–651 (2008).
- [11] Bloom, B. *et al.* An optical lattice clock with accuracy and stability at the 10^{-18} level. *Nature* **506**, 71–75 (2014).
- [12] Dowling, J. P. & Milburn, G. J. Quantum technology: the second quantum revolution. *Philosophical Transactions of the Royal Society of London A: Mathematical, Physical and Engineering Sciences* **361**, 1655–1674 (2003).
- [13] Zhang, J. *et al.* Observation of a many-body dynamical phase transition with a 53-qubit quantum simulator. *Nature* **551**, 601 (2017).

- [14] Bernien, H. *et al.* Probing many-body dynamics on a 51-atom quantum simulator. *Nature* **551**, 579 (2017).
- [15] Kelly, J. *et al.* State preservation by repetitive error detection in a superconducting quantum circuit. *Nature* **519**, 66–69 (2015).
- [16] Veldhorst, M. *et al.* A two-qubit logic gate in silicon. *Nature* **526**, 410–414 (2015).
- [17] Leonhardt, U. *Measuring the quantum state of light*, vol. 22 (Cambridge university press, 1997).
- [18] Aspect, A., Dalibard, J. & Roger, G. Experimental test of Bell’s inequalities using time-varying analyzers. *Physical review letters* **49**, 1804 (1982).
- [19] Giustina, M. *et al.* Significant-loophole-free test of Bell’s theorem with entangled photons. *Physical review letters* **115**, 250401 (2015).
- [20] Shalm, L. K. *et al.* Strong loophole-free test of local realism. *Physical review letters* **115**, 250402 (2015).
- [21] Brune, M. *et al.* Observing the progressive decoherence of the meter in a quantum measurement. *Physical Review Letters* **77**, 4887 (1996).
- [22] Pryde, G. J., Chrzanowski, H. M., Shalm, L. K., Weston, M. M., Nam, S. W., Slussarenko, S. & Verma, V. B. Unconditional violation of the shot-noise limit in photonic quantum metrology. *Nature Photonics* **11**, 700 (2017).
- [23] Barz, S., Kashefi, E., Broadbent, A., Fitzsimons, J. F., Zeilinger, A. & Walther, P. Demonstration of blind quantum computing. *Science* **335**, 303–308 (2012).
- [24] Gobby, C., Yuan, Z. & Shields, A. Quantum key distribution over 122 km of standard telecom fiber. *Applied Physics Letters* **84**, 3762–3764 (2004).
- [25] Wang, X.-L. *et al.* Experimental ten-photon entanglement. *Physical review letters* **117**, 210502 (2016).
- [26] Marsili, F. *et al.* Detecting single infrared photons with 93% system efficiency. *Nature Photonics* **7**, 210–214 (2013).
- [27] Grynberg, G., Aspect, A., Fabre, C. *et al.* *Introduction to quantum optics* (Cambridge University Press, 2010).
- [28] Braunstein, S. L. Squeezing as an irreducible resource. *Physical Review A* **71**, 55801 (2005).
- [29] Banaszek, K. & Wódkiewicz, K. Operational theory of homodyne detection. *Physical Review A* **55**, 3117 (1997).
- [30] Wigner, E. On the quantum correction for thermodynamic equilibrium. *Physical review* **40**, 749 (1932).
- [31] Rahimi-Keshari, S., Ralph, T. C. & Caves, C. M. Sufficient conditions for efficient classical simulation of quantum optics. *Physical Review X* **6**, 021039 (2016).
- [32] Bartlett, S. D., Sanders, B. C., Braunstein, S. L. & Nemoto, K. Efficient classical simulation of continuous variable quantum information processes. In *Quantum Information with Continuous Variables*, 47–55 (Springer, 2002).

- [33] Dodonov, V., Manko, O. & Manko, V. Multidimensional Hermite polynomials and photon distribution for polymode mixed light. *Physical Review A* **50**, 813 (1994).
- [34] Adesso, G., Ragy, S. & Lee, A. R. Continuous variable quantum information: Gaussian states and beyond. *Open Systems & Information Dynamics* **21**, 1440001 (2014).
- [35] Ringbauer, M., Duffus, B., Branciard, C., Cavalcanti, E. G., White, A. G. & Fedrizzi, A. Measurements on the reality of the wavefunction. *Nature Physics* **11**, 249–254 (2015).
- [36] Bouwmeester, D., Pan, J.-W., Mattle, K., Eibl, M., Weinfurter, H. & Zeilinger, A. Experimental quantum teleportation. *Nature* **390**, 575–579 (1997).
- [37] Metcalf, B. J. *et al.* Quantum teleportation on a photonic chip. *Nature Photonics* **8**, 770–774 (2014).
- [38] Hong, C. K., Ou, Z.-Y. & Mandel, L. Measurement of subpicosecond time intervals between two photons by interference. *Physical review letters* **59**, 2044 (1987).
- [39] Menssen, A. J., Jones, A. E., Metcalf, B. J., Tichy, M. C., Barz, S., Kolthammer, W. S. & Walmsley, I. A. Distinguishability and many-particle interference. *Physical Review Letters* **118**, 153603 (2017).
- [40] Agne, S. *et al.* Observation of genuine three-photon interference. *Physical Review Letters* **118**, 153602 (2017).
- [41] Slussarenko, S., Weston, M. M., Chrzanowski, H. M., Shalm, L. K., Verma, V. B., Nam, S. W. & Pryde, G. J. Unconditional violation of the shot-noise limit in photonic quantum metrology. *Nature Photonics* **11**, 700 (2017).
- [42] Grangier, P., Slusher, R., Yurke, B. & LaPorta, A. Squeezed-light-enhanced polarization interferometer. *Physical review letters* **59**, 2153 (1987).
- [43] Wolfgramm, F., Vitelli, C., Beduini, F. A., Godbout, N. & Mitchell, M. W. Entanglement-enhanced probing of a delicate material system. *Nature Photonics* **7**, 28–32 (2013).
- [44] Taylor, M. A., Janousek, J., Daria, V., Knittel, J., Hage, B., Bachor, H.-A. & Bowen, W. P. Biological measurement beyond the quantum limit. *Nature Photonics* **7**, 229–233 (2013).
- [45] Taylor, M. A. & Bowen, W. P. Quantum metrology and its application in biology. *Physics Reports* **615**, 1–59 (2016).
- [46] Abbott, B. P. *et al.* Observation of gravitational waves from a binary black hole merger. *Physical review letters* **116**, 061102 (2016).
- [47] Shor, P. W. Polynomial-time algorithms for prime factorization and discrete logarithms on a quantum computer. *SIAM review* **41**, 303–332 (1999).
- [48] Debnath, S., Linke, N., Figgatt, C., Landsman, K., Wright, K. & Monroe, C. Demonstration of a small programmable quantum computer with atomic qubits. *Nature* **536**, 63–66 (2016).
- [49] The IBM Quantum Experience, <http://www.research.ibm.com/quantum>. Site accessed on 11/01/2018.
- [50] Knill, E., Laflamme, R. & Milburn, G. J. A scheme for efficient quantum computation with linear optics. *Nature* **409**, 46–52 (2001).

- [51] Nielsen, M. A. Optical quantum computation using cluster states. *Physical review letters* **93**, 040503 (2004).
- [52] Menicucci, N. C., van Loock, P., Gu, M., Weedbrook, C., Ralph, T. C. & Nielsen, M. A. Universal quantum computation with continuous-variable cluster states. *Physical review letters* **97**, 110501 (2006).
- [53] Gimeno-Segovia, M., Shadbolt, P., Browne, D. E. & Rudolph, T. From three-photon Greenberger-Horne-Zeilinger states to ballistic universal quantum computation. *Physical review letters* **115**, 020502 (2015).
- [54] Menicucci, N. C. Fault-tolerant measurement-based quantum computing with continuous-variable cluster states. *Physical review letters* **112**, 120504 (2014).
- [55] Rudolph, T. Why I am optimistic about the silicon-photonics route to quantum computing. *APL Photonics* **2**, 030901 (2017).
- [56] Boutari, J., Feizpour, A., Barz, S., Di Franco, C., Kim, M., Kolthammer, W. & Walmsley, I. A. Large scale quantum walks by means of optical fiber cavities. *Journal of Optics* **18**, 094007 (2016).
- [57] Broome, M. A., Fedrizzi, A., Lanyon, B. P., Kassal, I., Aspuru-Guzik, A. & White, A. G. Discrete single-photon quantum walks with tunable decoherence. *Physical review letters* **104**, 153602 (2010).
- [58] Peruzzo, A. *et al.* Quantum walks of correlated photons. *Science* **329**, 1500–1503 (2010).
- [59] Harris, N. C. *et al.* Quantum transport simulations in a programmable nanophotonic processor. *Nature Photonics* **11**, 447–452 (2017).
- [60] Ma, X.-S., Dakic, B., Naylor, W., Zeilinger, A. & Walther, P. Quantum simulation of the wavefunction to probe frustrated Heisenberg spin systems. *Nature Physics* **7**, 399–405 (2011).
- [61] Caruso, F., Spagnolo, N., Vitelli, C., Sciarrino, F. & Plenio, M. B. Simulation of noise-assisted transport via optical cavity networks. *Physical Review A* **83**, 013811 (2011).
- [62] Aaronson, S. & Arkhipov, A. The computational complexity of linear optics. In *Proceedings of the forty-third annual ACM symposium on Theory of computing*, 333–342 (ACM, 2011).
- [63] Scott Aaronson's blog, <http://www.scottaaronson.com/blog/?p=1579>. Site accessed on 12/02/2018.
- [64] Lund, A., Laing, A., Rahimi-Keshari, S., Rudolph, T., O'Brien, J. & Ralph, T. Boson sampling from a Gaussian state. *Physical Review Letters* **113**, 100502 (2014).
- [65] Hamilton, C. S., Kruse, R., Sansoni, L., Barkhofen, S., Silberhorn, C. & Jex, I. Gaussian boson sampling. *arXiv preprint arXiv:1612.01199* (2016).
- [66] Barkhofen, S., Bartley, T. J., Sansoni, L., Kruse, R., Hamilton, C. S., Jex, I. & Silberhorn, C. Driven boson sampling. *Physical Review Letters* **118**, 020502 (2017).
- [67] Gao, X. & Duan, L. Efficient classical simulation of noisy quantum computation. *arXiv preprint arXiv:1810.03176* (2018).
- [68] Renema, J. J., Menssen, A., Clements, W. R., Triginer, G., Kolthammer, W. S. & Walmsley, I. A. Efficient algorithm for boson sampling with partially distinguishable photons. *arXiv preprint arXiv:1707.02793* (2017).

- [69] García-Patrón, R., Renema, J. J. & Shchesnovich, V. Simulating boson sampling in lossy architectures. *arXiv preprint arXiv:1712.10037* (2017).
- [70] Spagnolo, N. *et al.* Experimental validation of photonic boson sampling. *Nature Photonics* **8**, 615–620 (2014).
- [71] Carolan, J. *et al.* On the experimental verification of quantum complexity in linear optics. *Nature Photonics* **8**, 621–626 (2014).
- [72] Walschaers, M., Kuipers, J., Urbina, J.-D., Mayer, K., Tichy, M. C., Richter, K. & Buchleitner, A. Statistical benchmark for bosonsampling. *New Journal of Physics* **18**, 032001 (2016).
- [73] Neville, A., Sparrow, C., Clifford, R., Johnston, E., Birchall, P. M., Montanaro, A. & Laing, A. Classical boson sampling algorithms with superior performance to near-term experiments. *Nature Physics* **13**, 1153 (2017).
- [74] Spring, J. B. *et al.* Boson sampling on a photonic chip. *Science* **339**, 798–801 (2013).
- [75] Broome, M. A., Fedrizzi, A., Rahimi-Keshari, S., Dove, J., Aaronson, S., Ralph, T. C. & White, A. G. Photonic boson sampling in a tunable circuit. *Science* **339**, 794–798 (2013).
- [76] Tillmann, M., Dakić, B., Heilmann, R., Nolte, S., Szameit, A. & Walther, P. Experimental boson sampling. *Nature Photonics* **7**, 540–544 (2013).
- [77] Crespi, A. *et al.* Integrated multimode interferometers with arbitrary designs for photonic boson sampling. *Nature Photonics* **7**, 545–549 (2013).
- [78] He, Y. *et al.* Time-bin-encoded boson sampling with a single-photon device. *Physical Review Letters* **118**, 190501 (2017).
- [79] Loredo, J. *et al.* Boson sampling with single-photon Fock states from a bright solid-state source. *Physical Review Letters* **118**, 130503 (2017).
- [80] Wang, H. *et al.* High-efficiency multiphoton boson sampling. *Nature Photonics* **11**, 361–365 (2017).
- [81] Bentivegna, M. *et al.* Experimental scattershot boson sampling. *Science Advances* **1**, e1400255 (2015).
- [82] Walmsley, I. A. & Nunn, J. Building quantum networks. *Physical Review Applied* **6**, 040001 (2016).
- [83] Kimble, H. J. The quantum internet. *Nature* **453**, 1023–1030 (2008).
- [84] Monroe, C., Raussendorf, R., Ruthven, A., Brown, K., Maunz, P., Duan, L.-M. & Kim, J. Large-scale modular quantum-computer architecture with atomic memory and photonic interconnects. *Physical Review A* **89**, 022317 (2014).
- [85] Reim, K. *et al.* Towards high-speed optical quantum memories. *Nature Photonics* **4**, 218 (2010).
- [86] Lo, H.-K., Curty, M. & Tamaki, K. Secure quantum key distribution. *Nature Photonics* **8**, 595–604 (2014).
- [87] Komar, P., Kessler, E. M., Bishof, M., Jiang, L., Sørensen, A. S., Ye, J. & Lukin, M. D. A quantum network of clocks. *Nature Physics* **10**, 582 (2014).

- [88] Takahashi, H., Neergaard-Nielsen, J. S., Takeuchi, M., Takeoka, M., Hayasaka, K., Furusawa, A. & Sasaki, M. Entanglement distillation from Gaussian input states. *Nature photonics* **4**, 178 (2010).
- [89] Yoshikawa, J.-I., Yokoyama, S., Kaji, T., Sornphiphatphong, C., Shiozawa, Y., Makino, K. & Furusawa, A. Invited article: Generation of one-million-mode continuous-variable cluster state by unlimited time-domain multiplexing. *APL Photonics* **1**, 060801 (2016).
- [90] Ren, J.-G. *et al.* Ground-to-satellite quantum teleportation. *Nature* **549**, 70 (2017).
- [91] Holleczek, A. *et al.* Quantum logic with cavity photons from single atoms. *Physical review letters* **117**, 023602 (2016).
- [92] Gazzano, O. *et al.* Bright solid-state sources of indistinguishable single photons. *Nature Communications* **4**, 1425 (2013).
- [93] Ding, X. *et al.* On-demand single photons with high extraction efficiency and near-unity indistinguishability from a resonantly driven quantum dot in a micropillar. *Physical review letters* **116**, 020401 (2016).
- [94] Mosley, P. J., Lundeen, J. S., Smith, B. J., Wasylczyk, P., URen, A. B., Silberhorn, C. & Walmsley, I. A. Heralded generation of ultrafast single photons in pure quantum states. *Physical Review Letters* **100**, 133601 (2008).
- [95] Christ, A. & Silberhorn, C. Limits on the deterministic creation of pure single-photon states using parametric down-conversion. *Physical Review A* **85**, 023829 (2012).
- [96] Kaneda, F., Xu, F., Chapman, J. & Kwiat, P. G. Quantum-memory-assisted multi-photon generation for efficient quantum information processing. *Optica* **4**, 1034–1037 (2017).
- [97] Vahlbruch, H. *et al.* Observation of squeezed light with 10-db quantum-noise reduction. *Physical review letters* **100**, 033602 (2008).
- [98] Mehmet, M., Ast, S., Eberle, T., Steinlechner, S., Vahlbruch, H. & Schnabel, R. Squeezed light at 1550 nm with a quantum noise reduction of 12.3 dB. *Optics express* **19**, 25763–25772 (2011).
- [99] Eto, Y., Koshio, A., Ohshiro, A., Sakurai, J., Horie, K., Hirano, T. & Sasaki, M. Efficient homodyne measurement of picosecond squeezed pulses with pulse shaping technique. *Optics letters* **36**, 4653–4655 (2011).
- [100] Harder, G., Bartley, T. J., Lita, A. E., Nam, S. W., Gerrits, T. & Silberhorn, C. Single-mode parametric-down-conversion states with 50 photons as a source for mesoscopic quantum optics. *Physical review letters* **116**, 143601 (2016).
- [101] Spring, J. B. *et al.* Chip-based array of near-identical, pure, heralded single-photon sources. *Optica* **4**, 90–96 (2017).
- [102] Silverstone, J. W. *et al.* On-chip quantum interference between silicon photon-pair sources. *Nature Photonics* **8**, 104–108 (2014).
- [103] Carolan, J. *et al.* Universal linear optics. *Science* **349**, 711–716 (2015).
- [104] Shen, Y. *et al.* Deep learning with coherent nanophotonic circuits. *Nature Photonics* **11**, 441 (2017).

- [105] Gerrits, T. *et al.* On-chip, photon-number-resolving, telecommunication-band detectors for scalable photonic information processing. *Physical Review A* **84**, 060301 (2011).
- [106] Kaiser, F., Fedrici, B., Zavatta, A., DAuria, V. & Tanzilli, S. A fully guided-wave squeezing experiment for fiber quantum networks. *Optica* **3**, 362–365 (2016).
- [107] Silverstone, J. W., Bonneau, D., O'Brien, J. L. & Thompson, M. G. Silicon quantum photonics. *IEEE Journal of Selected Topics in Quantum Electronics* **22**, 390–402 (2016).
- [108] Payne, F. & Lacey, J. A theoretical analysis of scattering loss from planar optical waveguides. *Optical and Quantum Electronics* **26**, 977–986 (1994).
- [109] Cardenas, J., Poitras, C. B., Robinson, J. T., Preston, K., Chen, L. & Lipson, M. Low loss etchless silicon photonic waveguides. *Optics express* **17**, 4752–4757 (2009).
- [110] Reed, G. T. & Knights, A. P. *Silicon photonics: an introduction* (John Wiley & Sons, 2004).
- [111] Takesue, H., Matsuda, N., Kuramochi, E., Munro, W. J. & Notomi, M. An on-chip coupled resonator optical waveguide single-photon buffer. *Nature communications* **4**, 2725 (2013).
- [112] Alloatti, L. *et al.* 42.7 Gbit/s electro-optic modulator in silicon technology. *Optics express* **19**, 11841–11851 (2011).
- [113] Harris, N. C. *et al.* Integrated source of spectrally filtered correlated photons for large-scale quantum photonic systems. *Physical Review X* **4**, 041047 (2014).
- [114] Pernice, W. H., Schuck, C., Minaeva, O., Li, M., Goltsman, G., Sergienko, A. & Tang, H. High-speed and high-efficiency travelling wave single-photon detectors embedded in nanophotonic circuits. *Nature communications* **3**, 1325 (2012).
- [115] Notaros, J. *et al.* Ultra-efficient CMOS fiber-to-chip grating couplers. In *Optical Fiber Communications Conference and Exhibition (OFC), 2016*, 1–3 (IEEE, 2016).
- [116] Cardenas, J., Poitras, C. B., Luke, K., Luo, L.-W., Morton, P. A. & Lipson, M. High coupling efficiency etched facet tapers in silicon waveguides. *IEEE Photonics Technology Letters* **26**, 2380–2382 (2014).
- [117] Jacobsen, R. S. *et al.* Strained silicon as a new electro-optic material. *Nature* **441**, 199–202 (2006).
- [118] Reed, G. T., Mashanovich, G., Gardes, F. & Thomson, D. Silicon optical modulators. *Nature photonics* **4**, 518–526 (2010).
- [119] Alibart, O. *et al.* Quantum photonics at telecom wavelengths based on lithium niobate waveguides. *Journal of Optics* **18**, 104001 (2016).
- [120] Weis, R. & Gaylord, T. Lithium niobate: summary of physical properties and crystal structure. *Applied Physics A: Materials Science & Processing* **37**, 191–203 (1985).
- [121] Sugii, K., Fukuma, M. & Iwasaki, H. A study on titanium diffusion into LiNbO₃ waveguides by electron probe analysis and X-ray diffraction methods. *Journal of Materials Science* **13**, 523–533 (1978).
- [122] Jin, H. *et al.* On-chip generation and manipulation of entangled photons based on reconfigurable lithium-niobate waveguide circuits. *Physical Review Letters* **113**, 103601 (2014).

- [123] Alferness, R., Ramaswamy, V., Korotky, S., Divino, M. & Buhl, L. Efficient single-mode fiber to titanium diffused lithium niobate waveguide coupling for $\lambda = 1.32 \mu\text{m}$. *IEEE Journal of Quantum Electronics* **18**, 1807–1813 (1982).
- [124] Krapick, S., Herrmann, H., Quiring, V., Brecht, B., Suche, H. & Silberhorn, C. An efficient integrated two-color source for heralded single photons. *New Journal of Physics* **15**, 033010 (2013).
- [125] Yoshizawa, A., Kaji, R. & Tsuchida, H. Generation of polarisation-entangled photon pairs at 1550 nm using two PPLN waveguides. *Electronics Letters* **39**, 621–622 (2003).
- [126] Yoshino, K.-I., Aoki, T. & Furusawa, A. Generation of continuous-wave broadband entangled beams using periodically poled lithium niobate waveguides. *Applied physics letters* **90**, 041111 (2007).
- [127] Krapick, S., Brecht, B., Quiring, V., Ricken, R., Herrmann, H. & Silberhorn, C. On-chip generation of photon-triplet states in integrated waveguide structures. In *CLEO: QELS_Fundamental Science*, FM2E-3 (Optical Society of America, 2015).
- [128] Tanner, M., Alvarez, L. S. E., Jiang, W., Warburton, R., Barber, Z. & Hadfield, R. A superconducting nanowire single photon detector on lithium niobate. *Nanotechnology* **23**, 505201 (2012).
- [129] Höpker, J. P. *et al.* Towards integrated superconducting detectors on lithium niobate waveguides. In *Quantum Photonic Devices*, vol. 10358, 1035809 (International Society for Optics and Photonics, 2017).
- [130] Staudt, M. U. *et al.* Fidelity of an optical memory based on stimulated photon echoes. *Physical review letters* **98**, 113601 (2007).
- [131] Minford, W., Korotky, S. & Alferness, R. Low-loss Ti:LiNbO₃ waveguide bends at X=1-3 μm . *IEEE Journal of Quantum Electronics* 1802–1806 (1983).
- [132] Wang, C., Zhang, M., Stern, B., Lipson, M. & Lončar, M. Nanophotonic lithium niobate electro-optic modulators. *Optics Express* **26**, 1547–1555 (2018).
- [133] Meany, T., Gross, S., Jovanovic, N., Arriola, A., Steel, M. & Withford, M. J. Towards low-loss lightwave circuits for non-classical optics at 800 and 1,550 nm. *Applied Physics A* **114**, 113–118 (2014).
- [134] Zauner, D., Kulstad, K., Rathje, J. & Svalgaard, M. Directly UV-written silica-on-silicon planar waveguides with low insertion loss. *Electronics Letters* **34**, 1582–1584 (1998).
- [135] Marshall, G. D., Politi, A., Matthews, J. C., Dekker, P., Ams, M., Withford, M. J. & O'Brien, J. L. Laser written waveguide photonic quantum circuits. *Optics express* **17**, 12546–12554 (2009).
- [136] Politi, A., Cryan, M. J., Rarity, J. G., Yu, S. & O'Brien, J. L. Silica-on-silicon waveguide quantum circuits. *Science* **320**, 646–649 (2008).
- [137] Smith, B. J., Kundys, D., Thomas-Peter, N., Smith, P. G. R. & Walmsley, I. A. Phase-controlled integrated photonic quantum circuits. *Optics Express* **17**, 13516–13525 (2009).
- [138] Natarajan, C. M., Tanner, M. G. & Hadfield, R. H. Superconducting nanowire single-photon detectors: physics and applications. *Superconductor Science and Technology* **25**, 063001 (2012).

- [139] Engel, A., Renema, J., Ilin, K. & Semenov, A. Detection mechanism of superconducting nanowire single-photon detectors. *Superconductor Science and Technology* **28**, 114003 (2015).
- [140] Dauler, E. A. *et al.* Photon-number-resolution with sub-30-ps timing using multi-element superconducting nanowire single photon detectors. *Journal of Modern Optics* **56**, 364–373 (2009).
- [141] Gemmell, N. R. *et al.* A miniaturized 4 K platform for superconducting infrared photon counting detectors. *Superconductor Science and Technology* (2017).
- [142] Irwin, K. An application of electrothermal feedback for high resolution cryogenic particle detection. *Applied Physics Letters* **66**, 1998–2000 (1995).
- [143] Fukuda, D. *et al.* Titanium-based transition-edge photon number resolving detector with 98% detection efficiency with index-matched small-gap fiber coupling. *Optics Express* **19**, 870–875 (2011).
- [144] Levine, Z. H., Glebov, B. L., Migdall, A. L., Gerrits, T., Calkins, B., Lita, A. E. & Nam, S. W. Photon-number uncertainty in a superconducting transition edge sensor beyond resolved-photon-number determination. *Journal of the Optical Society of America B* **31**, B20–B24 (2014).
- [145] Lanyon, B. P. *et al.* Towards quantum chemistry on a quantum computer. *Nature chemistry* **2**, 106–111 (2010).
- [146] Barz, S., Kassal, I., Ringbauer, M., Lipp, Y. O., Dakić, B., Aspuru-Guzik, A. & Walther, P. A two-qubit photonic quantum processor and its application to solving systems of linear equations. *Scientific reports* **4** (2014).
- [147] Barz, S., Fitzsimons, J. F., Kashefi, E. & Walther, P. Experimental verification of quantum computation. *Nature Physics* **9** (2013).
- [148] Reck, M., Zeilinger, A., Bernstein, H. J. & Bertani, P. Experimental realization of any discrete unitary operator. *Physical Review Letters* **73**, 58 (1994).
- [149] Tanizawa, K. *et al.* Ultra-compact 32×32 strictly-non-blocking Si-wire optical switch with fan-out LGA interposer. *Optics express* **23**, 17599–17606 (2015).
- [150] Miller, D. A. Self-configuring universal linear optical component. *Photonics Research* **1**, 1–15 (2013).
- [151] Miller, D. A. Perfect optics with imperfect components. *Optica* **2**, 747–750 (2015).
- [152] Birth of the programmable optical chip. *Nature Photonics* **10**, 1–1 (2016).
- [153] Capmany, J., Gasulla, I. & Perez, D. Microwave photonics: The programmable processor. *Nature Photonics* **10**, 6–8 (2016).
- [154] Chen, L.-N., Hall, E., Theogarajan, L. & Bowers, J. Photonic switching for data center applications. *IEEE Photonics journal* **3**, 834–844 (2011).
- [155] Stabile, R., Albores-Mejia, A., Rohit, A. & Williams, K. A. Integrated optical switch matrices for packet data networks. *Microsystems & Nanoengineering* **2** (2016).
- [156] Thomson, R. R., Kar, A. K. & Allington-Smith, J. Ultrafast laser inscription: an enabling technology for astrophotonics. *Optics express* **17**, 1963–1969 (2009).

- [157] Ribeiro, A., Ruocco, A., Vanacker, L. & Bogaerts, W. Demonstration of a 4×4 -port universal linear circuit. *Optica* **3**, 1348–1357 (2016).
- [158] Perez, D. *et al.* Multipurpose silicon photonics signal processor core. *Nature Communications* (2017).
- [159] Motes, K. R., Gilchrist, A., Dowling, J. P. & Rohde, P. P. Scalable boson sampling with time-bin encoding using a loop-based architecture. *Physical review letters* **113**, 120501 (2014).
- [160] Alber, G. *et al.* *Quantum Information: An introduction to basic theoretical concepts and experiments*, vol. 173 (Springer, 2003).
- [161] Miller, D. A. Self-aligning universal beam coupler. *Optics express* **21**, 6360–6370 (2013).
- [162] Crespi, A. *et al.* Suppression law of quantum states in a 3D photonic fast fourier transform chip. *Nature communications* **7** (2016).
- [163] Shen, C., Zhang, Z. & Duan, L.-M. Scalable implementation of boson sampling with trapped ions. *Physical review letters* **112**, 050504 (2014).
- [164] Peropadre, B., Aspuru-Guzik, A. & García-Ripoll, J. J. Equivalence between spin Hamiltonians and boson sampling. *Physical Review A* **95**, 032327 (2017).
- [165] Peropadre, B., Guerreschi, G. G., Huh, J. & Aspuru-Guzik, A. Proposal for microwave boson sampling. *Physical review letters* **117**, 140505 (2016).
- [166] Jing, L. *et al.* Tunable efficient unitary neural networks (EUNN) and their application to RNNs. *arXiv preprint arXiv:1612.05231* (2016).
- [167] Miller, D. A. Setting up meshes of interferometers—reversed local light interference method. *Optics Express* **25**, 29233–29248 (2017).
- [168] Morichetti, F. *et al.* 4-channel all-optical MIMO demultiplexing on a silicon chip. In *Optical Fiber Communication Conference*, ThE3.7 (2016).
- [169] Mower, J., Harris, N. C., Steinbrecher, G. R., Lahini, Y. & Englund, D. High-fidelity quantum state evolution in imperfect photonic integrated circuits. *Physical Review A* **92**, 032322 (2015).
- [170] Metcalf, B. J. *et al.* Multiphoton quantum interference in a multiport integrated photonic device. *Nature communications* **4**, 1356 (2013).
- [171] Bonneau, D. *et al.* Quantum interference and manipulation of entanglement in silicon wire waveguide quantum circuits. *New Journal of Physics* **14**, 045003 (2012).
- [172] Peruzzo, A., Laing, A., Politi, A., Rudolph, T. & O’Brien, J. L. Multimode quantum interference of photons in multiport integrated devices. *Nature communications* **2**, 224 (2011).
- [173] These random unitary matrices were generated using the QR decomposition of random matrices, following the code developed by Toby Cubitt, available on www.dr-qubit.org/matlab.php.
- [174] Burgwal, R., Clements, W. R., Smith, D. H., Gates, J. C., Kolthammer, W. S., Renema, J. J. & Walmsley, I. A. Using an imperfect photonic network to implement random unitaries. *Optics Express* **25**, 28236–28245 (2017).
- [175] Russell, N. J., Chakhmakhchyan, L., O’Brien, J. L. & Laing, A. Direct dialling of Haar random unitary matrices. *New Journal of Physics* **19**, 033007 (2017).

- [176] Fletcher, R. *Practical methods of optimization* (John Wiley & Sons, 2013).
- [177] Thomas-Peter, N. *et al.* Integrated photonic sensing. *New Journal of Physics* **13**, 055024 (2011).
- [178] Thomas-Peter, N. *Quantum enhanced precision measurement and information processing with integrated photonics*. Ph.D. thesis, Balliol College, University of Oxford (2012).
- [179] Adikan, F. R., Gawith, C. B., Smith, P. G., Sparrow, I. J., Emmerson, G. D., Riziotis, C. & Ahmad, H. Design and demonstration of direct UV-written small angle X couplers in silicon-on-silicon for broadband operation. *Applied optics* **45**, 6113–6118 (2006).
- [180] Neyer, A., Mevenkamp, W., Thylen, L. & Lagerstrom, B. A beam propagation method analysis of active and passive waveguide crossings. *Journal of Lightwave Technology* **3**, 635–642 (1985).
- [181] Rogers, H. L., Ambran, S., Holmes, C., Smith, P. G. & Gates, J. C. In situ loss measurement of direct UV-written waveguides using integrated Bragg gratings. *Optics Letters* **35**, 2849–2851 (2010).
- [182] Uppu, R., Wolterink, T. A. W., Tentrup, T. B. H. & Pinkse, P. W. H. Quantum optics of lossy asymmetric beam splitters. *Opt. Express* **24**, 16440–16449 (2016).
- [183] Humphreys, P. C. *Experimental and theoretical techniques for quantum-enhanced metrology and optical quantum information processing*. Ph.D. thesis, University of Oxford (2015).
- [184] Varnava, M., Browne, D. E. & Rudolph, T. How good must single photon sources and detectors be for efficient linear optical quantum computation? *Physical Review Letters* **100**, 060502 (2008).
- [185] Humphreys, P. C. *et al.* Tomography of photon-number resolving continuous-output detectors. *New Journal of Physics* **17**, 103044 (2015).
- [186] Parr, A. C. The candela and photometric and radiometric measurements. *Journal of research of the National Institute of Standards and Technology* **106**, 151 (2001).
- [187] Klyshko, D. Use of two-photon light for absolute calibration of photoelectric detectors. *Quantum Electronics* **10**, 1112–1117 (1980).
- [188] Lunghi, T., Korzh, B., Sanguinetti, B. & Zbinden, H. Absolute calibration of fiber-coupled single-photon detector. *Optics Express* **22**, 18078–18092 (2014).
- [189] Sanguinetti, B., Guerreiro, T., Monteiro, F., Gisin, N. & Zbinden, H. Measuring absolute spectral radiance using an erbium-doped fiber amplifier. *Physical Review A* **86**, 062110 (2012).
- [190] Martin, J., Fox, N. & Key, P. A cryogenic radiometer for absolute radiometric measurements. *Metrologia* **21**, 147 (1985).
- [191] Mandel, L. & Wolf, E. The measures of bandwidth and coherence time in optics. *Proceedings of the Physical Society* **80**, 894 (1962).
- [192] Mandel, L. Fluctuations of photon beams: the distribution of the photo-electrons. *Proceedings of the Physical Society* **74**, 233 (1959).
- [193] Lita, A. E., Miller, A. J. & Nam, S. W. Counting near-infrared single-photons with 95% efficiency. *Optics express* **16**, 3032–3040 (2008).

- [194] Metcalf, B. J. *Silica-on-silicon waveguide circuits and superconducting detectors for integrated quantum information processing*. Ph.D. thesis, University of Oxford (2014).
- [195] Irwin, K. D. *Phonon-mediated particle detection using superconducting tungsten transition-edge sensors*. Ph.D. thesis, Stanford University (1995).
- [196] Fohrmann, L. S., Petrov, A. Y., Lang, S., Jalas, D., Krauss, T. F. & Eich, M. Single mode thermal emission. *Optics express* **23**, 27672–27682 (2015).
- [197] Smirnov, K., Vachtomin, Y., Divochiy, A., Antipov, A. & Goltsman, G. Dependence of dark count rates in superconducting single photon detectors on the filtering effect of standard single mode optical fibers. *Applied Physics Express* **8**, 022501 (2015).
- [198] Welty, R. P. & Martinis, J. M. A series array of dc SQUIDs. *IEEE Transactions on Magnetics* **27**, 2924–2926 (1991).
- [199] Sperling, J. *et al.* Detector-independent verification of quantum light. *Phys. Rev. Lett.* **118**, 163602 (2017).
- [200] Sperling, J. *et al.* Identification of nonclassical properties of light with multiplexing layouts. *Phys. Rev. A* **96**, 013804 (2017).
- [201] Stobińska, M. *et al.* Quantum interference enables constant-time quantum information processing. *arXiv preprint arXiv:1807.03960* (2018).
- [202] Barz, S., Dakić, B., Lipp, Y. O., Verstraete, F., Whitfield, J. D. & Walther, P. Linear-optical generation of eigenstates of the two-site XY model. *Physical Review X* **5**, 021010 (2015).
- [203] Hachmann, J. *et al.* The Harvard clean energy project: large-scale computational screening and design of organic photovoltaics on the world community grid. *The Journal of Physical Chemistry Letters* **2**, 2241–2251 (2011).
- [204] Butler, H. J. *et al.* Using Raman spectroscopy to characterize biological materials. *Nature protocols* **11**, 664–687 (2016).
- [205] Gross, M., Müller, D. C., Nothofer, H.-G., Scherf, U., Neher, D., Bräuchle, C. & Meerholz, K. Improving the performance of doped π -conjugated polymers for use in organic light-emitting diodes. *Nature* **405**, 661–665 (2000).
- [206] Bak, K. L., Gauss, J., Jørgensen, P., Olsen, J., Helgaker, T. & Stanton, J. F. The accurate determination of molecular equilibrium structures. *The Journal of Chemical Physics* **114**, 6548–6556 (2001).
- [207] Deaven, D. M. & Ho, K.-M. Molecular geometry optimization with a genetic algorithm. *Physical review letters* **75**, 288 (1995).
- [208] Gillespie, R. J. & Hargittai, I. *The VSEPR model of molecular geometry* (Courier Corporation, 2013).
- [209] Born, M. & Oppenheimer, R. Zur quantentheorie der moleküle. *Annalen der Physik* **389**, 457–484 (1927).
- [210] Duschinsky, F. The importance of the electron spectrum in multi atomic molecules. Concerning the Franck-Condon principle. *Acta Physicochim. URSS* **7**, 551–566 (1937).

- [211] Doktorov, E. V., Malkin, I. A. & Man'ko, V. I. Dynamical symmetry of vibronic transitions in polyatomic molecules and the Franck-Condon principle. *Journal of Molecular Spectroscopy* **64**, 302–326 (1977).
- [212] Huh, J., Guerreschi, G. G., Peropadre, B., McClean, J. R. & Aspuru-Guzik, A. Boson sampling for molecular vibronic spectra. *Nature Photonics* **9**, 615–620 (2015).
- [213] Condon, E. U. Nuclear motions associated with electron transitions in diatomic molecules. *Physical Review* **32**, 858 (1928).
- [214] Franck, J. & Dymond, E. G. Elementary processes of photochemical reactions. *Transactions of the Faraday Society* **21**, 536–542 (1926).
- [215] Huh, J. & Yung, M.-H. Vibronic boson sampling: Generalized Gaussian boson sampling for molecular vibronic spectra at finite temperature. *Scientific Reports* **7** (2017).
- [216] Hu, L. *et al.* Simulating molecular spectroscopy with circuit quantum electrodynamics. *arXiv preprint arXiv:1703.03300* (2017).
- [217] Shen, Y., Huh, J., Lu, Y., Zhang, J., Zhang, K., Zhang, S. & Kim, K. Quantum simulation of molecular spectroscopy in trapped-ion device. *arXiv preprint arXiv:1702.04859* (2017).
- [218] Sparrow, C. *et al.* Simulating the vibrational quantum dynamics of molecules using photonics. *Nature* **557**, 660 (2018).
- [219] Wu, L.-A., Kimble, H., Hall, J. & Wu, H. Generation of squeezed states by parametric down conversion. *Physical Review Letters* **57**, 2520 (1986).
- [220] McMahon, P. L. *et al.* A fully-programmable 100-spin coherent Ising machine with all-to-all connections. *Science* (2016).
- [221] Inagaki, T. *et al.* A coherent Ising machine for 2000-node optimization problems. *Science* **354**, 603–606 (2016).
- [222] Paraoanu, G.-S. & Scutaru, H. Fidelity for multimode thermal squeezed states. *Physical Review A* **61**, 022306 (2000).
- [223] Marian, P. & Marian, T. A. Uhlmann fidelity between two-mode Gaussian states. *Physical Review A* **86**, 022340 (2012).
- [224] Banchi, L., Braunstein, S. L. & Pirandola, S. Quantum fidelity for arbitrary Gaussian states. *Physical Review Letters* **115**, 260501 (2015).
- [225] Jankowiak, H.-C., Stuber, J. L. & Berger, R. Vibronic transitions in large molecular systems: rigorous prescreening conditions for Franck-Condon factors. *J. Chem. Phys.* **127**, 234101 (2007).
- [226] Marian, P., Marian, T. A. & Scutaru, H. Quantifying nonclassicality of one-mode Gaussian states of the radiation field. *Physical Review Letters* **88**, 153601 (2002).
- [227] Rahimi-Keshari, S., Lund, A. P. & Ralph, T. C. What can quantum optics say about computational complexity theory? *Physical Review Letters* **114**, 060501 (2015) (2015).
- [228] Giddings, J. C. *Advances in chromatography*, vol. 14 (CRC Press, 1976).
- [229] Smith, W. The strong Duschinsky effect and the intensity of transitions in non-totally symmetric vibrations in the electronic spectra of polyatomic molecules. *Journal of molecular spectroscopy* **187**, 6–12 (1998).

- [230] Weedbrook, C., Pirandola, S., García-Patrón, R., Cerf, N. J., Ralph, T. C., Shapiro, J. H. & Lloyd, S. Gaussian quantum information. *Reviews of Modern Physics* **84**, 621 (2012).
- [231] Eckstein, A., Christ, A., Mosley, P. J. & Silberhorn, C. Highly efficient single-pass source of pulsed single-mode twin beams of light. *Physical Review Letters* **106**, 013603 (2011).
- [232] Worsley, A. *et al.* Absolute efficiency estimation of photon-number-resolving detectors using twin beams. *Optics express* **17**, 4397–4412 (2009).
- [233] Helt, L., Steel, M. & Sipe, J. Parasitic nonlinearities in photon pair generation via integrated spontaneous four-wave mixing: critical problem or distraction? *Applied Physics Letters* **102**, 201106 (2013).
- [234] Berger, R., Fischer, C. & Klessinger, M. Calculation of the vibronic fine structure in electronic spectra at higher temperatures. 1. benzene and pyrazine. *J. Phys. Chem. A* **102**, 7157–7167 (1998).
- [235] Lee, C.-L., Yang, S.-H., Kuo, S.-Y. & Chang, J.-L. A general formula of two-dimensional Franck–Condon integral and the photoelectron spectroscopy of sulfur dioxide. *Journal of Molecular Spectroscopy* **256**, 279–286 (2009).
- [236] Simon, R. Peres-Horodecki separability criterion for continuous variable systems. *Physical Review Letters* **84**, 2726 (2000).
- [237] Sperling, J. Characterizing maximally singular phase-space distributions. *Physical Review A* **94**, 013814 (2016).
- [238] Tank, D. & Hopfield, J. Simple ‘neural’ optimization networks: An A/D converter, signal decision circuit, and a linear programming circuit. *IEEE Transactions on Circuits and Systems* **33**, 533–541 (1986).
- [239] Yoshimura, C., Yamaoka, M., Hayashi, M., Okuyama, T., Aoki, H., Kawarabayashi, K.-i. & Mizuno, H. Uncertain behaviours of integrated circuits improve computational performance. *Scientific reports* **5** (2015).
- [240] Adleman, L. M. Molecular computation of solutions to combinatorial problems. *Nature* **369**, 40 (1994).
- [241] Lipton, R. J. DNA solution of hard computational problems. *Science* **268**, 542 (1995).
- [242] Rojas, R. *Neural networks: a systematic introduction* (Springer Science & Business Media, 2013).
- [243] Larger, L. *et al.* Photonic information processing beyond Turing: an optoelectronic implementation of reservoir computing. *Optics express* **20**, 3241–3249 (2012).
- [244] Larger, L., Baylón-Fuentes, A., Martinenghi, R., Udaltssov, V. S., Chembo, Y. K. & Jacquot, M. High-speed photonic reservoir computing using a time-delay-based architecture: million words per second classification. *Physical Review X* **7**, 011015 (2017).
- [245] Duport, F., Smerieri, A., Akroud, A., Haelterman, M. & Massar, S. Fully analogue photonic reservoir computer. *Scientific reports* **6**, 22381 (2016).
- [246] Saade, A., Caltagirone, F., Carron, I., Daudet, L., Drémeau, A., Gigan, S. & Krzakala, F. Random projections through multiple optical scattering: Approximating kernels at the speed of light. In *2016 IEEE International Conference on Acoustics, Speech and Signal Processing (ICASSP)*, 6215–6219 (IEEE, 2016).

- [247] Shainline, J. M., Buckley, S. M., Mirin, R. P. & Nam, S. W. Superconducting optoelectronic circuits for neuromorphic computing. *Physical Review Applied* **7**, 034013 (2017).
- [248] Barahona, F. On the computational complexity of Ising spin glass models. *Journal of Physics A: Mathematical and General* **15**, 3241 (1982).
- [249] Karp, R. M. Reducibility among combinatorial problems. In *Complexity of computer computations*, 85–103 (Springer, 1972).
- [250] Wang, Z., Marandi, A., Wen, K., Byer, R. L. & Yamamoto, Y. Coherent Ising machine based on degenerate optical parametric oscillators. *Physical Review A* **88**, 063853 (2013).
- [251] Haribara, Y., Utsunomiya, S. & Yamamoto, Y. A coherent Ising machine for MAX-CUT problems: performance evaluation against semidefinite programming and simulated annealing. In *Principles and Methods of Quantum Information Technologies*, 251–262 (Springer, 2016).
- [252] Marandi, A., Wang, Z., Takata, K., Byer, R. L. & Yamamoto, Y. Network of time-multiplexed optical parametric oscillators as a coherent Ising machine. *Nature Photonics* **8**, 937–942 (2014).
- [253] Inagaki, T., Inaba, K., Hamerly, R., Inoue, K., Yamamoto, Y. & Takesue, H. Large-scale Ising spin network based on degenerate optical parametric oscillators. *Nature Photonics* (2016).
- [254] Courtland, R. HPE’s new chip marks a milestone in optical computing. *IEEE Spectrum* (January 2017).
- [255] Drummond, P., McNeil, K. & Walls, D. Non-equilibrium transitions in sub/second harmonic generation. *Journal of Modern Optics* **28**, 211–225 (1981).
- [256] Maruo, D., Utsunomiya, S. & Yamamoto, Y. Truncated Wigner theory of coherent Ising machines based on degenerate optical parametric oscillator network. *Physica Scripta* **91**, 083010 (2016).
- [257] Milburn, G. & Walls, D. Production of squeezed states in a degenerate parametric amplifier. *Optics Communications* **39**, 401–404 (1981).
- [258] Kirkpatrick, S., Gelatt, C. D., Vecchi, M. P. *et al.* Optimization by simulated annealing. *Science* **220**, 671–680 (1983).
- [259] Utsunomiya, S., Takata, K. & Yamamoto, Y. Mapping of Ising models onto injection-locked laser systems. *Optics express* **19**, 18091–18108 (2011).
- [260] Alexander, R. N., Wang, P., Sridhar, N., Chen, M., Pfister, O. & Menicucci, N. C. One-way quantum computing with arbitrarily large time-frequency continuous-variable cluster states from a single optical parametric oscillator. *Physical Review A* **94**, 032327 (2016).
- [261] Kadowaki, T. & Nishimori, H. Quantum annealing in the transverse Ising model. *Physical Review E* **58**, 5355 (1998).
- [262] Farhi, E., Goldstone, J., Gutmann, S., Lapan, J., Lundgren, A. & Preda, D. A quantum adiabatic evolution algorithm applied to random instances of an NP-complete problem. *Science* **292**, 472–475 (2001).
- [263] Puentes, G., Lundein, J. S., Branderhorst, M. P., Coldenstrodt-Ronge, H. B., Smith, B. J. & Walmsley, I. A. Bridging particle and wave sensitivity in a configurable detector of positive operator-valued measures. *Physical review letters* **102**, 080404 (2009).

- [264] Shoji, T., Aihara, K. & Yamamoto, Y. Quantum model for coherent Ising machines: Stochastic differential equations with replicator dynamics. *Physical Review A* **96**, 053833 (2017).
- [265] De Santis, L. *et al.* A solid-state single-photon filter. *Nature Nanotechnology* (2017).
- [266] Volz, J., Scheucher, M., Junge, C. & Rauschenbeutel, A. Nonlinear π phase shift for single fibre-guided photons interacting with a single resonator-enhanced atom. *Nature Photonics* **8**, 965–970 (2014).
- [267] See <https://nqit.ox.ac.uk/> and <https://qutech.nl/> for some example of large research initiatives on quantum technologies. Sites accessed on 16/01/2018.
- [268] Gibney, E. *et al.* Billion-euro boost for quantum tech. *Nature* **523**, 426 (2016).
- [269] The definition of the graph6 format can be found here: <http://users.cecs.anu.edu.au/~bdm/data/formats.html>. A helpful online conversion tool between graph formats can be found here: <http://treedecompositions.com/#/translate>. Both of these sites were accessed on 30/08/2017.